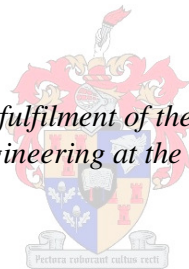


# **CFD investigation of flow in and around a natural draft cooling tower**

by  
Heinrich Claude Störm

*Thesis presented in partial fulfilment of the requirements for the degree  
Master of Science in Engineering at the University of Stellenbosch*



Supervisor: Mr. Hanno Reuter  
Mechanical and Mechatronic Engineering department

March 2010

## **Declaration**

By submitting this thesis electronically, I declare that the entirety of the work contained therein is my own, original work, that I am the owner of the copyright thereof (unless to the extent explicitly otherwise stated) and that I have not previously in its entirety or in part submitted it for obtaining any qualification.

Date: 18/10/2010

Copyright © 2010 Stellenbosch University  
All rights reserved

## **Abstract**

Cooling tower inlet losses and effective flow diameter under no crosswind conditions and the pressure distribution around a circular cylinder subjected to a crosswind are modelled using CFD. The CFD model used to evaluate the inlet losses is validated with data measured in an experimental cooling tower sector model and data obtained from literature. The effect of different inlet geometries on the inlet loss coefficient and the effective diameter are investigated in order to improve cooling tower inlet designs. CFD models are developed to investigate the pressure distribution around infinite and finite circular cylinders. The infinite cylinder is modelled with a smooth surface and a rough surface so that the results can be compared to experimental data from literature. Ultimately a finite cylinder model with a rough surface is developed and the results are compared to experimental data from literature.

## Opsomming

Koeltoring inlaatverlies en effektiewe vloei deursnit onder geen teenwind toestand en die drukverdeling rondom 'n sirkelvormige silinder, onderworpe aan 'n teenwind, word gemodelleer deur gebruik te maak van "CFD". Die "CFD" model wat gebruik word om die inlaatverlies te evalueer is gevalideer met data verkry vanaf 'n eksperimentele koeltoring sektor model. Verder word die "CFD" model gebruik in 'n ondersoek om te bepaal wat die effek is van verskillende inlaat geometrieë op die inlaat verlies koëffisiënt en die effektiewe diameter sodat die inlaat geometrie van koeltorings verbeter kan word. 'n "CFD" model word dan ontwikkel om die drukverdeling rondom 'n sirkelvormige silinder te ondersoek. Die silinder word as oneindig gesimuleer met 'n glade en ruwe wand sodat die resultate vergelyk kan word met eksperimentele data verkry vanaf literatuur. Die afdeling word afgesluit deur die silinder as eindig met 'n ruwe wand te simuleer en dan word die resultate vergelyk met eksperimentele data verkry vanaf literatuur.

# Table of contents

	<b>Page</b>
Declaration.....	i
Abstract.....	ii
Opsomming.....	iii
Table of contents.....	iv
List of Figures.....	vi
List of Tables.....	viii
Nomenclature.....	x
1 Introduction.....	1
1.1 Background.....	1
1.2 Motivation.....	2
1.3 Objectives.....	3
1.4 Scope of work.....	3
1.5 Thesis layout.....	4
2 Modelling of cooling tower inlets.....	5
2.1 Theory.....	7
2.2 Experimental Work.....	10
2.2.1 Determining packing material characteristics.....	10
2.2.2 Cooling tower sector model.....	14
2.3 CFD modelling procedure.....	17
2.4 Tower modelling results.....	23
2.4.1 Comparison of experimental and Fluent results for a sharp inlet.....	24
2.4.2 Comparison of CFD to correlations from literature.....	25
2.4.3 Comparison between experimental and Fluent results for different inlet geometries.....	29
2.4.4 Fluent analysis for different cooling tower inlet geometries.....	31
2.5 Discussion.....	35
3 Modelling of flow around a cylinder.....	37
3.1 Theory.....	38
3.2 Modelling procedure.....	41
3.2.1 Definition of nomenclature used in this chapter.....	41
3.2.2 Influence of variables in Fluent.....	43
3.3 Results.....	51
3.3.1 Comparison of 2-D analysis with literature.....	51
3.3.2 3-D analysis.....	52
3.4 Discussion.....	55
4 Conclusion.....	57
4.1 Inlet loss and effective diameter study.....	57
4.2 Flow around a circular cylinder.....	58

5	References .....	59
	Appendix A: Thermo Physical Properties of Fluids .....	62
	Appendix B: Experimental work .....	65
	B.1 Wind tunnel.....	65
	B.1.1 Description .....	65
	B.1.2 Measurement of mass flow rate .....	65
	B.2 Static pressure probe.....	67
	Appendix C: Packing Experiment.....	69
	C.1 Sample calculation for the packing .....	69
	C.2 Experimental data of the fill experiment .....	70
	Appendix D: Sector model test data.....	73
	D.1 Sample Calculation for CTSM.....	73
	D.2 CTSM Experimental Data .....	75
	Appendix E: Cooling tower inlet loss modelling using CFD .....	78
	E.1 Inlet loss coefficient sample calculation .....	78
	E.2 Data from Fluent for sharp inlet .....	81
	E.3 Data from Fluent for added structures .....	84

## List of Figures

	<b>Page</b>
Figure 1-1 Schematic of counter flow NDWCT	1
Figure 1-2 Plume flow patterns observed at the outlet of a cooling tower at different wind speeds (1)	2
Figure 2-1 Schematic of a NDCT showing the velocity profile and vena contracta inside the tower	5
Figure 2-2 Schematic of the test section for measuring the packing loss coefficient	11
Figure 2-3 Experimentally determined wire mesh loss coefficient data	12
Figure 2-4 Comparison of experimental wire mesh loss coefficient data to literature	13
Figure 2-5 Experimental cooling tower scale sector model	15
Figure 2-6 Static pressure probe used in CTSSM	16
Figure 2-7 $K_{he}$ determined in the CTSM	17
Figure 2-8 Comparison of the second order scheme to the combination of the PRESTO! and QUICK schemes with $d_i/c = 1045$ and $K_{p(ref)} = 21.91$	18
Figure 2-9 Effect of grid size on the pressure relation coefficient and velocity profile above the packing for $K_{p(ref)} = 29.91$	18
Figure 2-10 The different grid structures investigated for the analysis of tower inlet losses	19
Figure 2-11 Effect of grid type on the pressure relation coefficient and velocity profile for $K_p = 23.71$	20
Figure 2-12 Effect of different turbulence models on the pressure relation coefficient and velocity profile for $K_{p(ref)} = 21.91$	21
Figure 2-13 Effect of turbulence intensity and length scale on the pressure relation coefficient and velocity profile with $K_{p(ref)} = 22.21$	22
Figure 2-14 Effect of turbulence intensity on the total pressure	22
Figure 2-15 Static pressure drop deviation between Fluent and experimental data	24
Figure 2-16 Fluent curve comparison of $\delta(K_p)$ and $v/v_i$ for cylindrical and conical tower walls	26
Figure 2-17 Contour plots for cylindrical and inclined tower walls	27
Figure 2-18 Inlet loss coefficients determined with Fluent for a sharp inlet	28
Figure 2-19 Effective diameter ratio determined with Fluent for a sharp inlet	29
Figure 2-20 Different inlet geometries to improve the inlet loss coefficient and effective inlet diameter	30
Figure 2-21 Change in $K_{ct}$ for different cooling tower inlet geometries compared to a sharp inlet	32
Figure 2-22 Change in $d_{ie}/(d_i+2t_s)$ for different inlet geometries compared to a sharp inlet	33
Figure 2-23 Path-line plots coloured by velocity magnitude, for platforms and a rounded inlet	34
Figure 3-1 Drag coefficient of circular cylinder for smooth and rough cylinders (17)	39
Figure 3-2 Illustration of different definitions for mesh refinement in the wake region	41

Figure 3-3	Coordinate system for cylinder analysis	42
Figure 3-4	Difference in flow patterns between refinement and no refinement in the wake area	42
Figure 3-5	Effect of boundary layer grid type on the pressure and drag coefficients	43
Figure 3-6	Comparison of different turbulence models for the two-dimensional cylinder model	44
Figure 3-7	Comparison of the different methods of grid refinement in the wake	46
Figure 3-8	Comparison of cylinder surface pressure coefficient for different grid refinements in the wake with $Y = m$	47
Figure 3-9	Comparison of wake refinement results with $Y = m$	48
Figure 3-10	Comparison of cylinder parameters for different turbulence parameters	49
Figure 3-11	Comparison of results for cylinder surface roughness of $k_s/D = 1.5 \times 10^{-3}$	50
Figure 3-12	Comparison of averaged pressure coefficient results from Fluent with literature for an infinite smooth circular cylinder	52
Figure 3-13	Illustration of the three dimensional grid for the finite circular cylinder investigation	52
Figure 3-14	Comparison between the surface pressure distribution and drag coefficients of finite and infinite cylinders	53
Figure 3-15	Comparison of rough circular cylinder pressure coefficient distribution from Fluent with experimental data from literature	54
Figure 3-16	Velocity vector plots at different planes for an infinite and finite cylinder	55
Figure B-1	Schematic of wind tunnel used in experiments courtesy of Kröger (1)	65
Figure B-2	Dimensions of the static pressure probe	67
Figure B-3	Pressure probe position in the CTSM	67
Figure D-1	Illustration of Measurement Technique	73
Figure E-1	Domain of the axi-symmetric Fluent model developed to simulate the sector model experiment	78



## List of Tables

		Page
Table 2-1	Power function coefficients for equation (2-21)	17
Table 2-2	Number of cells for different starting cell sizes	19
Table 2-3	Comparison of the results for triangular and quadrilateral meshes with $d_i/c = 696.67$	20
Table 2-4	Comparison of the results for different turbulence models	21
Table 2-5	$K_{ct}$ results at different values of Re obtained using Fluent	23
Table 2-6	Tower inlet loss coefficients for sharp inlet with $K_{he} = 14.3$ for different ratios of $d_i/H_i$	24
Table 2-7	Fluent loss coefficient and effective diameter data for cylindrical and conical tower walls	25
Table 2-8	Fluent model with an inclined shell compared to equation (2-9), which is based on a cylindrical shell, with $K_{he} = 12$	28
Table 2-9	Tower inlet loss coefficients for protruding platforms and rounded inlets with $K_{he} = 14.3$	30
Table 2-10	Sharp inlet loss coefficient for $K_{he} = 11.32$ and different $d_i/H_i$ ratios determined using Fluent	31
Table 2-11	Effective diameter ratio for the sharp inlet	32
Table 2-12	Full-scale Fluent results for different cooling tower inlet geometries with $K_{he} = 12$ and $d_i/H_i = 10.45$	35
Table 3-1	Different regimes encountered for flow around a smooth cylinder (18)	38
Table B-1	Data for pressure calibration of the probe	68
Table B-2	Data for probe sensitivity to angle of attack	68
Table C-1	Fill experimental data run 1: Honeycomb	70
Table C-2	Fill experimental data run 1: One layer of mesh	70
Table C-3	Fill experimental data run 1: One layer of mesh and Honeycomb	71
Table C-4	Fill experimental data run 1: One layer of mesh and Honeycomb	71
Table C-5	Fill experimental data run 1: Two layers of mesh	71
Table C-6	Fill experimental data run 2: One layer of mesh	71
Table C-7	Fill experimental data run 2: One layer of mesh with Honeycomb	71
Table C-8	Fill experimental data run 2: One layer of mesh with honeycomb	72
Table C-9	Fill experimental data run 2: Two layers of mesh with honeycomb	72
Table C-10	Fill experimental data run 3: Two layers of mesh with honeycomb	72
Table D-1	Incremental Area Data	75
Table D-2	Experimental data for Sharp inlet ( $d_i/H_i = 10.45$ )	75
Table D-3	Experimental data for Sharp inlet ( $d_i/H_i = 11.61$ )	75
Table D-4	Experimental data for sharp inlet ( $d_i/H_i = 13.06$ )	75
Table D-5	Experimental data for walkway ( $X \times Y = 0 \times 1.8\text{m}$ )	76
Table D-6	Experimental data for walkway ( $X \times Y = 0 \times 3.6\text{m}$ )	76
Table D-7	Experimental data for walkway ( $X \times Y = 0 \times 7.2\text{m}$ )	76
Table D-8	Experimental data for rounded inlet ( $r_i/d_i = 0.025$ )	77
Table E-1	Data from CFD for further manipulation	79
Table E-2	Sharp inlet Input parameters for Fluent	81
Table E-3	Sharp inlet output from Fluent for $d_i/H_i = 6$	81
Table E-3	Sharp inlet output from Fluent for $d_i/H_i = 6$	81

Table E-4	Sharp inlet output from Fluent for $d_i/H_i = 6.97$	81
Table E-5	Sharp inlet output from Fluent for $d_i/H_i = 8.71$	82
Table E-6	Sharp inlet output from Fluent for $d_i/H_i = 10.45$	82
Table E-7	Sharp inlet output from Fluent for $d_i/H_i = 11.61$	82
Table E-8	Sharp inlet output from Fluent for $d_i/H_i = 13.06$	83
Table E-9	Sharp inlet output from Fluent for $d_i/H_i = 14.93$	83
Table E-10	Added structures input parameters for Fluent	84
Table E-11	Added structures at the inlet output from Fluent for $d_i/H_i = 8.708$	84
Table E-12	Added structures at the inlet output from Fluent for $d_i/H_i = 10.45$	84
Table E-13	Added structures at the inlet output from Fluent for $d_i/H_i = 11$	85
Table E-14	Added structures at the inlet output from Fluent for $d_i/H_i = 11.611$	85
Table E-15	Added structures at the inlet output from Fluent for $d_i/H_i = 12.294$	85
Table E-16	Added structures at the inlet output from Fluent for $d_i/H_i = 13.063$	86
Table E-17	Added structures away from the inlet output from Fluent for $d_i/H_i = 8.708$	86
Table E-18	Added structures away from the inlet output from Fluent for $d_i/H_i = 10.45$	86
Table E-19	Added structures away from the inlet output from Fluent for $d_i/H_i = 11$	87
Table E-20	Added structures away from the inlet output from Fluent for $d_i/H_i = 11.611$	87
Table E-21	Added structures away from the inlet output from Fluent for $d_i/H_i = 12.294$	87
Table E-22	Added structures away from the inlet output from Fluent for $d_i/H_i = 13.062$	88

# Nomenclature

## List of Symbols

a	Coefficient as per equation (2-21)
B	Distance from bottom of cylinder as shown in Figure 3-3, m
b	Coefficient as per equation (2-21)
$b_1$	Parameter as defined in equation (D-3)
$b_2$	Parameter as defined in equation (D-4)
C	Coefficient
$C_n$	Coefficient as defined in equation (B-2)
c	Reference size of first cells used at inlet of NDCT Fluent model, m
D	Diameter, m
E	Distance from centre of cylinder to downstream position as shown in Figure 3-3, m
F	Distance from centre of the cylinder parallel to the flow field in the horizontal direction as shown in Figure 3-3, m
H	Height, m
$h_1$	Parameter as defined in equation (D-1)
$h_2$	Parameter as defined in equation (D-2)
I	Axis parallel to flow direction as shown in Figure 3-3
J	Axis perpendicular to flow field in the horizontal direction as shown in Figure 3-3
K	Loss coefficient
$K_p$	Pressure relation coefficient
k	Thermal conductivity,
$k_s$	Sand grain roughness height, mm
$\ell$	Turbulence length scale, m
L	Axis perpendicular to flow field in the vertical direction as shown in Figure 3-3
m	Mass flow rate, kg/s
q	Heat input, J/kg
P	Pitch, mm
p	Static pressure, Pa
r	Radius to specific point in CTSM, m
$T_i$	Turbulence intensity
$t_s$	Tower wall thickness, m
u	Internal energy, J/kg
v	Velocity, m/s
$w_v$	Viscous work, J/kg
$w_s$	Shaft work, J/kg
X	Ratio of cylinder diameter to starting cell height on cylinder boundary
x	Place holder
Y	Parameter designating which surfaces where used in refining the wake behind the cylinder as shown in Figure 3-2, Velocity factor
$y^+$	Wall boundary layer parameter
Z	Ratio of the cylinder diameter to the starting cell height on the refinement surfaces in the wake of cylinder as shown in Figure 3-2.
z	Height

### **Greek Symbols**

$\alpha_e$	Kinetic energy correction factor
$\beta$	Porosity
$\Delta$	Differential
$\phi$	Gas expansion factor
$\delta(x)$	Deviation percentage
$\mu$	Dynamic viscosity
$\varphi$	expansion factor
$\rho$	Density
$\sigma$	surface tension
$\theta$	Angle from reference as shown in Figure 3-3
$\omega$	Frequency, radians/s

### **Subscripts**

1	Position with respect to cooling tower shell, as according to Figure 1-1 and Figure D-1
2	Position with respect to cooling tower shell, as according to Figure 1-1 and Figure D-1
3	Position with respect to cooling tower shell, as according to Figure 1-1
4	Position with respect to cooling tower shell, as according to Figure 1-1
5	Position with respect to cooling tower shell, as according to Figure 1-1
a	Ambient, air
ax	Axial
c	critical
ct	Inlet loss
cyl	cylinder
D	Drag
f	fluid
fr	Frontal area
g	gas
he	Heat exchanger
i	Inlet
ie	Effective inlet
m	Mean
n	Nozzle
p	Pressure
q	counter
r	Radial
ref	Reference
s	Tower shell, Static pressure
scr	Screen
tus	Section between nozzles and inlet. Appendix B
up	Upstream of nozzles. Appendix B
v	vapour
vc	vena contracta
x	Place holder

**Dimensionless groups**

Re	Reynolds number,	$\frac{\rho v d}{\mu}$
St	Strouhal number,	$\frac{\omega d}{2\pi v}$

**Abbreviations and acronyms**

MDCT	Mechanical Draft Cooling Tower
NDCT	Natural Draft Cooling Tower
NDWCT	Natural Draft Wet Cooling Tower
NDDCT	Natural Draft Dry Cooling Tower
CFD	Computational Fluid Dynamics
CTSM	Cooling Tower Scale Sector Model
RMS	root mean square

# 1 Introduction

Industrial cooling systems are required to effectively reject waste heat from process plants to the environment. The typical systems that require heat rejection are refrigeration, chemical, process, combustion and power generation plants (1). In the past, the most common method of cooling was by means of the hydrosphere, which involves water from a natural resource being passed through a heat exchanger and returned to the source at an increased temperature. Most countries have legislation which limits the increase in temperature of the cooling water used due to the negative impact on the environment. This environmental issue, the shortage of natural resources and the increasing cost of water has limited the use of natural water for once-through cooling.

An alternative is to reject the heat to the atmosphere. Passing heat to the atmosphere is accomplished with the aid of cooling towers. Cooling towers are classified as either dry or wet. Wet-cooling towers allow the cooling water to come in direct contact with the air and heat is transferred by means of convection and evaporation. These towers are utilized in areas where there is a sustainable and economical water supply. In dry-cooling towers, cooling is accomplished by means of convective heat transfer by utilizing finned tube heat exchangers to reject heat to the atmosphere, i.e. air. These towers are also generally used where the process fluid, which needs cooling, is at a temperature higher than 60°C (1) since large heat rejection is required. For increased heat rejection, the size or number of MDCTs increases which means that larger or more fans are required. This constitutes the need for more auxiliary power to drive these fans and thus increases the running cost of these towers.

## 1.1 Background

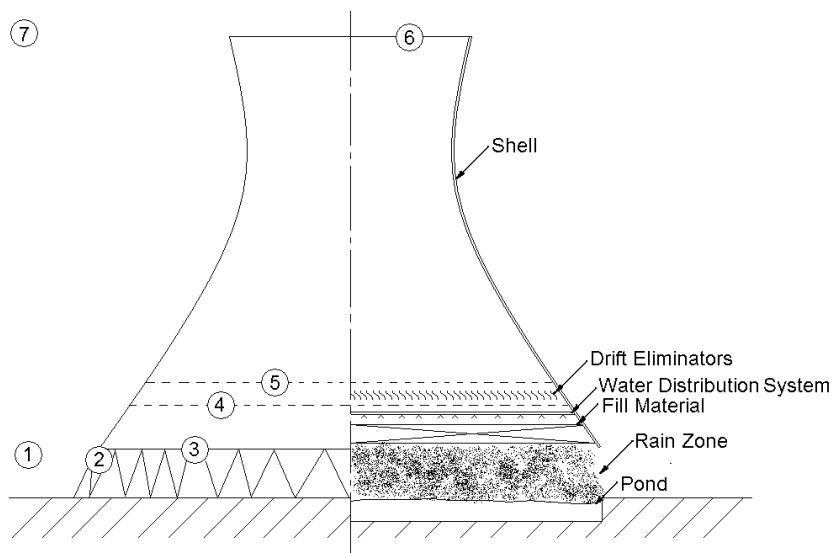


**Figure 1-1 Schematic of a counter flow NDWCT**

Figure 1-1 depicts a natural draft wet-cooling tower (NDWCT). The tower consists of a tower shell, tower supports, drift eliminators, a water distribution system with

supporting structure, fill with supporting structure and the pond. The drift eliminators catch small droplets entrained into the air flow, which form larger drops that fall back to the fill. These functions to minimize the make-up water needed and prevents pollution of the environment by not allowing the products in the water to escape. Depending on the design and operating conditions, different fill types and nozzles can be installed in the cooling tower to maximize the cooling tower performance. The fill/packing can also be installed in a cross flow configuration around the circumference of the tower inlet. The numbers in Figure 1-1 are used to identify different positions within and around the tower, which will be referenced later on in the document.

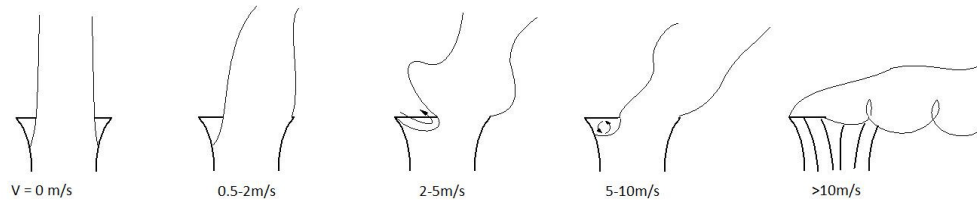


**Figure 1-2 Plume flow patterns observed at the outlet of a cooling tower at different wind speeds (1)**

Figure 1-2 depicts the flow patterns at the outlet of a cooling tower in the presence of a crosswind. Studies on NDCTs subjected to crosswinds show that there is a rise in water temperature with increased wind speed in both wet- and dry- cooling towers (1). These studies also indicate that a counter flow configuration for the fill/packing or heat exchangers is less sensitive to the effect of the crosswind than the cross flow configuration. The rise in water temperature is a result of poor distribution of and a decrease in the air flow into the fill or heat exchangers for the counter flow configuration. Fill and heat exchangers installed in a cross flow configuration experience oblique flow under crosswind conditions, which decreases the amount of air entering these sections and decreases the performance of the tower.

Performance engineers generally use one-dimensional theoretical models for the design of cooling towers. The relevant theory and sample calculations for different types of cooling systems are presented in Kröger (1). These models can predict the three-dimensional effects of crosswinds on the airflow through the towers and subsequent effects on performance to some extent if the specified assumptions hold true. The aim of this thesis is to lay the ground work for developing a three-dimensional numerical model of a NDCT in order to investigate the influence of crosswinds on the performance of such a tower using the commercial CFD code, Fluent 3.6.26. With the aid of Fluent it is possible to simulate any type of geometry for a tower shell and also simulate the effects of different types of fills before actually building a tower.

## 1.2 Motivation

Cooling towers are essential for the efficient functioning of the thermal system into which they are incorporated. To illustrate this point the example of a power generation plant is considered. If a power plant's efficiency can be increased by 1% it will amount in a significant cost reduction. This project will enable better understanding of cooling towers and the flow patterns in these towers due to

atmospheric conditions. A better understanding of cooling tower performance will result in improved designs and higher power plant efficiency.

The sheer physical size of a cooling tower and uncontrollable operating conditions make it difficult to conduct tests on full-scale towers (1). Thus scale models are used to measure and investigate the flow patterns through the NDCTs in a controlled environment. Scale models pose the problem of not adhering to both the Reynolds and densimetric Froude numbers at the same time and thus are modelled isothermally to overcome this problem. The draft is achieved by means of fans. Although this method allows the main fluid velocities to be determined, it is difficult to achieve the Reynolds numbers observed for real NDCT for these models due to wind tunnel limitations, such as a lack of the required volume flow rate. This increases the appeal of using a numerical model due to the ease of construction and since such a method will meet all similitude requirements.

After a better understanding is gained of the flow through a cooling tower, the life cycle costs of new and existing cooling towers can be reduced by decreasing the size for a given heat load or improving the efficiency.

### **1.3 Objectives**

To develop a CFD model for simulating the performance of a NDCT under crosswind conditions, the following flow aspects need to be investigated and validated: flow separation and reattachment at the inlet of the tower, the flow patterns at the tower outlet and flow patterns and pressure distribution around a cylinder. The accuracy with which each of these aspects can be solved will determine the overall accuracy of the model. In this thesis emphasis is placed on the flow into the tower with no crosswind and the flow characteristics around a cooling tower in the presence of a crosswind. A literature review is conducted to find available research data on these topics. The main objectives of this thesis are to:

- Create 2-D (axis-symmetric) Fluent models of cooling tower inlets and compare the results with experimental data.
- Investigate the effects of different cooling tower inlet geometries on the cooling tower inlet loss coefficient and effective flow diameter.
- Create two-dimensional (2-D) and three dimensional (3-D) CFD models to predict the air flow and pressure field around a cylinder and compare the results to data found in literature.

### **1.4 Scope of work**

In order to gain a better understanding of the flow fields inside and around a NDCT through modelling, one must be aware of the capabilities of the CFD package being used. For this reason it is necessary to verify the CFD results using experimental or theoretical data. The validation procedure is as follows:

1. Use a scale model of a tower section to predict the inlet losses experimentally.
2. Develop a two-dimensional axi-symmetric CFD model of the experimental apparatus using Fluent and compare the results to the experimental data as well as data from literature.



3. Modify the inlet design and configuration of both the experimental apparatus and Fluent to investigate the effects on the loss coefficient and effective diameter.
4. Investigate Fluent's capability to model the flow around an infinite and circular cylinder of finite length

## **1.5 Thesis layout**

This section presents the basic layout of the thesis and provides a short synopsis of each chapter.

### **Chapter 1: Introduction**

A brief background of natural draft cooling towers is given and the effect wind has on the performance of these structures is discussed. The motivation, objectives, scope of work and a summary of the thesis layout is given.

### **Chapter 2: Modelling of cooling tower inlets**

Experimental work is conducted on a scale sector model of a cooling tower. A two-dimensional (axi-symmetric) model is developed in Fluent and the results are validated with the measured data. A comparison between available data from literature and the Fluent models are given. Structures are added to the inlet of the Fluent model to determine their effect on the inlet loss coefficient and effective diameter of the tower.

### **Chapter 3: Modelling of flow around a cylinder**

Fluent's capability of modelling the flow around an infinite and finite circular cylinder is investigated. The infinite cylinder is modelled two-dimensionally with varying surface roughness. Different turbulence models, grid independence, turbulence intensities and length scales are investigated. A finite cylinder with a rough surface is constructed from the experience gained from the infinite cylinder model to investigate the three-dimensional effects that occur. The results for both finite and infinite cylinders are compared to experimental data from literature.

### **Chapter 4: Conclusion and Recommendations**

This chapter consists of conclusions and recommendations which are based on the results in this thesis.

## 2 Modelling of cooling tower inlets

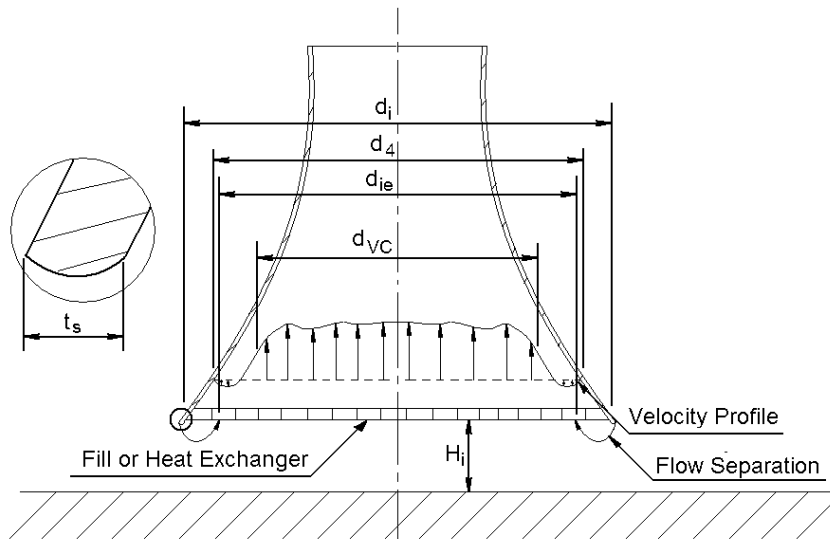


**Figure 2-1 Schematic of a NDCT showing the velocity profile and vena contracta inside the tower**

Cooling tower inlet losses are defined as flow losses due to viscous dissipation of mechanical energy caused by shear stresses present in the air flow which are directly affected by the inlet geometry. The shear stresses are caused by the velocity gradients in the fluid which are present due to flow separation while the fluid turns nearly  $180^\circ$  when entering the tower. Decreasing these shear stresses and the turbulent separation zone will result in lower tower inlet losses, which increases the mass flow rate of air entering the tower and the heat rejection capability of the tower.

Turbulent flow separation at the entrance of the tower causes a recirculation zone where limited heat transfer takes place. This leads to the introduction of the effective flow area which is defined as the area at the fill outlet where a mass balance is achieved between the air entering the tower and the air leaving the outlet of the fill, by mathematical integration from the centre of the cooling tower. The size of the effective area is determined by the size of the recirculation zone and thus it can be deduced that by reducing the recirculation zone, the effective area can be improved resulting in increased performance of the tower.

Cooling tower inlet losses have been studied by a number of researchers [ (1), (2), (3), (4), (5)]. The majority of researchers make use of scale model tests to study the flow characteristics inside a NDCT due to the complexity of full-scale tests owing to uncontrolled variable atmospheric conditions and the physical size of a NDCT. When conducting a model test using a wind tunnel, the dimensions and shape of the model must ideally be geometrically proportional to the full-scale structure and the Reynolds and Froude numbers must be of the same order of magnitude while maintaining incompressible flow. Most experimental investigations of cooling tower inlets do not satisfy dimensional and geometrical similitude (6).

Geldenhuys (3) used a 1:20 scale sector model (sector angle of  $5^\circ$ ) to measure inlet loss coefficients up to a Reynolds number of  $10^6$ . Although this value is one order of

magnitude smaller than Reynolds numbers typically encountered in a NDCT, he proves that varying the order of magnitude of the Reynolds number has a negligible effect on the measured inlet loss coefficients. The heat exchanger/fill was simulated using an actual small fin pitch radiator core, which satisfies the geometrical equivalence to a NDDCT, such as Kendal, and NDWCT's with film type packing which has an orthotropic resistance. The wall of this model represents a cylindrical cooling tower, which differs from a typical NDCT with conical or inclined walls at the inlet. The base of the model, which represents the ground or pond, is height adjustable to enable the  $d_i/H_i$  ratio of the scale sector model to be varied. The pressure and axial velocity is measured directly downstream of the heat exchangers cores. Geldenhuys (6) determined the inlet loss coefficient from pressure drop and velocity data whilst ignoring the effect of the non-uniform velocity profile.

Terblanche and Kröger (4) used the same sector model and wind tunnel as Geldenhuys (3) but in addition measured the velocity profile downstream of the heat exchanger to determine the effect of the kinetic energy coefficient on the inlet loss coefficient and to determine the effective diameter. De Villiers (2) also measured and simulated the inlet loss coefficient and effective diameter for an isotropic fill resistance using the sector model of Geldenhuys. The simulations were carried out using the commercial CFD code Star-CD and he validated his two dimensional models using the experimental results.

To develop a successful CFD model with the aid of Fluent, the parameters that influence the results need to be investigated. These include the grid size, turbulence models, influence of solving the boundary layer, turbulence intensity and turbulence length scale. Data obtained from literature is used to verify the numerically simulated inlet loss and effective flow area. The data is also used to determine if it will be possible to reduce the inlet loss coefficient and increase the effective flow area, to enhance the performance of the tower. Kröger (1) showed that a rounded inlet can be used to reduce inlet losses and increase the effective flow area. In this chapter a validated CFD model is developed to simulate the inlet losses and effective flow area of a NDCT with the aid of Fluent in order to obtain a better understanding of the flow patterns inside the tower and to study the effect that modification to the inlet geometry has on the inlet loss coefficient and the effective flow area.

From a sample calculation given by Kröger (1), it is noted that the inlet losses may represent more than a quarter of the total losses occurring in a cooling tower. By reducing inlet losses and increasing the effective flow area the tower performance and power plant efficiency could increase significantly. The objectives of this chapter are therefore to develop and validate a Fluent model of a cooling tower inlet; to determine the inlet loss coefficient and the effective flow area for a given cooling tower geometry; and to use this model to investigate the effect of different inlet geometries on the inlet loss coefficient and effective flow area.

The results of the Fluent model and the experimental sector model are presented in dimensionless form with the pressure relation coefficient, loss coefficient, velocity ratio and deviation percentage to simplify the comparison with other experimental data. The chapter consists of the following sections:

- Introduction: This section gives the general background for investigating cooling tower inlet losses.

- Theory: In this section the relevant theory applicable to inlet losses and effective flow area is presented.
- Experimental work: This section contains experimental setup, measurement technique, test procedure and results for the investigation into the material used to simulate the heat exchangers and packing material and the scale sector model.
- Modelling procedure: In this section different turbulence models, grid size, type of cell, turbulence intensity and turbulence length scale are investigated to determine their effect on the numerical results, and the results are interpreted.
- Tower modelling results: This section consists of a comparison between Fluent and the experimental results, comparison of the Fluent results with literature, the validation of the Fluent model with experimental results for added geometries to the tower and the results of the Fluent investigation into added geometries.
- Discussion of the results: In this section a summary of the chapter's findings is presented.

## 2.1 Theory

The total losses inside a NDCT include the inlet loss and the various flow resistances such as support structures and heat exchangers inside the tower. Figure 2-1 provides a schematic representation of the flow inside a NDCT and illustrates how the separation at the tower inlet edges causes the formation of a vena contracta. The vena contracta diameter ( $d_{vc}$ ) is defined as the diameter where a mass balance is reached between the air flow crossing the area under investigation and the air entering the tower, where the mass flow rate above the packing is determined by integration of the velocity profile from the tower axis. This definition is similar to that of the effective diameter ( $d_{ie}$ ) but the vena contracta can be measured at any level inside the tower whereas the effective diameter is measured directly downstream of the heat exchangers. To determine the inlet loss coefficient the steady state energy equation is used (7), which is as follows:

$$\frac{p_1}{\rho} + \frac{\alpha_{e1} v_1^2}{2} + z_1 g + u_1 = \frac{p_4}{\rho_4} + \frac{\alpha_{e4} v_4^2}{2} + z_4 g + u_4 + q + w_s + w_v \quad (2-1)$$

where  $p_1$  and  $p_4$  are the static pressures;  $\alpha_{e1}$  and  $\alpha_{e4}$  are the kinetic energy correction factors;  $v_1$  and  $v_4$  are the velocities;  $z_1$  and  $z_4$  are the heights above a reference plane;  $g$  is gravitational acceleration;  $q$  is heat added to the system;  $w_s$  is the shaft work;  $w_v$  is the work done by the viscous stresses on the control surface;  $u_1$  and  $u_4$  are the internal energies; and  $\rho_1$  and  $\rho_4$  are the densities where the location of planes 1 and 4 are shown in Figure 1-1. The variables used in equation (2-1) are mean values at the representative locations.

During this investigation a horizontal scale sector model is utilized, as depicted in Figure 2-5, to validate the Fluent models. For this configuration and under isothermal conditions, the following assumptions apply to equation (2-1):

- There is no change in elevation due to the tower model's horizontal position.

- There is no shaft work since the control volume does not incorporate the wind tunnel.
- There is no energy added or removed from the control volume.
- No work is done by the viscous stresses since the velocity is zero at the surface of the control volume.
- Point 1 is far away from the tower where the velocity is zero.
- The change in internal energy is represented by loss coefficients in the form of  $\sum K \frac{v^2}{2} = u_4 - u_1$ .
- The loss coefficients that are present in the experimental tower sector model are the inlet loss coefficient ( $K_{ct}$ ) and the loss coefficient of the simulated heat exchanger ( $K_{he}$ ). Both of these loss coefficients are normalized to the heat exchanger inlet velocity and area.
- In normal circumstances the heat exchanger does not cover the entire inlet area and thus, along with the change in density, must be specifically adjusted by  $A/A_{fr}$ .
- Point 4 is taken directly downstream of the heat exchanger in order to take the vena contracta that forms into account.

With the above assumptions equation (2-1) simplifies to:

$$\frac{p_1}{\rho_1} = \frac{p_4}{\rho_4} + \frac{\alpha_{e4} v_{vc4}^2}{2} + \left[ K_{ct} + K_{he} \left( \frac{\rho_1}{\rho_{he}} \right) \left( \frac{A}{A_{fr}} \right)^2 \right] \frac{v_i^2}{2} \quad (2-2)$$

where A is the cross sectional area directly downstream of the heat exchangers,  $A_{fr}$  is the frontal area of the heat exchanger,  $\rho_1$  is the density of air entering the heat exchanger,  $v_i$  is the average inlet velocity into the heat exchanger and  $\rho_{he}$  is the average density of the air flowing through the heat exchanger. Rearranging equation (2-2) yields the following relation for the inlet loss coefficient:

$$K_{ct} = \frac{p_1 - (\bar{p}_4 + 0.5\alpha_{e4}\rho_4 v_{vc4}^2)}{0.5\rho_1 v_i^2} - K_{he} \left( \frac{\rho}{\rho_{he}} \right) \left( \frac{A}{A_{fr}} \right)^2 \quad (2-3)$$

The average pressure at the measured level is determined with a volume flow weighted average, defined as:

$$\bar{p} = \left( \int p \cdot dQ \right) / \bar{Q} \quad (2-4)$$

The mean velocity at any level, represented by the x, is defined as:

$$v_x = m / \rho A_x \quad (2-5)$$

The mean velocity of the vena contracta is determined from:

$$v_{vc4} = \frac{\int_{A_{vc}} v \cdot dA}{A_{vc}} \quad (2-6)$$

The kinetic energy of flow with a non-uniform velocity profile differs from that of uniform flow. The kinetic energy velocity distribution correction factor ( $\alpha_{e,vc}$ ) takes into account this non-uniformity. The integral is taken over the total area of the vena contracta and is defined by the following equation:

$$\alpha_{e,vc} = \frac{\frac{1}{m} \int \frac{1}{2} v^2 \cdot dm}{\frac{1}{2} v_{vc4}^2} = \frac{\int_{A_{vc}} v^3 \cdot dA}{A_{vc} v_{vc4}^3} \quad (2-7)$$

Geldenhuys [(3), (6)] simplifies equation (2-3) by assuming  $\alpha_{e,4} = 1$ ,  $v_{vc4} = v_{m4} = m/\rho A_4$ , constant density and  $A/A_{fr} = 1$ , which yields:

$$K_{ct} = \frac{p_a - (p + 0.5\rho v_{m4}^2)}{0.5\rho v_i^2} - K_{he} \quad (2-8)$$

Using equation (2-8) and experimental data for the inlet loss coefficient, Geldenhuys (6) proposes the following empirical equation:

$$K_{ct} = \frac{0.05[d_i/H_i]^{2.24+0.0255d_i/H_i}}{K_{he}^{0.12+0.018d_i/H_i}} + 0.4 \quad (2-9)$$

valid for  $10 \leq K_{he} \leq 45$  and  $0 \leq d_i/H_i \leq 15$ .

Terblanche and Kröger (4) used the same sector model test section as Geldenhuys (6) and measured the velocity profile downstream of the packing material to improve the accuracy of the loss coefficient by including the kinetic energy correction coefficient and the average vena contracta velocity. Equation (2-3) is used to evaluate the inlet loss coefficient and the following empirical equation based on experimental data is proposed:

$$K_{ct} = \left[ 100 - 18 \left( \frac{d_i}{H_i} \right) + 0.94 \left( \frac{d_i}{H_i} \right)^2 \right] \times K_{he}^{\left( -1.28 + 0.183 \left( \frac{d_i}{H_i} \right) - 7.769 \times 10^{-3} \left( \frac{d_i}{H_i} \right)^2 \right)} \quad (2-10)$$

for  $10 \leq d_i/H_i \leq 15$  and  $5 \leq K_{he} \leq 25$ , where  $\left( \frac{d_i}{H_i} \right)$  is the ratio of the inlet diameter to the inlet height and  $K_{he}$  is the loss coefficient of the fill.

Oosthuizen (8) also used Geldenhuys's (6) sector model to determine the effective flow area and to measure the velocity profiles downstream of the packing. He proposed an empirical equation for the effective diameter using experimental data, presented by Kröger (1) as:

$$\frac{d_{ie}}{d_i + 2t_s} = 1.2549 - 0.21069 \ln \left( \frac{d_i + 2t_s}{H_i} \right) + \left[ 0.050673 \ln \left( \frac{d_i + 2t_s}{H_i} \right) - 0.052085 \right] \ln K_{he} \quad (2-11)$$

for  $5.35 \leq (d_i + 2t_s)/H_i \leq 16$ ,  $3.6 \leq K_{he} \leq 49$  and  $d_{ie}/d_i \leq 1$ , where  $t_s$  is the tower shell thickness at the inlet. The wall thickness is added to the term below the line on the right hand side, since the effective diameter ratio is defined as the effective diameter divided by the diameter of the point of flow separation at the inlet, which is at the outer sharp edge

The results displayed in this chapter are presented in dimensionless form. The pressure relation coefficient  $K_p$ , is the Euler number which relates the static pressure difference, relative to a reference pressure, to the dynamic pressure at the fill inlet, is represented by:

$$K_p = \frac{p - p_{ref}}{0.5\rho v_i^2} \quad (2-12)$$

where  $p$  is the pressure being evaluated,  $p_{ref}$  is the reference pressure,  $\rho$  is the reference density and  $v_i$  is the average inlet velocity.

The equation for the deviation percentage is:

$$\delta(x) = \left[ \frac{(x - x_{ref})}{x_{ref}} \right] \times 100\% \quad (2-13)$$

where  $x$  is the parameter being evaluated and  $x_{ref}$  is the reference value for that parameter.

## 2.2 Experimental Work

Experimental work is an integral part of validating the Fluent models. The wind tunnel, as described in Appendix B, is used in all the following experiments.

### 2.2.1 Determining packing material characteristics

#### (a) Design criteria of the test rig

The design criteria for the test rig are as follows:

- Air flow needs to be variable, measured, uniform and perpendicular to the packing.
- The pressure drop over the test material must be measured.
- Material should have a loss coefficient of between 11 and 19.

#### (b) Description of the test rig

The test rig consists of a bell mouth inlet and two cylindrical pipe sections ( $d = 0.3\text{m}$ ) joined by two flanges, as depicted in Figure 2-2. The bell mouth ensures a uniform velocity profile in the test section and could be used as a second flow meter to verify the measured volume flow rate of the wind tunnel. This is however not practical in this case due to low air speed. The pipes are attached to the wind tunnel by means of a flange.

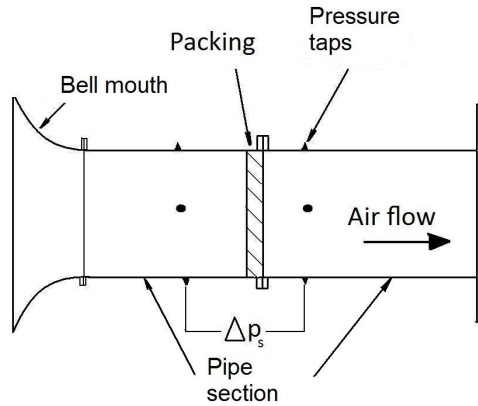


**Figure 2-2 Schematic of the test section for measuring the packing loss coefficient**

The material to be tested is clamped between the two pipe flanges, to prevent it from being sucked down the pipe and the static pressure is measured upstream and downstream of the material. The loss coefficient is determined by using equation (2-1) and it is assumed that: the velocity on both sides of the packing is the same; no heat transfer or work is introduced into the system, the pipe friction losses are negligible and there is no change in height or internal energy. From equation (2-1) and these assumptions the packing loss coefficient can be expressed as:

$$K_{scr} = \frac{2\Delta p_{scr}}{\rho v^2} \quad (2-14)$$

### **(c) Measurement technique used for the test rig**

Four static pressure taps are positioned around the outside of the pipe at 90° angles to determine the static pressure at the walls. An average reading is taken by connecting the four taps. Due to spatial constraints, the taps are placed one pipe diameter upstream of the material and a third of a diameter downstream. This is not a desirable configuration because the static pressure measurement might be influenced by unstable flow patterns or by being in the wake of an obstruction. However, it is proven later that the results are acceptable when compared to equations and data from literature.

### **(d) Test procedure of the test rig**

The following steps are taken to determine a correlation between the loss coefficient and the velocity of the air flow through the material:

- Set the fan speed on desired frequency with the aid of a frequency converter.
- Measure the static pressure drop over the packing material.
- Measure the static pressure drop over the nozzles in the wind tunnel.
- Measure the pressure in front of the nozzles in the wind tunnel.
- Adjust the speed of the fan.

These steps are repeated until the maximum setting for the fan speed is reached where a new configuration is inserted and the test is repeated.



### (e) Results gained from test rig

A wire mesh with a pitch of 0.4 mm and a wire diameter of 0.173 mm is tested. A piece of aluminium honey comb material is added to lend rigidity to the wire mesh and is tested separately to determine the effect on the fill loss coefficient. The wire mesh is tested in 4 configurations and the experiment is repeated three times to establish repeatability:

Test 1: Mesh by its self.

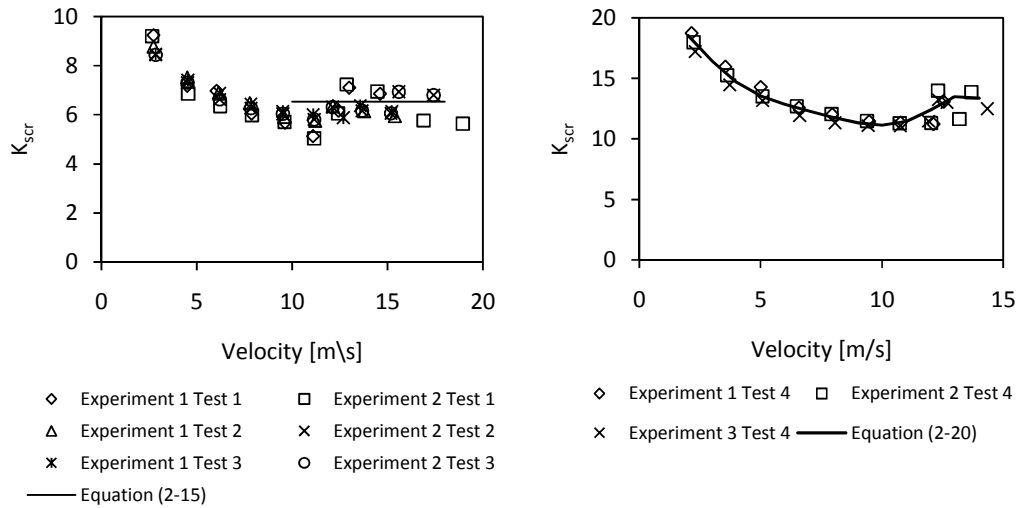
Test 2: Mesh with honey comb structure upstream of the packing.

Test 3: Mesh with honey comb structure downstream of the packing.

Test 4; Mesh on both sides of the honey comb structure.

It is found that the loss coefficient of the honey comb is very small, with the highest value being  $K = 0.29$  at a velocity of 15m/s. When the velocity is increased further, the loss coefficient decreases. Thus the loss coefficient is neglected since it is less than 5% of the value of the wire mesh.

Figure 2-3 (a) illustrates the loss coefficients measured for one layer of wire mesh and different configurations, which indicate that the position of the honey comb does not have a significant overall effect on the loss coefficient of the mesh. To determine the validity of these results, a comparison is made to the following set of equations by Simmons (9) for the loss coefficient of a wire mesh, found in Kröger (1). The wire mesh loss coefficient is defined as:



(a) Different combinations of honey comb.

(b) Two layers of mesh with honeycomb in between.

Figure 2-3 Experimentally determined wire mesh loss coefficient data

$$K_{scr} = \frac{1 - \beta_{scr}}{\beta_{scr}^2} \quad (2-15)$$

where the porosity of a wire mesh,  $\beta_{scr}$ , is defined as the relation of open area to that of the total area of the screen and is presented as:

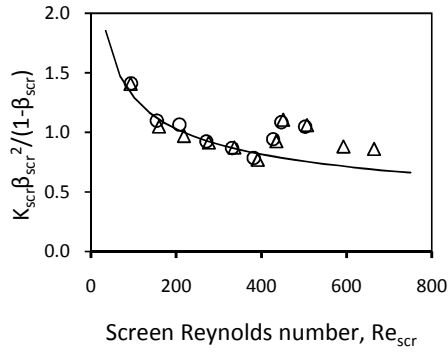
$$\beta_{scr} = \frac{A_{open}}{A_{total}} = \left(1 - \frac{d_{scr}}{P_s}\right)^2 \quad (2-16)$$

where  $d_s$  is the wire diameter and  $P_s$  is the pitch of the wires. Equation (2-15) is only valid for an air stream velocity above 10 m/s with the air flow perpendicular to the wire mesh. This equation predicts a loss coefficient of 6.53 for the current mesh, which correlates well with experimental values. According to Wieghardt (10), the loss coefficient for different screen Reynolds numbers is expressed as:

$$K_{scr} = \frac{6(1 - \beta_{scr})}{\beta_{scr}^2 Re_{scr}^{0.333}} \quad (2-17)$$

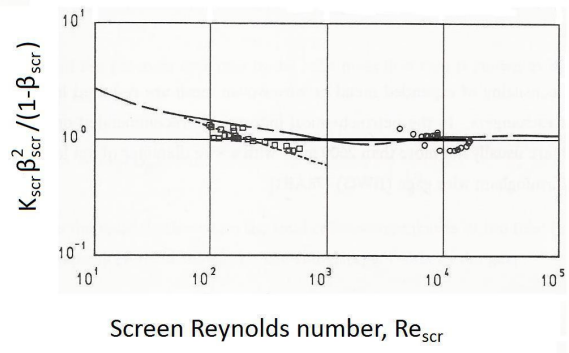
and is valid for  $60 < Re_{scr} < 1000$ . The screen Reynolds number ( $Re_{scr}$ ) is based on the free stream velocity and is defined as:

$$Re_s = \frac{\rho v d_s}{\beta_s \mu} \quad (2-18)$$



○ Experiment 1 Test 1    △ Experiment 2 Test 1  
— Equation (2-17)

(a) Measured data compared to equation (2-17)



--- Equation (2-19)    ..... Equation (2-17)  
— Equation (2-15)    □ Derbunovich et.al (11)  
○ Cornell (12)

(b) Measured data compared to cylinder drag coefficient (Kröger (1))

**Figure 2-4 Comparison of experimental wire mesh loss coefficient data to literature**

Figure 2-4 shows that the experimental data compares well to equation (2-17) for  $Re_s < 400$ . Similar results are obtained by Derbunovich et.al (11) as shown in Figure 2-4 (b). Kröger (1) established that the loss coefficient of a wire screen can be related to the drag coefficient of a cylinder and can be expressed as follows:

$$\frac{K_{scr} \beta_{scr}^2}{1 - \beta_{scr}} = c_D \quad (2-19)$$

which is valid if  $d_{scr}/P_{scr} \ll 1$ . Figure 2-4 (b) plots this equation and it is observed that for  $100 < Re_{scr} < 1000$  that equation (2-19) deviates from experimental data, but at higher  $Re_{scr}$ , a good representation of the loss coefficient is observed from the experimental data of Cornell (12).

Figure 2-3 (b) illustrated the results for two layers attached on either side of a piece of honeycomb. The wind tunnel was unable to exceed an average velocity above 14m/s through the packing. Above this value the loss coefficient can be assumed as constant at a value of 13 as shown in Figure 2-4 (b). For use in the Fluent models, a sixth order polynomial is fit through the data which yields:

$$K_{scr} = -1.449628 \times 10^{-4}v^6 + 6.361771 \times 10^{-5}v^5 - 0.1074526v^4 + 0.8750982v^3 - 3.385495v^2 + 3.911621v + 18.78976 \quad (2-20)$$

where  $v$  is the velocity perpendicular to the wire mesh and the validity of the equation is for  $2\text{m/s} \leq v \leq 13\text{m/s}$  and an ambient temperature of  $22^\circ\text{C}$ , as plotted in Figure 2-3(b).

### **2.2.2 Cooling tower sector model**

An existing cooling tower sector model (CTSM) is used to measure the static pressure profiles behind the packing on the inside of a cooling tower. The methodology and experimental results are presented in this section.

#### **(a) Design criteria for the test rig**

The design criteria for the CTSM are:

- Air flow rate needs to be variable and measured.
- The loss coefficient of the tower has to be representative of the actual full-scale tower.
- The test section has to be dimensionally and dynamically equivalent to the actual full-scale tower.
- Pressure points are needed for determining the pressure drop in the tower.

The wind tunnel capacity and model size limit the measured  $Re$  to be one order of magnitude less than for a full-scale cooling tower. However, this does not result in an inaccurate representation of the dynamics within the tower (6).

#### **(b) Description of the test rig**

The CTSM is representative of a conical tower with a cylindrical outlet. The dimensions are based on a full-scale tower with an inlet diameter of  $d_i = 104.5$  m, an outlet diameter of  $d_o = 60$  m and a total height, starting from the top of the air inlet to the tower, of  $H_6 - H_3 = 137$  m. The conical section has an apex angle of  $14^\circ$ . The assumption is made that the air entering the tower is drawn into the tower from a region roughly two thirds the height of the tower (1). This assumption allows the omission of the top third of the tower in the CTSM model.

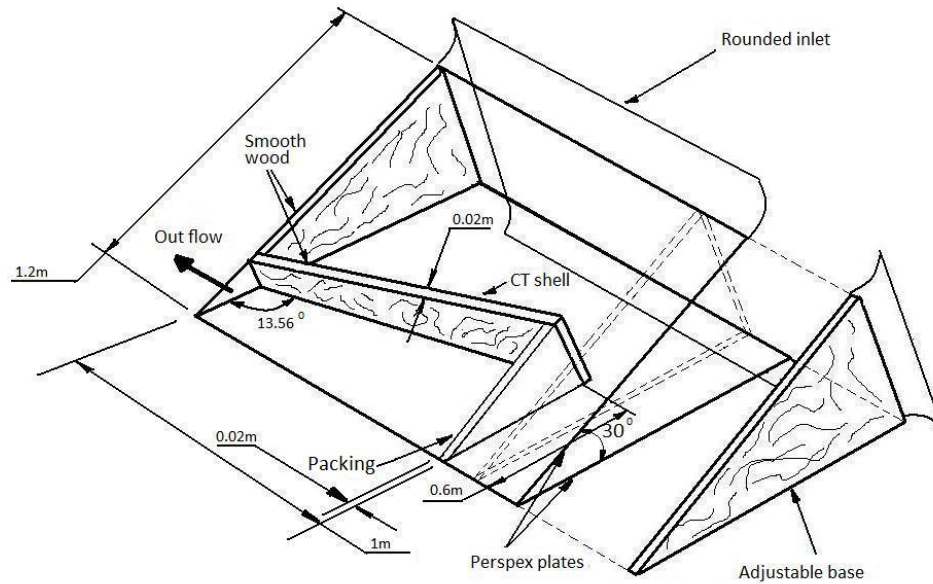


**Figure 2-5 Experimental cooling tower scale sector model**

The dimensions of the CTSM are 1.2 m x 1.2 m. The model represents a 30° sector of the cooling tower and is built to a scale of about 1:87. The inlet to the model is rounded to allow for a uniform velocity profile and to avoid separation at the edges. The base is adjustable so as to achieve different ratios of inlet diameter to inlet height and the tower wall is simulated using wood with a smooth finish. The sector is then closed off with smooth Perspex to minimize flow losses due to wall friction. The model is connected to the wind tunnel at the exit of the tower in order to induce air flow through it.

The cooling tower fill loss is simulated using a wire screen, which is supported by a honeycomb as discussed in section 2.2.1. The presence of the wire mesh at the front might result in deviation of the flow characteristics from that of normal tower packing since flow separation might not take place on the inlet edges of the packing as is the case with heat exchangers and film packing (1). This changes the loss characteristics from orthotropic to anisotropic. Since the wire screen lacks rigidity, the screen is packed in layers to prevent deformity, which results in a loss coefficient for the heat exchanging unit that varies with velocity. The sector model packing loss coefficient is verified by measuring it in the sector model. To establish flow perpendicular to the mesh, a wall is added at the inlet to the tower and the base is removed. The results of this experiment are compared to the results of the previous section later on.

The inlet rounding and protruding platforms that are attached to the CTSM, as illustrated in Figure 2-20, are made from 1mm thick sheet metal, which unfortunately bends towards the base during the experiment, increasing the pressure drop through the system. A better material could not be found that would satisfy dimensional equivalence and if stiffeners are attached to these structures the flow patterns into the tower would be affected. The structures that were added to the CTSM include walkways at the entrance to the tower with length to diameter dimensions of 0.0172, 0.0344 and 0.0689 respectively. One rounded inlet was also tested with  $r_i/d_i = 0.02$ . The experimental measurements are documented in Appendix D.

### (c) Measurement technique used for the test rig

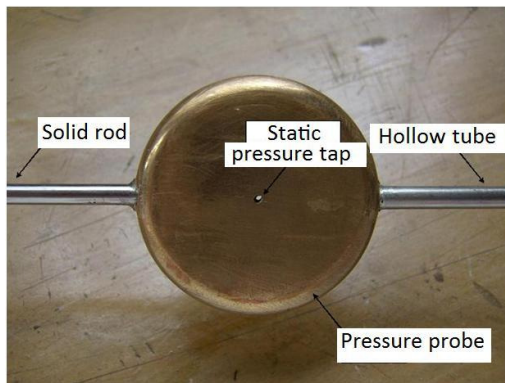


**Figure 2-6 Static pressure probe used in CTSSM**

Figure 2-6 shows the static pressure probe that is used in the CTSM. The static pressure is measured 45mm above the base of the tower shell on the inside of the tower and is accomplished with a static pressure probe that is calibrated in a wind tunnel using a pitot tube. The design of the probe, calibration method and results are given in Appendix B. The effect of the angle of attack of the static pressure probe to the flow direction is also tested by a sensitivity analysis and it is observed that the measurements do not change significantly up to an angle of  $5^\circ$ . The mass flow rate through the tower is determined by using the method as described in Appendix B.

### (d) Test procedure for the test rig

To ensure that the data is comparable, one parameter needs to be held constant and this is taken to be the mass flow rate. A constant mass flow rate ensures a constant loss coefficient for the packing, which is necessary since the loss coefficient is relative to the velocity of the air flowing through the packing.

Before each experiment, the adjustable base is positioned at the required inlet height. The static pressure probe is inserted, the wind tunnel is started and the speed of the fan adjusted until the required mass flow rate is achieved. The flow field is allowed to stabilize before readings are taken. The flow is assumed stable when the static pressure at the model outlet is constant over time. The probe is then moved from its starting point at the cooling tower centre towards the wall in increments that decrease in size. The increments are very small close to the air inlet wall to enable close monitoring of the static pressure distribution, so as to accurately locate the start of the recirculation zone. When the sweep is finished, the wind tunnel is switched off. Before the base is moved to the next location, a verification of the static pressures is done by repeating the tests.

### (e) Measurement of fill loss coefficient

The loss coefficient of the packing material is measured in the CTSM to determine this configurations influence on the loss coefficient. The packing loss coefficient is determined for a velocity range of 3 m/s to 12 m/s due to wind tunnel limitation on the differential pressure it is able to overcome.

Figure 2-7 displays the results for the fill loss coefficient determined with the sector model and it is observed that the results obtained are between 20 % and 25 % larger than those measured in the pipe test section. It is discovered that the sheets of wire screen used for the CTSM and that measured in the pipe section do not have the same wire diameter. The wire screen used in the CTSM has a  $d_s = 0.187\text{mm}$  and a  $P_s = 0.41\text{mm}$ . A curve-fit of the data yields the following power function:

$$K_{he} = av^b \quad (2-21)$$

where  $v$  is the average velocity through the wire screen and the coefficients  $a$  and  $b$  are given in Table 2-1.

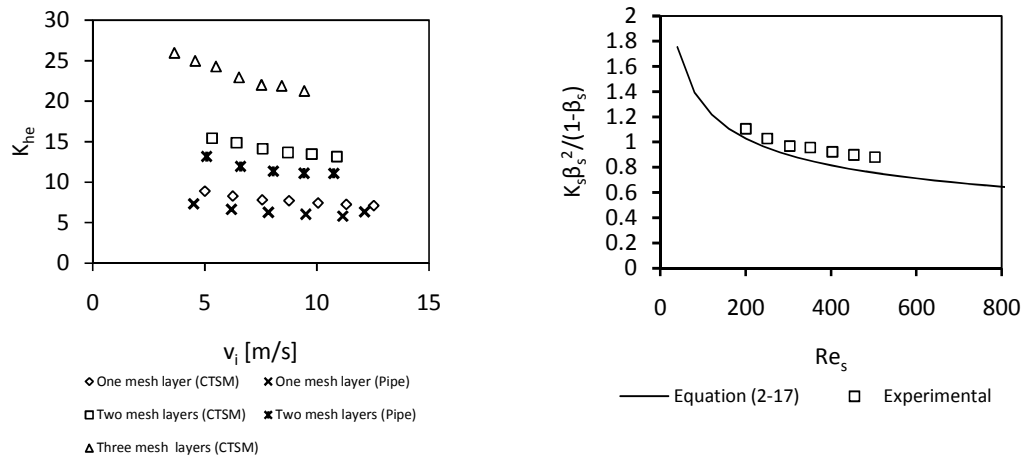


**Figure 2-7  $K_{he}$  determined in the CTSM**

**Table 2-1 Power function coefficients for equation (2-21)**

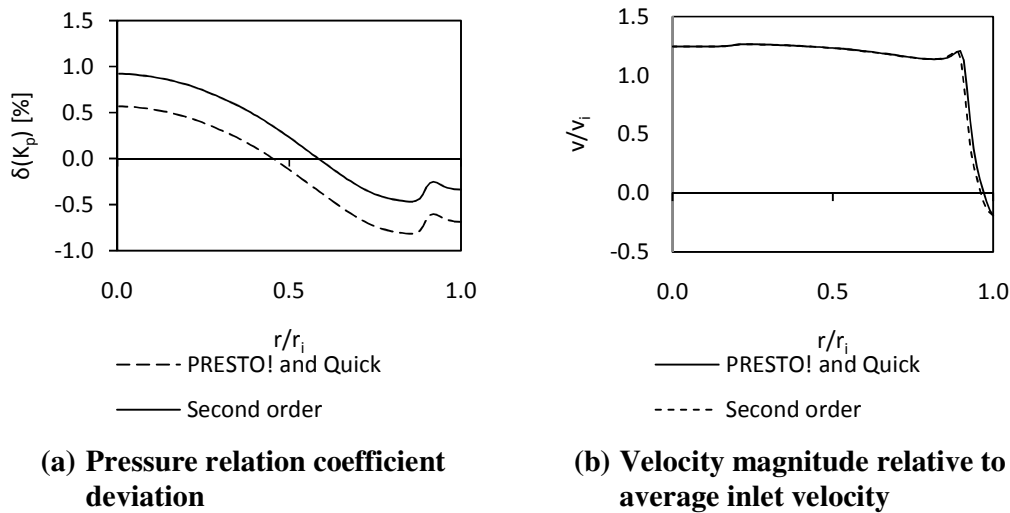
Number of Layers	a	b
1	12.92773	-0.23992
2	22.59034	-0.22795
3	34.73116	-0.2189

With the loss coefficient of the packing known, different configurations of tower inlet height, with or without inlet rounding or protruding platforms attached, are investigated during the course of the experiment. As reference, the tower inlet loss is determined for a sharp inlet and two layers of mesh. The results are presented in Section 2.5.

## 2.3 CFD modelling procedure

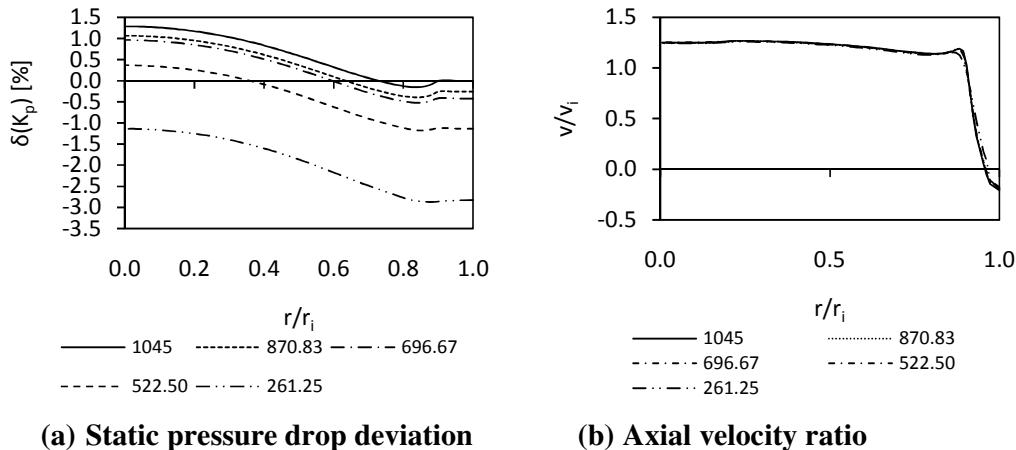
The CTSM is simulated with Fluent using a double precision, axis-symmetric solver. The SIMPLE algorithm is utilized with the aid of the PRESTO! discretisation scheme for pressure calculation and the QUICK discretisation scheme for momentum and turbulence calculation. It is found that the combination of these two schemes provide

the same results as the second-order upwind scheme, however, with a faster convergence rate. Figure 2-8 displays the deviation percentage of PRESTO! and QUICK discretisation scheme compared to the second order scheme showing that the difference is negligible. The heat exchanger of the tower is modelled using a porous medium with anisotropic characteristics represented by a horizontal loss coefficient set  $10^6$  higher than the vertical loss coefficient in order to act as a guide vane. The reference values for this section are  $d_i/H_i = 10.45$ ,  $K_{he} = 22.59v_i^{-0.22795}$  and  $m_a = 11.5$  kg/s.



**Figure 2-8 Comparison of the second order scheme to the combination of the PRESTO! and QUICK schemes with  $d_i/c = 1045$  and  $K_{p(ref)} = 21.91$**

To validate the Fluent model, the effects of grid size, grid type, turbulence model, turbulence parameters and processing time on the results are investigated and the results are compared to experimental data and data from literature.



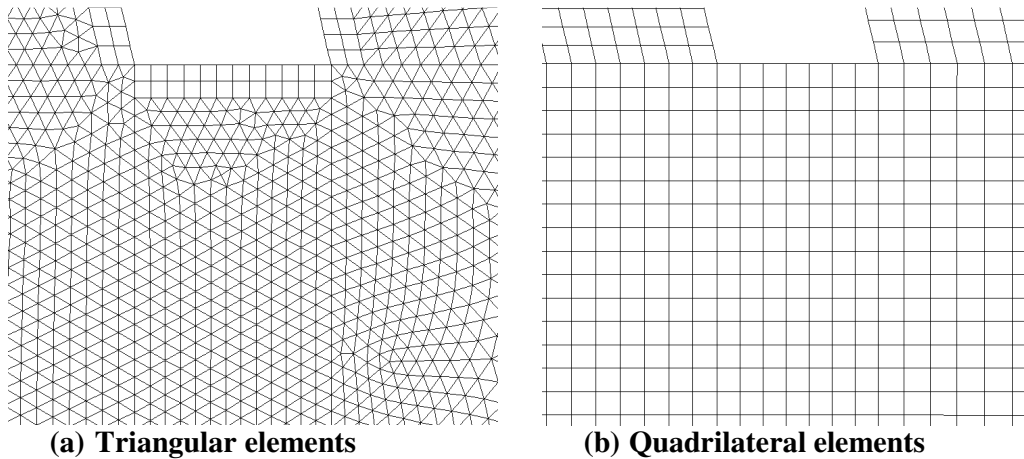
**Figure 2-9 Effect of grid size on the pressure relation coefficient and velocity profile above the packing for  $K_{p(ref)} = 29.91$**

Figure 2-9 and Table 2-2 shows the results of the grid independence analysis based on tetrahedral elements with an internal diameter to starting cell size ratio of  $d_i/c = 696.67$ , as the reference. It can be seen that the differences in  $K_p$  and  $v/v_i$  for different

grid sizes are relatively small. To minimize the number of cells required, grid independence is therefore said to be achieved at  $d_i/c = 696.67$ .

**Table 2-2 Number of cells for different starting cell sizes**

$d_i/c$	number of cells [n]	$\delta(n)$ [%]
1045	273420	189.3
870.83	148159	56.8
696.67	94512	0
522.5	78892	-16.5

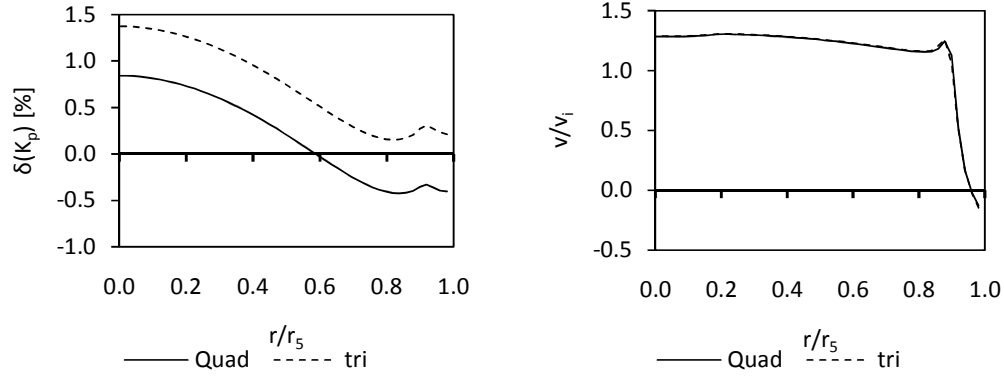


**Figure 2-10 The different grid structures investigated for the analysis of tower inlet losses**

Figure 2-10 shows the grids investigated. The cells start fine at the bottom edge of the shell and gradually become coarser, to reduce the number of cells in the grid. A finer mesh is required in areas where there are velocity gradients. Triangular elements are used to establish grid independence due to the ease with which a grid can be constructed. Further it is known that an un-structured grid is more favourable when the flow is not aligned to the boundaries of the cells. The  $d_i/c$  ratio next to the shell wall at the inlet of the tower is 696.67 and the growth factor is 1.005 towards the inside of the tower and 1.02 towards the outside.

Figure 2-11 and Table 2-3 give a comparison of the results obtained for quadrilateral and triangular meshes. Table 2-3 indicates that the differences in the numerical results between the two meshes are negligible and the increase in the computational time due to the number of cells can also be ignored. Figure 2-11 (a) shows that there is not a significant difference in the results of the meshes under investigation with an average deviation of 0.63 %. It is important to note that the maximum growth rate of cells should not exceed 20 %, since a higher growth rate results in increased convergence time and inaccurate results.





(a) Pressure relation coefficient deviation with  $K_{p(\text{ref})} = 23.71$

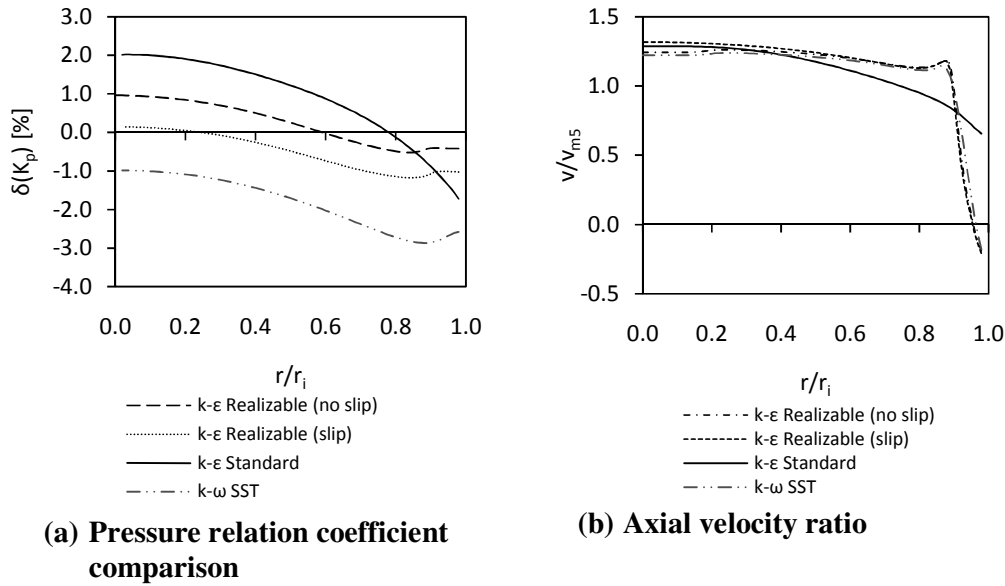
(b) Axial velocity ratio

Figure 2-11 Effect of grid type on the pressure relation coefficient and velocity profile for  $K_p = 23.71$

Table 2-3 Comparison of the results for triangular and quadrilateral meshes with  $d_i/c = 696.67$

	triangular	quadrilateral	$\delta(x)$ [%]
Number of cells	94512	80165	-15.18
$d_{ie}/(d_i+2t_s)$	0.8966	0.8979	0.144
$v_{m,vc}/v_{m5}$	1.17	1.17	0
$\alpha_{e,vc}$	1.04	1.04	0
$K_p$	23.84	23.71	-0.55
$K_{ct}$ Equation (2-8)	10.79	10.66	-1.2
$K_{ct}$ Equation (2-3)	10.35	10.23	-1.16

The processing time is usually determined mainly by the turbulence model and the size of the grid, however in this case the grid remains the same size and thus is only dependent on the turbulence model. The comparison between turbulence models are done for the standard, realizable and RNG  $k-\epsilon$  models as well as the  $k-\omega$  SST model. The RNG and realizable models predict the same solution for the test case however the realizable models processing time is in the order of 30 % faster. The main difference between the two models is that the realizable model statistically dampens the turbulent viscosity ratio by limiting it in regions where turbulence is high (13).



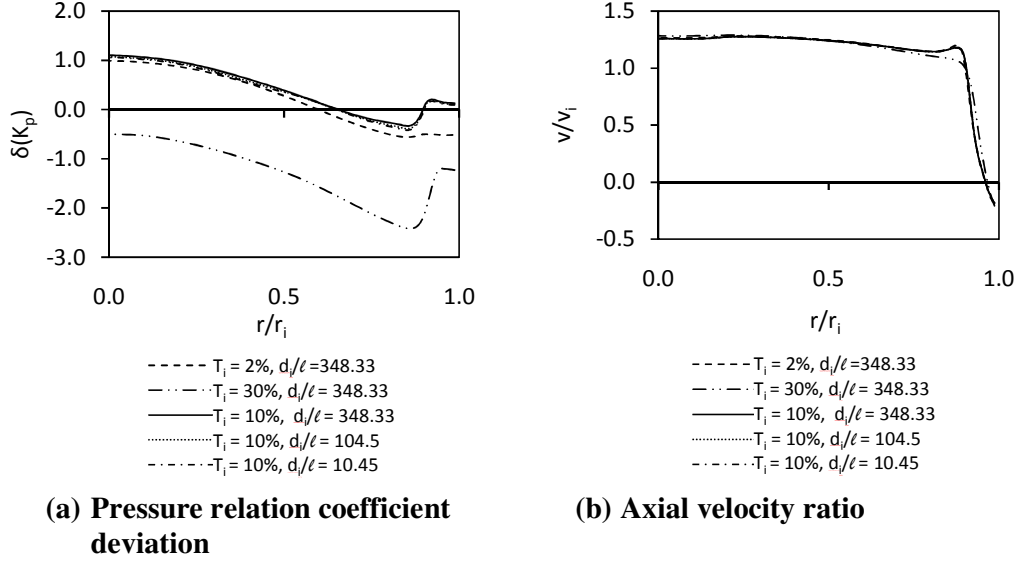
**Figure 2-12 Effect of different turbulence models on the pressure relation coefficient and velocity profile for  $K_{p(\text{ref})} = 21.91$**

**Table 2-4 Comparison of the results for different turbulence models**

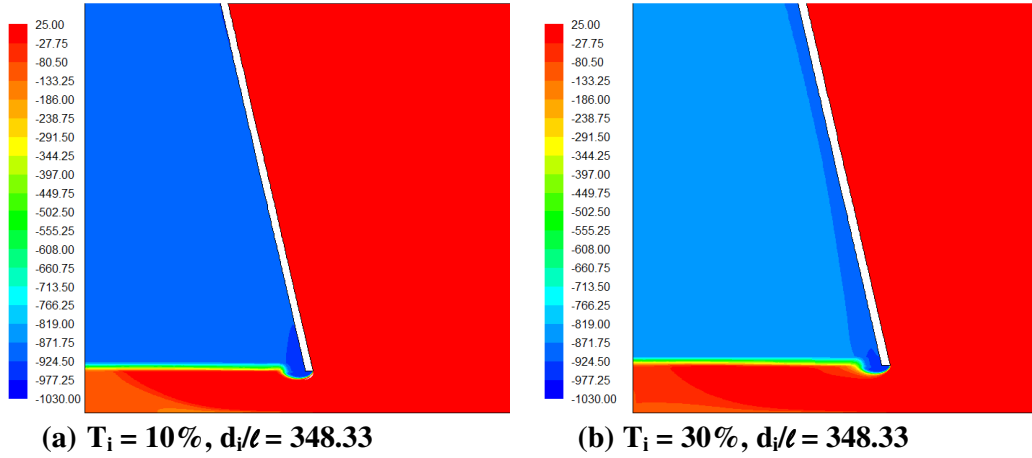
	k- $\epsilon$ Realizable			k- $\epsilon$ Standard		k- $\omega$ SST	
	No-slip	Slip	$\delta(x)$ [%]		$\delta(x)$ [%]		$\delta(x)$ [%]
$K_p$	22.354	22.191	-0.727	22.440	0.385	21.875	-2.140
$d_{ie}/(d_i+2t_s)$	0.891	0.886	-0.546	0.949	6.578	0.903	1.419
$v_{m,vc}/v_{m5}$	1.161	1.174	1.101	1.022	-11.962	1.129	-2.746
$\alpha_{e,vc}$	1.039	1.039	0	1.086	4.526	1.05	1.068
$K_{ct}$ Equation (2-8)	9.680	9.518	-1.678	9.766	0.889	9.202	-4.941
$K_{ct,T}$ Equation (2-3)	9.269	9.075	-2.092	9.614	3.724	8.854	-4.473

Figure 2-12 and Table 2-4 illustrates the results of the turbulence model evaluation. The resulting deviation is relative to the k- $\epsilon$  realizable model with no slip at the walls. The standard k- $\epsilon$  model does not predict the velocity or the static pressure profile correctly; the reason being that the model predicts no recirculation zone and thus a 100% effective diameter. The k- $\omega$  SST model predicts approximately the same velocity profile as that of the realizable k- $\epsilon$  model, but under predicts the static pressure drop. Thus the k- $\epsilon$  realizable model is deemed the more accurate of the three models when comparing the results with experimental values later on in this chapter.

Table 2-4 shows that the effect of including the boundary layer in the Fluent model is small when compared to the corresponding solution for slip walls. This is because the boundary layer is thin and thus does not influence the flow significantly. From Figure 2-12 it is noted, however, that there is a difference in pressure and velocity profiles. The condition of slip at the wall leads to a larger predicted recirculation zone and this can be observed from Table 2-4, where the effective inlet diameter is lower for slip conditions than for the no-slip conditions. To reduce the number of cells it is however considered acceptable to assume slip walls.



**Figure 2-13 Effect of turbulence intensity and length scale on the pressure relation coefficient and velocity profile with  $K_{p(\text{ref})} = 22.21$**



**Figure 2-14 Effect of turbulence intensity on the total pressure**

Figure 2-13 shows the effect of turbulence intensity ( $T_i$ ) on the reference case results. The turbulence intensity is defined as the ratio of the velocity fluctuation to the average velocity, with both values being root-mean squared. It is a physical quantity that is related to the size of the large eddies that contain the energy in turbulent flow (13). Figure 2-13 (a) illustrate that the turbulence intensity has the dominant effect on the results, but even so the change in the end result is less than 2%. The difference in the velocity profiles noted in Figure 2-13 (b) can be explained by the smaller recirculation zone shown in Figure 2-14. Thus, an increasing in the turbulence intensity seems to decrease the recirculation zone at the inlet to the tower, which results in an increase in the effective diameter.

From the above analysis it is recommended that when simulating the tower inlet the realizable k- $\epsilon$  model with slip walls and a triangular mesh with  $d_i/c = 696.67$  at the inlet, be used. A turbulence intensity of 10 % is regarded as a high value (13) and thus a value of 2 % is chosen to represent the flow into the tower, since the air inside

the laboratory is still and the experimental apparatus has rounded inlets. Considering that the turbulent length scale does not have a significant effect on the results, a value of 0.3 m is chosen, since it is the largest size an eddy can reach in the CTSM due to this being the size of the largest opening.

## 2.4 Tower modelling results

The following section presents a comparison of the CFD results with the experimental results and data from literature, after which full-scale simulations are done for different inlet geometries. Unless stated otherwise, all the models simulated in this section are given the following input variables:

- $Re = 648072.7$ , which is based on conditions at the horizontal cross-sectional area at the inlet of the tower.
- $K_{he}$ , in the direction perpendicular to the flow, is modelled using equation (2-20) for the added structure investigation, equation (2-21) during the comparison with experimental results and constant for comparison with data from literature.
- A momentum source term,  $K = 10^6$ , is added to the porous medium zone to represent the fill/heat exchanger in order to direct the flow in the axial direction, as described in section 2.3.
- Reference pressure,  $p_{ref} = 100\,000$  Pa
- Turbulence intensity,  $T_i = 2\%$
- Turbulent Length scale,  $\ell = 0.3$  m

**Table 2-5  $K_{ct}$  results at different values of  $Re$  obtained using Fluent**

Re	$K_{ct}$
517541.8	4.00
972331.7	3.999
1293855	3.996
1617318	3.995

The above value for  $Re$  is approximately the same as that measured in the wind tunnel and it does not have a significant influence on  $K_{ct}$  (3). This is verified by the Fluent results shown in Table 2-5. The experimental results cannot be compared to data from literature since the equivalent tower wall thickness to diameter ratio of the CTSM is  $t_s/d_i = 0.0168$ , where as those of literature models are  $t_s/d_i = 0.00957$  [ (1), (3), (4), (6)]. The increased thickness of the wall will affect the inlet loss of the tower and thus must be compared separately.

### 2.4.1 Comparison of experimental and Fluent results for a sharp inlet

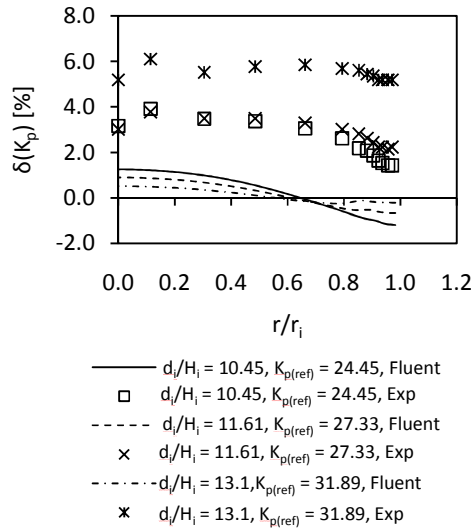


**Figure 2-15 Static pressure drop deviation between Fluent and experimental data**

**Table 2-6 Tower inlet loss coefficients for sharp inlet with  $K_{he} = 14.3$  for different ratios of  $d_i/H_i$**

$d_i/H_i$	Experimental (Equation (2-8))	Fluent (Equation (2-8))	Fluent (Equation (2-3))
<b>10.45</b>	9.787	9.641	8.926
<b>11.61</b>	12.924	12.595	11.764
<b>13.06</b>	18.450	17.266	16.257

Figure 2-15 compares the static pressure determined with the aid of Fluent to experimental results for different inlet ratios. This shows that Fluent underestimates the pressure loss through the system by less than 4 % for  $d_i/H_i$  values of 10.45 and 11.61 and less than 6 % for  $d_i/H_i = 13.1$ . There are many factors that influence the difference in the results of the Fluent models to the experimental results, such as the turbulence model used, assumptions made to simplify the model, the uncertainty of accuracy during the experiment and the porous media model employed. In the Fluent models oblique air flow is directed in the axial direction by including a large fill loss coefficient in the radial direction. This causes all the radial momentum to be lost through dissipation. Since honeycomb is used in the CTSM, it could be that the fill has an orthotropic resistance component due to flow separation and subsequent momentum recovery. This would result in a lower fill loss coefficient and thus a higher inlet loss coefficient.

Table 2-6 represents a comparison of the inlet loss coefficient determined experimentally and the Fluent results. The error is proportional to the increase in the velocity through the vertical inlet of the tower and further refinement of the grid in this area can lead to better results. The difference in loss coefficient between equation (2-8) and equation (2-3) are also presented and it is noted that the loss coefficient decreases substantially when the vena contracta is considered. This is a result of the

difference between the kinetic energy, in terms of the definition of the average velocity according to equation (2-5) and (2-6). Equation (2-6) results in a higher average velocity which in turn results in a lower predicted total pressure loss through the system.

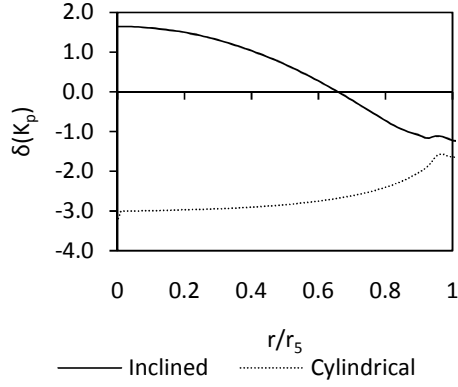
## 2.4.2 Comparison of CFD to correlations from literature

A Fluent model of the experimental setup of Geldenhuys (6) is developed, based on the experience gained in the preceding sections. The first step therefore is to study the effect of shell wall inclination on the inlet loss coefficient and effective diameter.

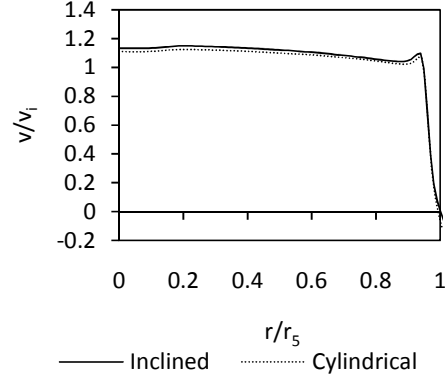
**Table 2-7 Fluent loss coefficient and effective diameter data for cylindrical and conical tower walls**

$K_{he}$	11		12.2		6.53	
$d_i/H_i$	7.5		10		12.5	
Re	1800000		2000000		2000000	
	Inclined	Cylinder	Inclined	Cylinder	Inclined	Cylinder
$v_{m,vc}/v_{m5}$	1.037	1.054	1.194	1.022	1.502	1.482
$d_{ie}/(d_i+2t_s)$	0.955	0.957	0.942	0.973	0.793	0.806
Equation (2-11)		0.948		0.930		0.863
$\delta(d_{ie}/(d_i+2t_s))$	0.221%	0.953%	3.263%	4.644%	1.708%	-6.614%
$\alpha_{e,vc}$	1.051	1.021	1.111	1.214	1.030	1.021
$K_p$	16.3	15.9	21.4	20.7	26.8	25.2
$K_{ct}$ (Equation (2-8))	4.32	3.91	8.19	7.54	19.28	17.71
Equation (2-9)		3.88		7.29		15.65
$\delta(K_{ct})$	-9.55%	0.73%	-7.91%	3.44%	-8.15%	13.13%
$K_{ct}$ (Equation (2-3))	4.15	3.77	7.87	7.27	17.87	16.47
Equation (2-10)		Not Applicable		7.94		14.85
$\delta(K_{ct})$	-9.03%		-7.60%	-8.39%	-7.83%	10.89%

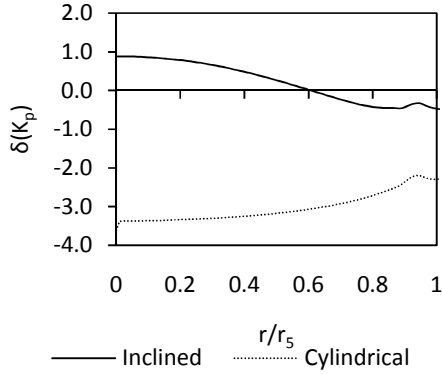
Table 2-7 shows the Fluent data determined for conical and cylindrical shell walls for different fill loss coefficients ( $K_{he}$ ) and inlet diameter to height ratios. The corresponding pressure relation coefficients and velocity profiles are presented in Figure 2-15. In this table the cylindrical models results are compared to the equations from literature and to the conical models results. From this table it is clear that in all the cases studied the mean vena contracta velocity decreases and the effective diameter increases for the cylindrical wall relative to the inclined wall. This can be attributed to the decrease in diameter of the conical wall which accelerates the flow and increases the shear stresses present in the air streams. Equations (2-9), (2-10) and (2-11) correlate well with the data obtained from the Fluent models for the cylindrical case except for the combination of the lowest value of  $K_{he}$  and the highest ratio of  $d_i/H_i$ .



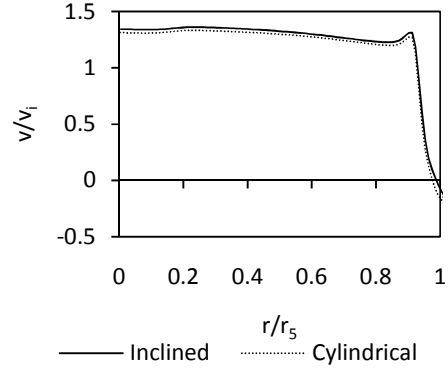
(a)  $K_p$  deviation for  $K_{he} = 11$ ,  $d_i/H_i = 7.5$ ,  $K_{p(ref)} = 17.25$



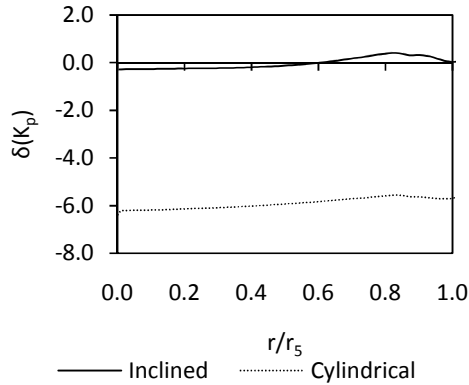
(b) Axial velocity ratio for  $K_{he} = 11$ ,  $d_i/H_i = 7.5$



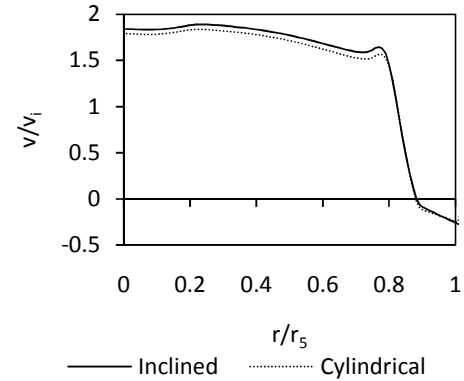
(c)  $K_p$  deviation for  $K_{he} = 12$ ,  $d_i/H_i = 10$ ,  $K_{p(ref)} = 27.85$



(d) Axial velocity ratio for  $K_{he} = 12$ ,  $d_i/H_i = 10$



(e)  $K_p$  deviation for  $K_{he} = 6.53$ ,  $d_i/H_i = 12.5$ ,  $K_{p(ref)} = 34.51$



(f) Axial velocity ratio for  $K_{he} = 6.53$ ,  $d_i/H_i = 12.5$

Figure 2-16 Fluent curve comparison of  $\delta(K_p)$  and  $v/v_i$  for cylindrical and conical tower walls

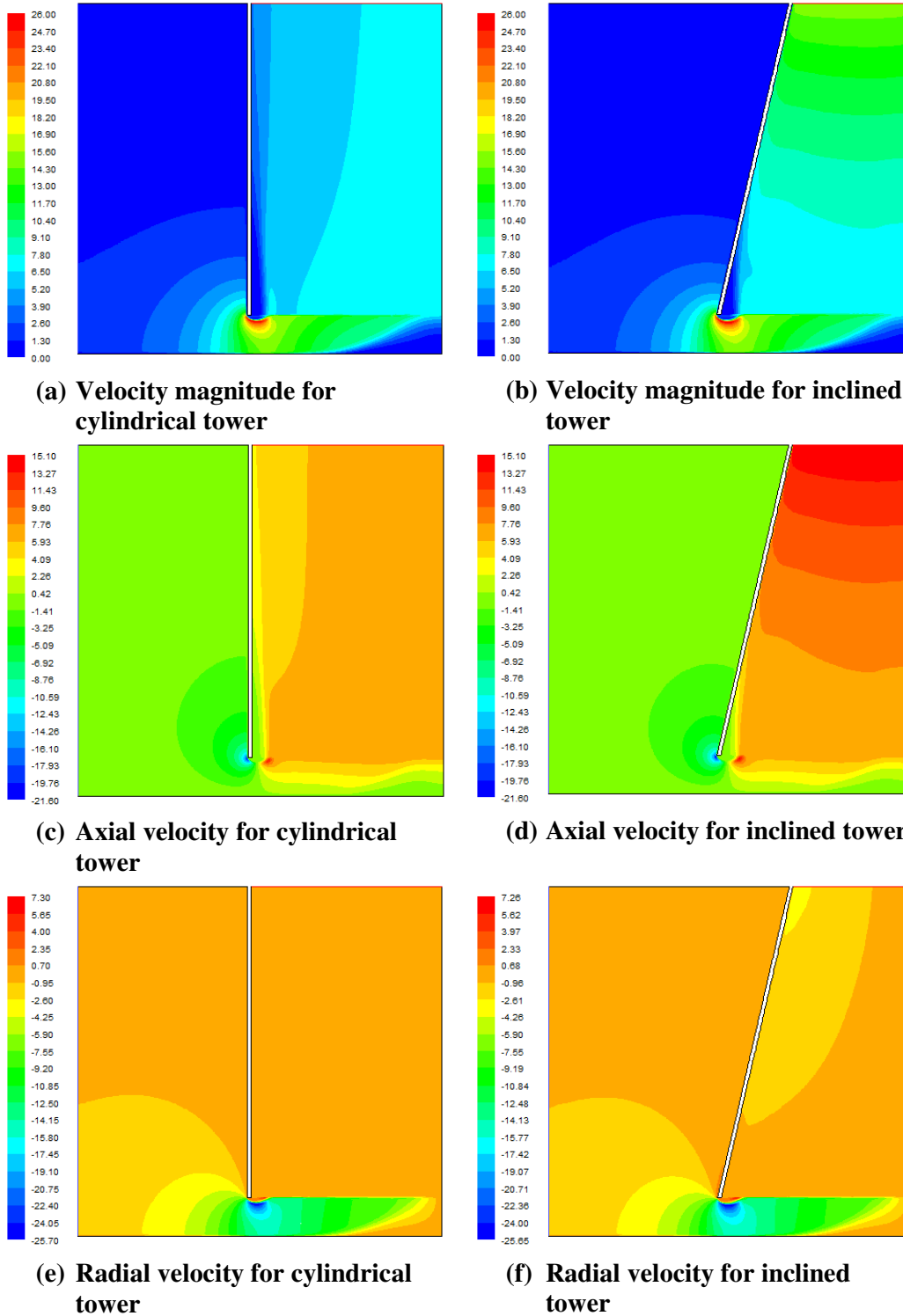


**Figure 2-17 Contour plots for cylindrical and inclined tower walls**

Figure 2-16 provides a comparison between inclined and cylindrical tower walls, showing the pressure relation coefficient deviation and axial velocity ratio curves for different  $K_{he}$  and  $d_i/H_i$  values. The axial velocity profiles are similar, but the static pressure profiles are different for the two configurations in all three cases



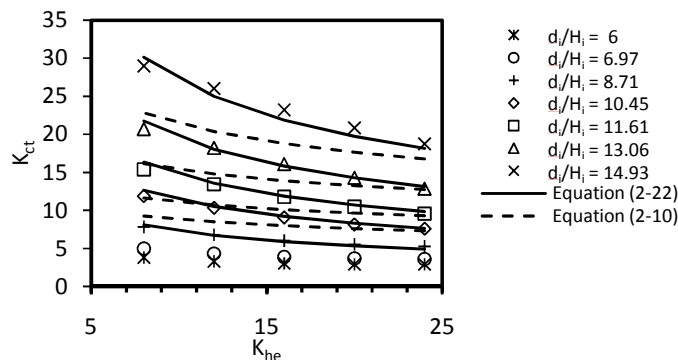
investigated. The pressure relation coefficient profiles tend to become increasingly similar with an increase in  $K_{ct}$  while the magnitude of the coefficients deviate further.

Figure 2-17 gives contour plots for velocity magnitude, axial velocity and radial velocity. The increased pressure difference for the inclined wall is explained by the axial and radial acceleration of the air inside the tower due to decreasing diameter, which increases shear stresses in the air and thus increases the energy needed to overcome these stresses. From Table 2-7 it can be seen that the loss coefficient for an inclined shell wall is significantly higher than for the cylindrical tower shell. The cylindrical Fluent model is first validated using equation (2-9) to determine what the effect of an increased  $d_i/H_i$  has on the simulation results.

**Table 2-8 Fluent model with an inclined shell compared to equation (2-9), which is based on a cylindrical shell, with  $K_{he} = 12$**

$d_i/H_i$	Geldenhuis (3)	Fluent	$\delta(K_{ct})[\%]$
8.708	8.75	7.08	23.59
10.45	10.10	10.79	-6.395
11.61	13.75	14.02	-1.926
13.06	17.50	19.04	-8.09

Table 2-8 compares the conical tower wall loss coefficients determined with Fluent, using equation (2-8), to equation (2-9) for different values of  $d_i/H_i$ . From Figure 2-16, Figure 2-17 and Table 2-8 it can be seen that there is a significant difference between the loss coefficients of an inclined tower wall to that of a cylindrical wall. To investigate the effect of an inclined shell wall on the loss coefficient of a full-scale tower, a Fluent model of a NDCT is constructed that will satisfy the required internal  $Re = 10^7$ . The results of these simulations are used to determine new empirical equations for the inlet loss coefficient and effective diameter of an inclined shell with an anisotropic fill.



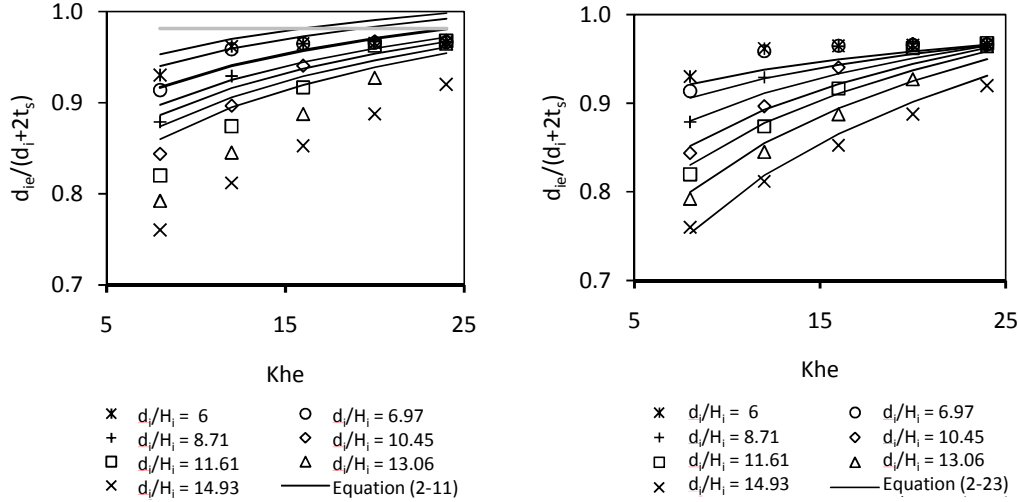
**Figure 2-18 Inlet loss coefficients determined with Fluent for a sharp inlet**

Figure 2-18 illustrates the inlet loss coefficients for different diameter to height inlet ratios and fill loss coefficients calculated using equation (2-3). It can be seen that equation (2-10) does not correlate well with the data. The following relation is proposed for the inlet loss coefficient:

$$K_{ct} = 0.11 \left( \frac{d_i}{H_i} \right)^{2.439} K_{he}^{-0.4597} \quad (2-22)$$

for  $8.71 \leq d_i/H_i \leq 15$  and  $8 \leq K_{he} \leq 24$ .

This equation has a maximum deviation from the numerical data of 7% at the extremes of the boundary values.



(a) Comparison of data with equation (2-11) (b) Comparison of data with equation (2-23)

**Figure 2-19 Effective diameter ratio determined with Fluent for a sharp inlet**

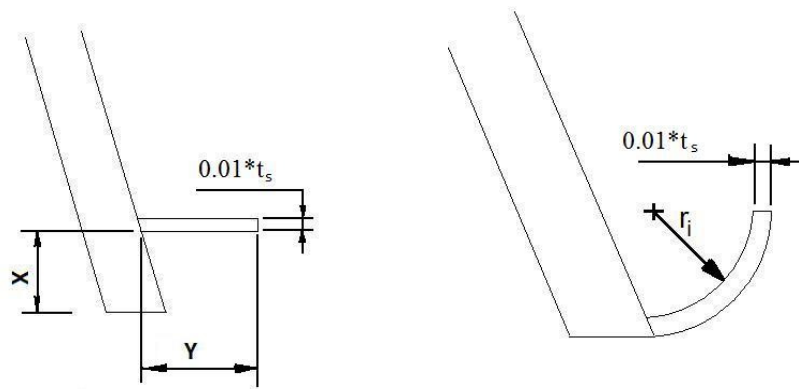
Figure 2-19 (a) illustrates the effective diameter data obtained from Fluent for different  $d_i/H_i$  and  $K_{he}$ , and shows significant deviations compared to equation (2-11). The effective ratio cannot be higher than 0.9812, as indicated by the thick grey line, due to the dimensions of the current model. Equation (2-23) provides an improved curve fit to the data as shown in Figure 2-19 (b) and the equation is presented as:

$$\frac{d_{ie}}{d_i + 2t_s} = 1.2 + \left[ -0.000384 \left( \frac{d_i + 2t_s}{H_i} \right)^2 - 0.001349 \left( \frac{d_i + 2t_s}{H_i} \right) - 0.178269 \right] \times \ln \left( \frac{d_i + 2t_s}{H_i} \right) + \left[ 0.013293 \left( \frac{d_i + 2t_s}{H_i} \right) - 0.040396 \right] \ln K_{he} \quad (2-23)$$

for  $6 \leq d_i/H_i \leq 11.61$  and  $8 \leq K_{he} \leq 25$ . This equation has a maximum deviation of 3.2% for the range specified.

### 2.4.3 Comparison between experimental and Fluent results for different inlet geometries

From the study of the inlet loss and effective diameter of the sharp inlet, it is observed that there is a considerable flow re-circulation at the inlet due to flow separation, which will reduce heat transfer in this region (1). To reduce this re-circulation region, the effect of a protruding platform and rounded inlets on the inlet loss coefficient and effective diameter, as depicted in Figure 2-20, is investigated experimentally and simulated with the aid of Fluent.



(a) Protruding platform

(b) Rounded inlet

**Figure 2-20 Different inlet geometries to improve the inlet loss coefficient and effective inlet diameter**

Figure 2-20 illustrates the different tower inlet geometries investigated experimentally and with Fluent, to determine whether the effective diameter can be increased and the loss coefficient decreased compared to a normal sharp inlet. The protruding platform is varied in length as well as in distance above the inlet. The description of these walkways is given in the form of  $X \times Y$ , as shown in Figure 2-20. The dimensions are based on a tower with  $d_i = 104.5$  m and are scaled accordingly for the CTSM.

**Table 2-9 Tower inlet loss coefficients for protruding platforms and rounded inlets with  $K_{he} = 14.3$**

	Experimental	Fluent
Square inlet	9.79	9.65
0x1.8	9.19	7.73
0x3.6	8.55	6.63
0x5.4	8.34	5.55
$r_i/d_i=0.025$	5.35	5.31

Table 2-9 presents the loss coefficients for three types of protruding platforms and a rounded inlet determined for experimental and Fluent data using equation (2-8). The inlet ratio  $d_i/H_i = 10.45$  is kept constant for these experiments and the platforms have the following dimensions: 0 m x 1.8 m, 0 m x 3.6 m and 0 x 5.4 m. It is observed that the experimental loss coefficients are significantly higher than the values obtained with Fluent, for the platforms. As noted in section 2.2.2, the description of the experimental apparatus, the platforms were bent by the airflow during the experiment, effectively increasing the inlet diameter to height ratio. This would result in higher inlet loss coefficients.

The loss coefficient of the tower is however improved by adding these platforms as both the Fluent models and the experimental results indicate. According to the experimental results the change in loss coefficient is small for a platform larger than 3.6 m. Adding a rounded inlet to the tower seems to be the most favourable approach. The inlet radius reduces the inlet loss by 45 % of the normal sharp inlet.

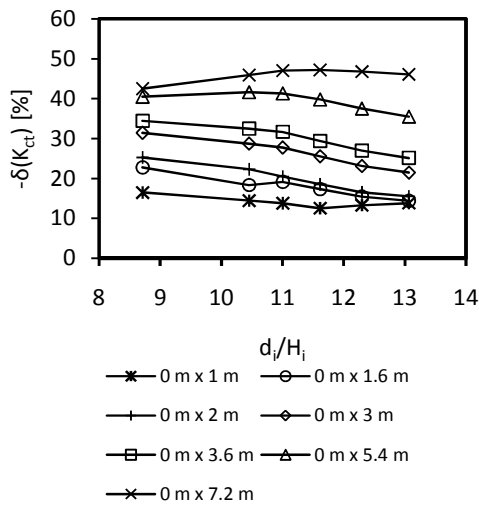
#### 2.4.4 Fluent analysis for different cooling tower inlet geometries

For the first part of this section, the dimensions and input variables of the Fluent models are identical to those of the experimental sector model, to complete the comparative study of different air inlets. Ultimately a full-scale model is developed to investigate the scale effect.

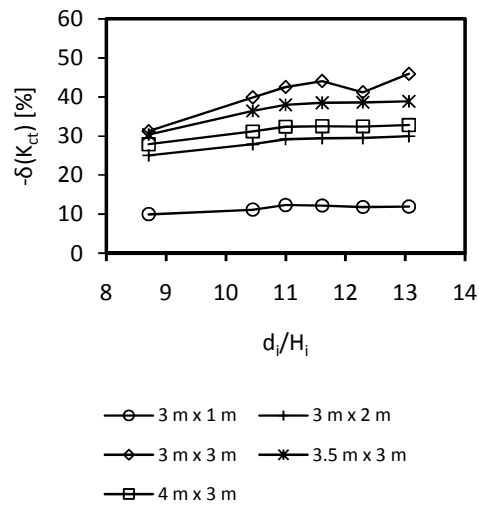
**Table 2-10 Sharp inlet loss coefficient for  $K_{he} = 11.32$  and different  $d_i/H_i$  ratios determined using Fluent**

$d_i/H_i$	Fluent (Equation (2-8))	Fluent (Equation (2-3))
8.71	6.38	6.13
10.45	10.01	9.59
11	11.57	11.07
11.61	13.29	12.72
12.29	15.4	14.74
13.06	18.15	17.43

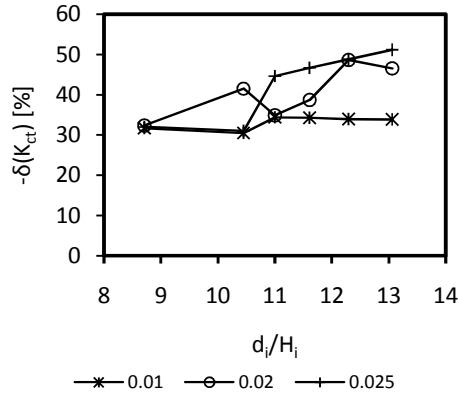
Table 2-10 represents the results of the inlet loss coefficient for a sharp inlet with different ratios of  $d_i/H_i$ . The results of both equation (2-8) and equation (2-3) are given in the table in order to provide an indication of the difference in the loss coefficient obtained when using these equations. The comparative study is conducted using the definition of the inlet loss coefficient according to equation (2-3) in order to incorporate the effect of a non-uniform velocity profile.



**(a) Protruding platforms, 0 x Y**



**(b) Protruding platforms, X x Y**



(c) Rounded Inlets,  $r_i/d_i$

**Figure 2-21 Change in  $K_{ct}$  for different cooling tower inlet geometries compared to a sharp inlet**

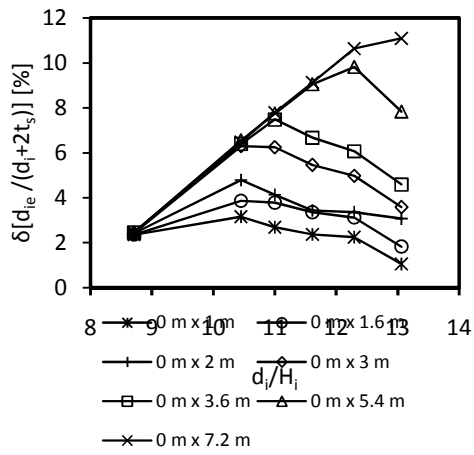
Figure 2-21 illustrates the predicted decrease in the inlet loss coefficient relative to the sharp inlet obtained for different inlet geometries. The most promising option for all inlet heights, in terms of decreasing  $K_{ct}$ , is adding a 0 m x 7.2 m walkway. However, this is not a practical solution since a large area will be utilized by the walkway and comparative results can be obtained by using the 3 m x 3 m walkway or the rounded inlet with  $r_i/d_i = 0.025$ .

Table 2-11 presents the effective diameter for a tower wall with a sharp inlet, determined with the aid of Fluent. The main focus of this study is on the effective diameter, which is to increase the effective area of heat transfer and to place more weight on the change in effective diameter than on the reduction in loss coefficient.

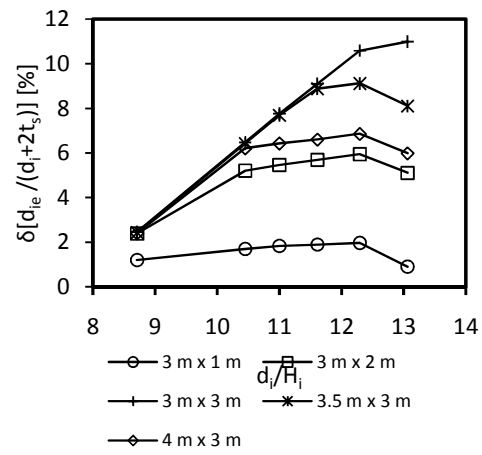
**Table 2-11 Effective diameter ratio for the sharp inlet**

$d_i/H_i$	Fluent
<b>8.708</b>	0.9263
<b>10.45</b>	0.8912
<b>11</b>	0.8803
<b>11.61</b>	0.8695
<b>12.29</b>	0.8576
<b>13.06</b>	0.854

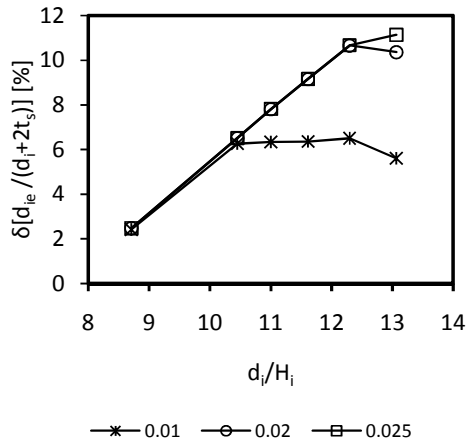
Figure 2-22 illustrates the predicted increase in effective inlet diameter ratio relative to the sharp inlet for different inlet geometries. All of the added structures succeeded in increasing the effective inlet diameter to some degree and similar trends are observed for the 3 m x 3m, 0 m x 7.2 m and the rounded inlets.



(a) Protruding platforms, 0xY

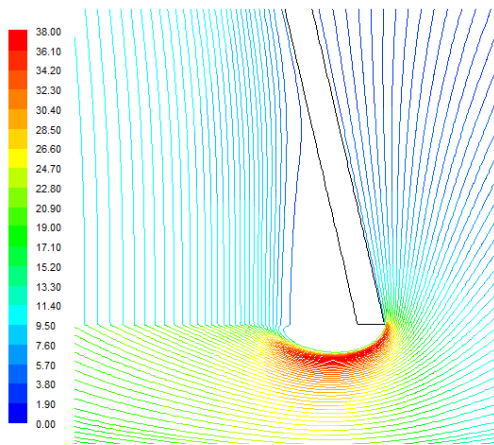


(b) Protruding platforms, XxY

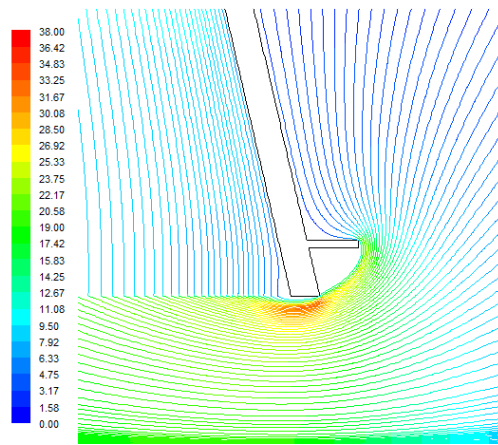


(c) Rounded inlet,  $r_i/d_i$

Figure 2-22 Change in  $d_{ie}/(d_i+2t_s)$  for different inlet geometries compared to a sharp inlet



(a) Sharp inlet



(b) 3 m x 3 m

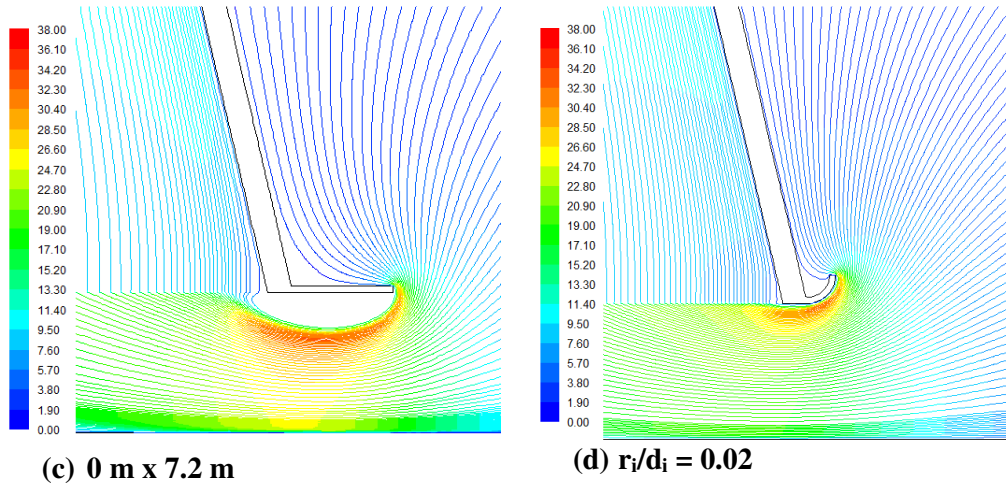


**Figure 2-23 Path-line plots coloured by velocity magnitude, for platforms and a rounded inlet.**

Figure 2-23 (a) to (d) illustrates the path-lines of the air flowing into the tower for  $d_i/H_i = 10.45$  and are coloured to show velocity magnitude. Figure 2-23 (d) illustrates why the trends shown for the rounded inlets  $r_i/d_i = 0.02$  and  $r_i/d_i = 0.025$  in Figure 2-22 (c) are similar. The air flows alongside the inside of the tower and thus there is no room for improving the effective diameter. From Figure 2-23 (b) it is observed that the walkway has similar flow patterns as the rounded inlet in Figure 2-23 (d). This is due to the recirculation of air beneath the walkway, which form eddies that act as a wall to guide the flow entering the inlet to the tower. The velocity gradients at the inlet of the tower and through the heat exchangers are the main contributors to the loss coefficient, which is due to the frictional forces acting within the fluid. This is illustrated clearly in Figure 2-23 when comparing the velocity magnitude path-lines of a sharp inlet to a 3 m x 3 m platform, which shows that the velocity gradients present are larger for the sharp inlet.

The data gathered in this section is used to determine which structures will be investigated on the full-scale model. Four structures are chosen for further investigation namely  $r_i/d_i=0.01$ ,  $r_i/d_i = 0.02$ , 0 m x 3 m, 3 m x 3 m. In addition a platform with dimensions 1 m x 1 m is investigated because from the path line plot of the 3 m x 3 m platform in Figure 2-23 (b) it is seen that decreasing the length and height from the inlet of the platform will result in roughly the same inlet path lines. A  $d_i/H_i = 10.45$  is chosen to investigate these structures since the NDWCT under investigation has the same ratio. The reference value for the heat exchanger loss coefficient is  $K_{he} = 12$ .

**Table 2-12 Full-scale Fluent results for different cooling tower inlet geometries with  $K_{he} = 12$  and  $d_i/H_i = 10.45$**

	$r_i/d_i = 0.01$	$X \times Y = 1 \text{ m} \times 1 \text{ m}$	$r_i/d_i = 0.02$	$X \times Y = 0 \text{ m} \times 3 \text{ m}$	$X \times Y = 3 \text{ m} \times 3 \text{ m}$
$d_{ie}/(d_i + 2t_s)$	0.955	0.957	0.967	0.936	0.967
$v_{m,vc}/v_{m5}$	1.037	1.026	1.005	1.072	1.005
$\alpha_{e,vc}$	1.116	1.069	1.03	1.087	1.03
$K_p$	29.67	28.35	26.41	30.46	26.40
$K_{ct}$ Equation (2-3)	7.52	6.68	5.41	8.02	5.40

Table 2-12 presents the data acquired from the full scale Fluent models. From the table it is deduced that the 3 m x 3m walkway gives the best results due to the walkway having the lowest loss coefficient even though the effective inlet and kinetic energy correction coefficient have the same magnitudes.

## 2.5 Discussion

Through a process of elimination a validated Fluent model is developed to determine cooling tower inlet loss coefficients and effective diameters, minimizing the processing time. The model is an axis-symmetric 2-D model that represents the lower two thirds of the tower and is solved using double precision with the SIMPLE algorithm, the PRESTO! discretization scheme for pressure and the QUICK discretization scheme for the remaining variables. The k- $\epsilon$  realizable turbulence model is identified as the most suitable model and grid independence is achieved by constructing a grid with a triangular mesh. The mesh has a minimum inlet diameter to cell size of 700 at the tower inlet with a growth factor of 1.005 to the inside of the tower and 1.02 to the outside.

The Fluent models are validated with experimental data obtained from a cooling tower sector model. The Fluent model compares well with the experimental data for the sharp inlet geometry and knowledge gained during this exercise is applied in order to determine if the geometry of the tower has an effect on the inlet loss. Data obtained from literature, where a cylindrical cooling tower is used, is taken as reference values [ (1), (2), (3), (4), (6)]. The study shows that the inlet loss of cylindrical cooling towers is more than 10% less than is observed for conical cooling towers. In a conical cooling tower the effective diameter is smaller but the difference is negligible. New empirical relations are proposed for effective inlet diameter and inlet loss coefficient for a NDCT using an anisotropic packing.

From the results of the sharp inlet, it is observed that there is a large area which is not utilized for heat transfer. This prompts an investigation aimed at improving the effective diameter of a NDCT by changing the inlet geometry of the existing tower shell. An experimental study is completed to validate the Fluent models. During this study, protruding platforms and rounded inlets are added to the tower shell in order to change the inlet geometry. The Fluent models constructed for the platforms do not compare well to the experimental data, whilst the rounded inlets do correlate with the data. The inaccuracies of the platform experimental and Fluent data are contributed to the downwards bending of these platforms due to the air flow during the experimental tests. The underestimation of the platforms inlet loss coefficient is due to the increase



of the effective  $d_i/H_i$  ratio which in turn increases the inlet loss. In the Fluent models the platforms are not subjected to bending and thus it is difficult to quantify this effect without constructing different Fluent models to study it.

The Fluent model is used to investigate other inlet geometries to the tower. Two types of structures are implemented to alter the inlet geometry namely protruding platforms and rounded inlets. A rounded inlet with dimensions  $r_i/d_i = 0.02$  produces the best results for the size of the structure. However, it will be difficult to add the inlet to an existing tower. From the modelling results it is found that the 3 m x 3 m platform produces similar results to the aforementioned rounded inlet. The similarity in results is contributed to the recirculation zone that forms beneath the platform, which form eddies that act as a wall too guide the flow entering the inlet to the tower. The platform also produces a more consistent improvement to the loss coefficient of the tower. Further investigation leads to the observation that a 1 m x 1 m platform also reduces the loss coefficient substantially and increases the effective diameter. This platform requires the least amount of material and still delivers satisfactory results when compared to the other cases examined.

### 3 Modelling of flow around a cylinder

It is important to accurately model the pressure distribution around and downstream of the cooling tower shell when investigating the effect of a crosswind on a NDCT. The pressure distribution around the tower will affect the flow into it whilst the turbulent wake downstream of the tower determines the path of the plume. The prediction of plume path is important in cases where hazardous substances in the drift and ice formation can have negative impacts on the environment, roads, health, etc.

Catalano et al (14) is the only article which was possible to access on the subject of CFD modelling of flow of air around a cylinder and according to this article most of the current research is being done with the large eddy simulation (LES) model. Catalano et al (14) simulated the flow around a cylinder with the aid of Fluent to compare the LES and standard k- $\epsilon$  models at a Reynolds number of  $1 \times 10^6$ . The results of the k- $\epsilon$  model correlated with the experimental data of Zdravkovich (15) and Warshauer et al (16). Catalano's work is relevant to towers experiencing wind velocities below 0.2m/s, which is rarely the case for the tower under investigation.

Alberti (17) investigated the influence of wind effects on a solar chimney and analyzed the flow around a circular cylinder with the aid of Fluent and experimental work. The Reynolds number for her evaluation is  $4.95 \times 10^5$ , which falls within in the critical regime. This low value is due to excessive vibration in the experimental model at higher Reynolds numbers. The Fluent and experimental results correlated well.

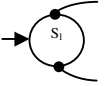
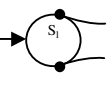
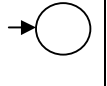
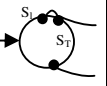
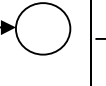
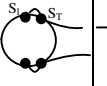
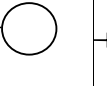
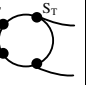
The objective of this chapter is to determine the capability of Fluent to model the flow around a circular cylinder using a Reynolds Averaged Navier Stokes (RANS) model in order to supplement the work done on the inlet of a NDCT in the previous chapter. To achieve this objective a two dimensional numerical model is developed using Fluent and validated with the aid of data from literature. A three-dimensional model is ultimately developed by applying information gained from the two dimensional models to investigate the difference in the pressure distribution and wake flow between finite and infinite cylinders.

The results of the Fluent model are presented in dimensionless form in terms of the surface pressure coefficient and velocity ratio to simplify the comparison with results obtained by other researchers. The chapter consists of the following sections:

- Introduction: This section gives the general background for examination of the flow around a circular cylinder.
- Theory: In this section the relevant theory applicable to flow around a cylinder is outlined.
- Modelling procedure: In this section the influence of the turbulence model, grid independence, surface roughness and turbulence parameters on the numerical results are investigated and the results are interpreted.
- Results: This section compares Fluent results to literature to determine accuracy.
- Discussion of the results: In this section a summary of the chapter's findings are presented

### 3.1 Theory

**Table 3-1 Different regimes encountered for flow around a smooth cylinder (18)**

	Subcritical	Critical				Super-Critical	Upper transition	Trans-Critical
Sub-regime regions	1	2	3	4	5	6	7	8
state of boundary layer	stable		unstable	bi-stable	unstable	stable	unstable	stable
$10^5 Re$	1.4		2.8	3.0	3.3	3.5	10	50
Mean drag coefficient $c_D$	1.2	1.2-1	1.0-0.7	0.5	0.5-0.4	0.22	0.22-0.52	0.5-0.85
Mean lift coefficient $c_L$	0			$\pm 1.3$	1.3-0.9	0	0.1-0.2	0.5
St	0.2		0.2	0.33	0.31	0.48	(0.1/0.45)	0.28
$CL_{RMS}$	0.4-0.25	0.25-0.09	0.09-0.06	0.04	0.04-0.07	0.02	0.04	0.05
Boundary layer separation	 Laminar separation, $S_l$	 Laminar separation	 Random changes	 One-sided separation bubble	 Random changes	 Two-sided separation bubble	 Random changes	 Turbulent separation, $S_t$

The flow around a smooth cylinder with infinite length has been studied quite excessively in the past century as summarized by Niemann and Holsher (18). The flow characteristics are very dependent on the Reynolds number ( $Re$ ) as well as the turbulence levels in the free stream flow approaching the cylinder (18). Schewe (19) determined that there are four main flow regimes to which the flow around a cylinder can be subjected to, i.e. subcritical, critical, supercritical and trans-critical. A summary of these regimes are presented in Table 3-1. In all four of these regimes, the shedding of vortices occurs and the frequency is obtained from the dimensionless Strouhal number ( $St$ ), defined for a circular cylinder as follows:

$$St = \frac{\omega d}{2\pi v} \quad (3-1)$$

where  $d$  is the diameter,  $v$  is the free-stream velocity and  $\omega$  is the shedding frequency in radians per second.

Figure 3-1 represents the plot of the drag coefficient for a circular cylinder with a smooth and rough surface in terms of the Reynolds number and the different flow regimes, which are for the smooth cylinder only. In the subcritical range the boundary layer is laminar throughout the circumference until separation occurs, which is normally at an angle of between  $70^\circ$  and  $80^\circ$ . This regime concludes at a  $Re$  of around  $1.4 \times 10^5$ . The boundary between subcritical and critical flow is defined as the onset of randomized lift fluctuations, which starts at a  $Re$  of around  $2.8 \times 10^5$  (19). Up until this value, vortex shedding takes place at more or less a constant frequency. The range from a  $Re$  of  $1.4 \times 10^5$  to  $2.8 \times 10^5$  (modes 1 and 2) is included within the critical regime, since the drag coefficient of a cylinder departs from a more or less constant value of 1.2 to a lower value due to the downstream shift of the laminar separation point (18).

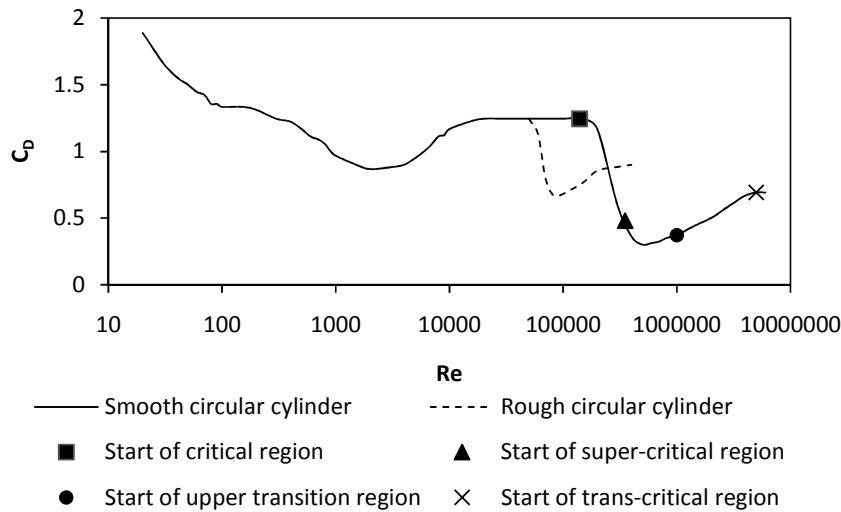


**Figure 3-1 Drag coefficient of circular cylinder for smooth and rough cylinders (17)**

The critical regime extends to a  $Re$  of  $3.5 \times 10^5$ , which is defined as the point where the lowest drag coefficient is found (18), and can be categorized into four ranges. An intermediate range, 4, is observed where laminar separation is followed immediately by transition to turbulent conditions in the free shear layer and turbulent reattachment. Turbulent separation consequently occurs downstream of the turbulent reattachment and  $St$  increases in relation to the value of the subcritical regime. The region between the laminar separation point and turbulent reattachment is called the “separation bubble” (18), which appear alternately on one side. Preceding this region is an unstable situation, 3, where the boundary layer jumps between laminar and turbulent separation which results in random lift fluctuations. A second unstable range, 5, follows the intermediate range until a separation bubble occurs on both sides, which represents range 6.

The next region is called the super-critical regime, 6, and is characterized by a fairly constant and low drag coefficient with a separation angle in the region of  $140^\circ$ . Separation bubbles appear on both sides of the cylinder and the vortex shedding frequency increases. In the following upper transition range, the separation bubbles disappear and the transition point from laminar to turbulence state of flow in the boundary layer,  $T$ , is shifted upstream as  $Re$  increases. The trans-critical regime, 8, is defined as the stage when the transition point and the separation point have more or less constant positions. The transition from a laminar to turbulent boundary layer is shifted almost to the stagnation point and the boundary layer separation is shifted forward to a position in the region of  $110^\circ$  as a result of higher friction loss (18). The drag coefficient also increases compared to the super-critical regime.

The surface roughness of the cylinder wall has a significant effect on the transition from a laminar to turbulent boundary layer since the increase in shear forces promote unstable flow (18). An increase in surface roughness has little effect on the subcritical drag coefficient and the critical regime shifts to a lower  $Re$ . The critical regime range decreases as roughness is increased and disappears altogether for moderate values of

roughness ( $k_s/D > 10^{-3}$ ) (18). For very rough surfaces, the critical region may even become a sudden drop from subcritical drag to the minimum drag found in the critical region. The surface roughness also stabilizes the flow field, which results in a decrease of the Strouhal number, while the drag increases as roughness is increased. The trans-critical regime's drag coefficient increases, since the transition point shifts closer to the stagnation point when roughness is increased and, for both the trans-critical and critical regime, it increases asymptotically for very rough surfaces. The separation bubble is affected by this and as such is confined to a region just behind the critical  $Re$  or does not occur at all if the surface is too rough.

Ribeiro [ (20), (21)] conducted extensive experiments on the effect of surface roughness on pressure distribution and flow characteristics around a circular cylinder. He determined that the greater the relative roughness, the greater the deviation of the mean pressure distribution became relative to that observed for smooth circular cylinders at the same  $Re$ . He also noted that with the increase in relative roughness, secondary vortices started to form at the separated boundary layer. The structures of these vortices are distinct from the von Karman vortices. According to Ribeiro [ (20), (21)], a condition of resonance would be established through these secondary vortices, which will amplify the size of the von Karman vortices. This is due to the von Karman vortices incorporating in their formation the action of these secondary vortices, in addition to the effect of the base pressure fluctuations.

The free stream turbulence has various effects on the transitional behaviour [ (18), (20), (21)] starting with random fluctuations of lift, drag and local pressure. The fluctuating force and pressure coefficients for turbulent flow across rough and smooth circular cylinders are similar [ (20), (21)]. The free stream turbulence also affects the spanwise correlation of vortex shedding and results in the vortices losing strength and stability. The transitional  $Re$  decreases as turbulence intensity increases since the separation point angle is shifted closer to the stagnation point, due to earlier transition from laminar to turbulent flow in the boundary layer, whilst the drag in the subcritical regime decreases. For the super-critical regime the opposite is true, however the separation point angle still increases along with turbulence intensity. It is suggested by Ribeiro (20) that the free stream turbulence not only penetrates the boundary layer, but also interacts with the free shear layer, which alters the transitional behaviour and shifts the transition from a laminar to turbulent boundary layer to a lower  $Re$ . Increased turbulence intensity causes the Strouhal number to increase, while simultaneously the span wise correlation of vortices and root mean squared (RMS) lift forces are decreased in the subcritical and increased in the super-critical condition (20). If the turbulence vortices are at the same frequency as the secondary vortexes there is a resonance effect that amplifies the von Karman vortices [ (20), (21)].

With a finite cylinder, additional three-dimensional effects start to appear which change the flow behaviour downstream of the cylinder. Firstly, air flows over the top as well as around the cylinder tip, which is the free end of the cylinder, and forms a pair of symmetric stationary vortices further downstream, which is known as the tip effect (18). These vortices cause recirculation of the main flow over the top in the near wake and relieve nearly the whole surface pressure distribution around the cylinder except in the tip region. The tip effect depends on the pressure difference between the front and the rear faces of the cylinder and thus it is expected to be more vigorous in the trans-critical regime, with its smaller wake and lower base suction,

than subcritical Reynolds number range (18). Up to a length to diameter ratio of fifty, the average local drag coefficient is lower than the total drag of an infinite circular cylinder.

The maximum pressure fluctuations occur near the cylinder tip and the RMS lift coefficient accomplishes the highest value at nearly a half diameter away from the free end of the model. Ayoub and Karamcheti (22) found coherent vortex shedding with one single  $St$  of 0.19 up to a short distance from the tip. Farivar (23) noted a stepwise decrease of the shedding frequency towards the cylinder end, five diameters downstream of the cylinder. He concluded that beyond the regular formation region a cellular vortex structure is formed. Sakamoto and Arie (24) found that in the case of circular cylinders the type of vortex shedding changes from the von Karman type to the arch-type with decreasing aspect ratio.

## 3.2 Modelling procedure

### 3.2.1 Definition of nomenclature used in this chapter

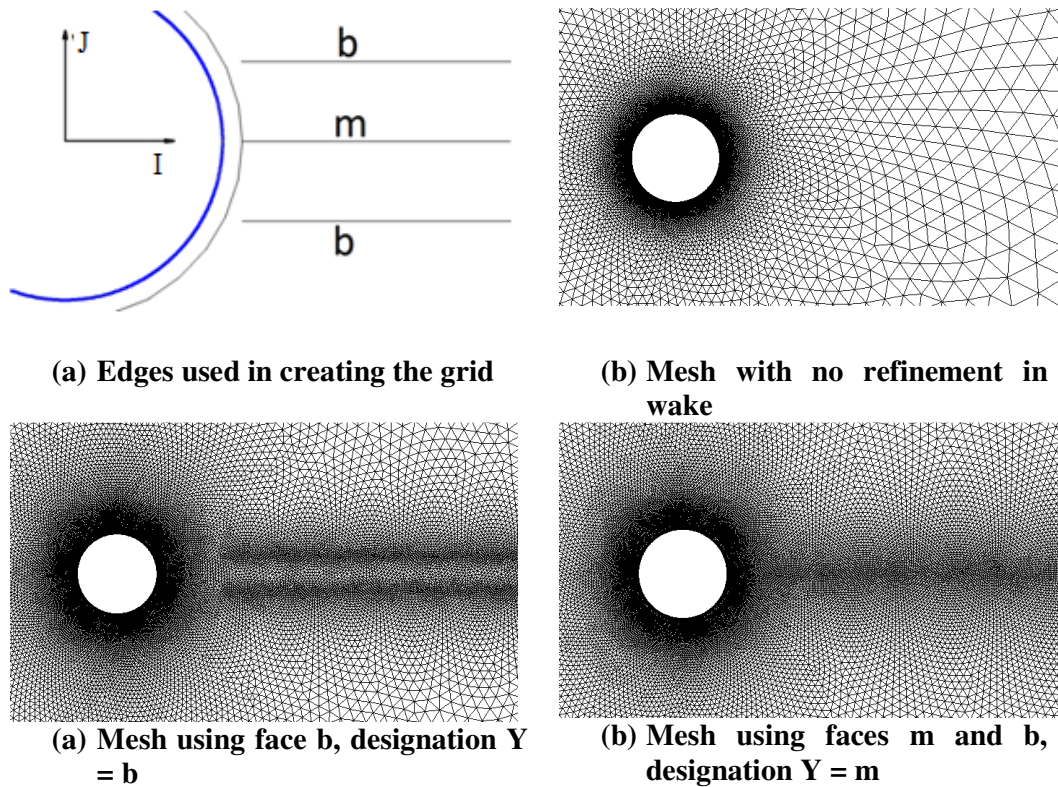


**Figure 3-2** Illustration of different definitions for mesh refinement in the wake region

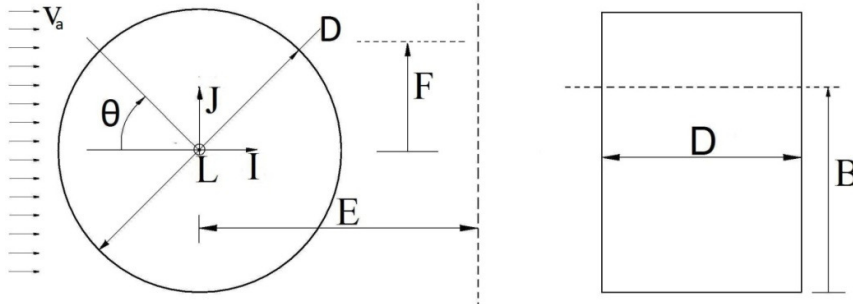


**Figure 3-3 Coordinate system for cylinder analysis**

Figure 3-2 provides a visual representation of the mesh formation for the cylinder analysis. Figure 3-2 (a) illustrates the edges used to generate the grid with the aid of sizing functions in Gambit, while Figure 3-2 (b), (c) and (d) represent the three types of meshes. This method for generating the mesh is used to determine grid independence and the influence that the boundary layer and wake refinement have on the results. When face m is used, face b is included, in the sense that both have a sizing function attached to them, which is necessary to obtain the form as illustrated in Figure 3-2 (d). The growth rate of the sizing function attached to faces b is 1.05, while those attached to the cylinder surface and face m are 1.1. The legends on the graphs to follow are given as: X, Y-Z, where X is the cylinder diameter to the starting boundary cell height ratio on the surface of the cylinder, Y designates the faces used according to Figure 3-2 (a) to (d) and Z is the cylinder diameter to the starting cell size ratio for the faces specified by Y. When Y-Z is omitted then there is no mesh refinement downstream of the cylinder. Figure 3-3 illustrates the coordinate system for the cylinder analysis, while the distance (E) is measured downstream of the cylinder.

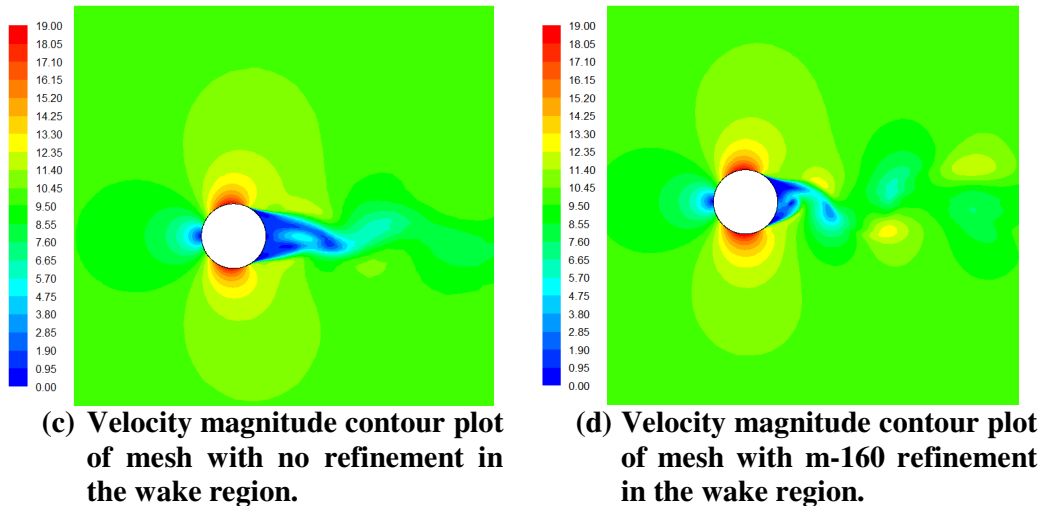


**Figure 3-4 Difference in flow patterns between refinement and no refinement in the wake area**

Figure 3-4 illustrates the difference in flow patterns when the grid in the wake region downstream of a cylinder is refined. From these plots, it is obvious that refinement in the wake area is crucial when determining the pressure and velocity profiles for the

wake and the cylindrical surface. The pressure on the surface of the cylinder is represented in terms of the dimensionless pressure coefficient, which is defined as:

$$C_p = \frac{p - p_a}{0.5\rho v_a^2} \quad (3-2)$$

where  $p$  is the static pressure at a point on the surface,  $p_a$  is the upstream static pressure and  $v_a$  is the average upstream velocity.

### 3.2.2 Influence of variables in Fluent

The flow around an infinite circular cylinder is simulated with Fluent using a two-dimensional double precision solver, the SIMPLE algorithm, which is used for pressure-velocity coupling and second order discretisation scheme for all equations. The flow field is modelled as unsteady and time dependent. The Reynolds number used is  $52.9 \times 10^6$ , which is in the order of what NDCTs are exposed to. The effect of different parameters on the flow around the cylinder is examined, namely the boundary layer creation, grid independence, turbulence model, surface roughness, turbulence intensity and turbulent length scale.

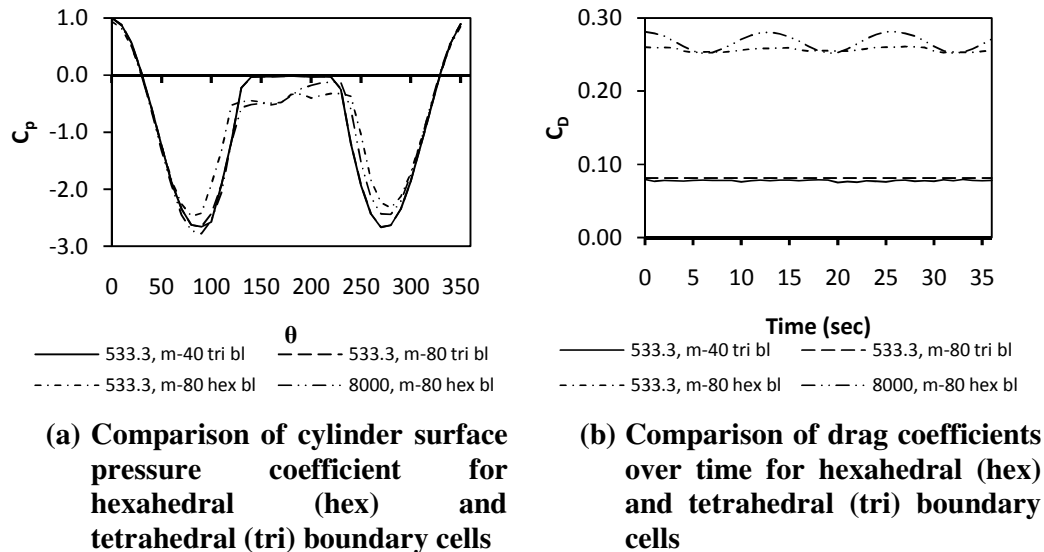


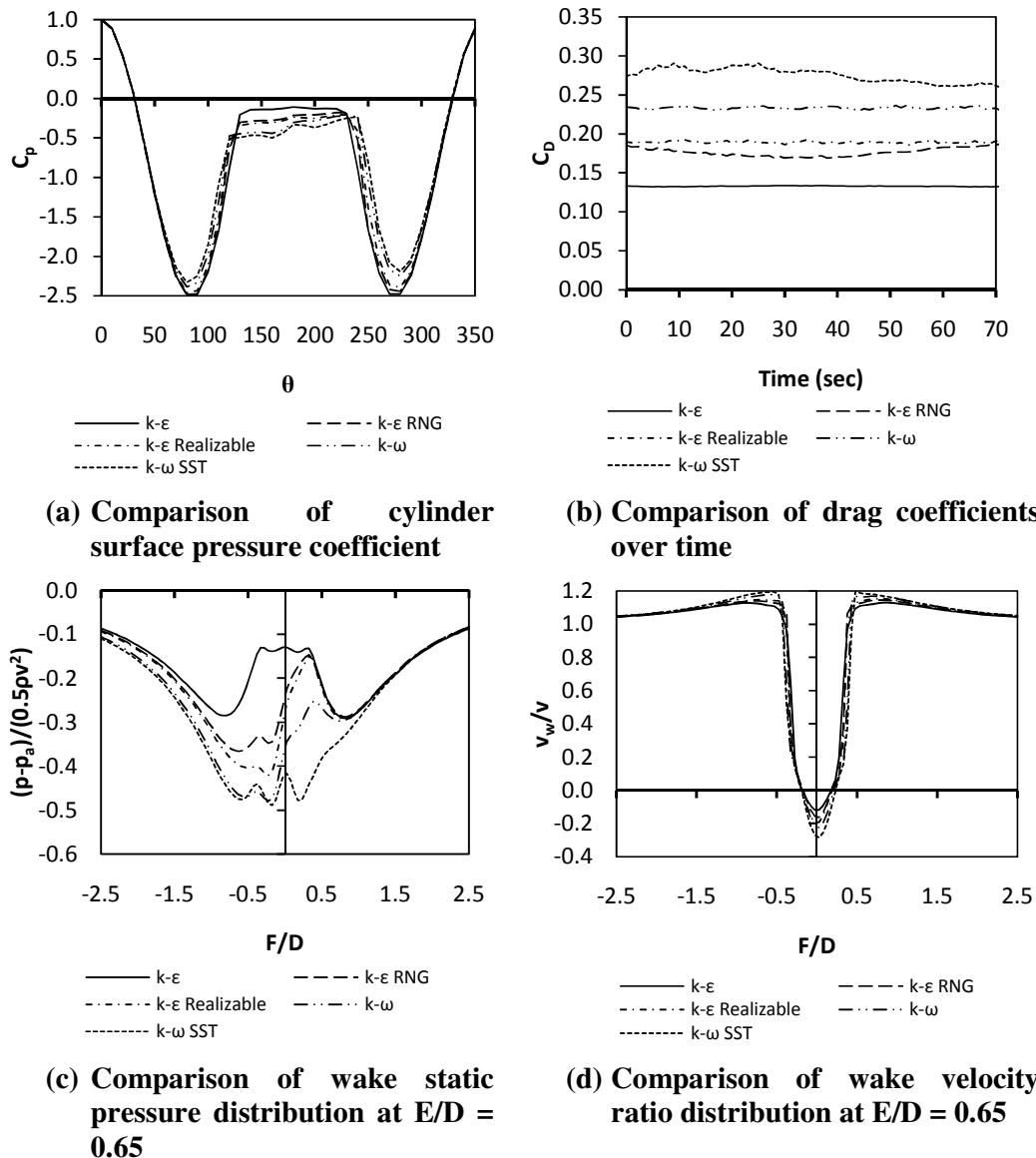
**Figure 3-5 Effect of boundary layer grid type on the pressure and drag coefficients**

The boundary layer size and wake refinement have an effect on the pressure distribution calculated on the surface of a cylinder. The formation of the boundary layer is limited by Gambit to a cylinder diameter to cell height ratio of 8000, where  $D = 80$  m. Below this ratio it is difficult to create an accurate representation of the cylinder and discontinuities start to appear. The elements are then grown at a rate of 1.05 away from the cylinder. However, this ratio results in a maximum  $y^+$  value of 211 on the surface of the cylinder and is important since the boundary layer equations are only valid if  $30 \leq y^+ \leq 300$ .

Figure 3-5 gives the results of an investigation into the correct mesh element to use for the construction of the boundary layer. For the case with  $X = 533$ , the  $y^+$  values mentioned above are not satisfied when using the hexahedral boundary layer,

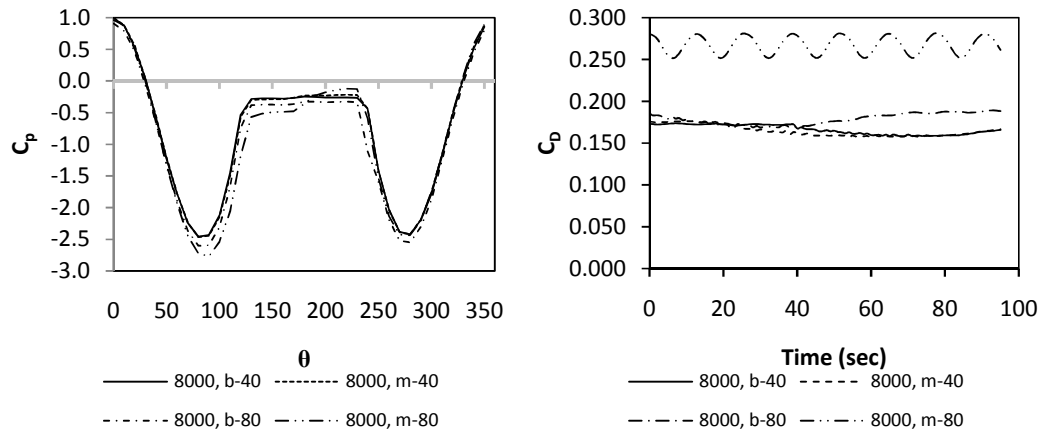


although this mesh element yields a better representation of the cylinder pressure distribution and drag coefficient. From examination of the boundary layer it is discovered that in order to create a stable boundary layer, it must consist of hexahedral elements and be at least a distance of  $D/3$  away from the cylinder in the radial direction, before the grid becomes triangular. If the boundary layer is constructed otherwise, there is an over recovery of pressure downstream of the cylinder as is apparent from Figure 3-5. It is also noted that refinement of the mesh in the wake region does not have a significant effect if the boundary layer is not constructed using hexahedral elements with the required radial distance away from the cylinder of  $D/3$  in the radial direction.



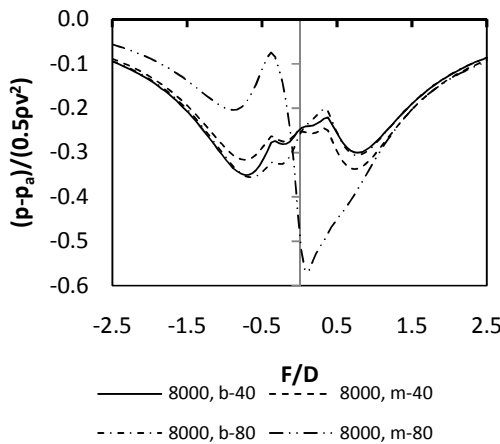
**Figure 3-6 Comparison of different turbulence models for the two-dimensional cylinder model**

Figure 3-6 compares the different turbulence models investigated. A mesh with no refinement in the wake is used to reduce simulation time. It is noted that the  $k-\varepsilon$  RNG and realizable models predict the same pressure coefficients around the cylinder, whilst the pressure and velocity profiles downstream differ as shown in Figure 3-6 (c) and (d). Thus it is apparent that the results are dependent on the mathematical turbulence creation and dissipation which take place in the wake. The standard  $k-\varepsilon$  model predicts a higher pressure recovery than the other models as observed from Figure 3-6 (a) and (c). Although the  $k-\omega$  models predicts a more realistic drag coefficient, the  $k-\varepsilon$  realizable has the shortest simulation time and thus during the mesh refinement process the  $k-\varepsilon$  realizable model is used.

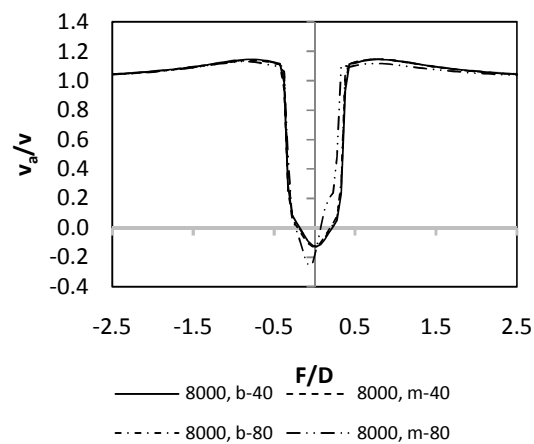


(a) Comparison of cylinder surface pressure coefficient

(b) Comparison of drag coefficient over time



(c) Comparison of static pressure distribution in wake at  $E/D = 0.65$



(d) Comparison of the wake velocity ratio distribution in wake at  $E/D = 0.65$

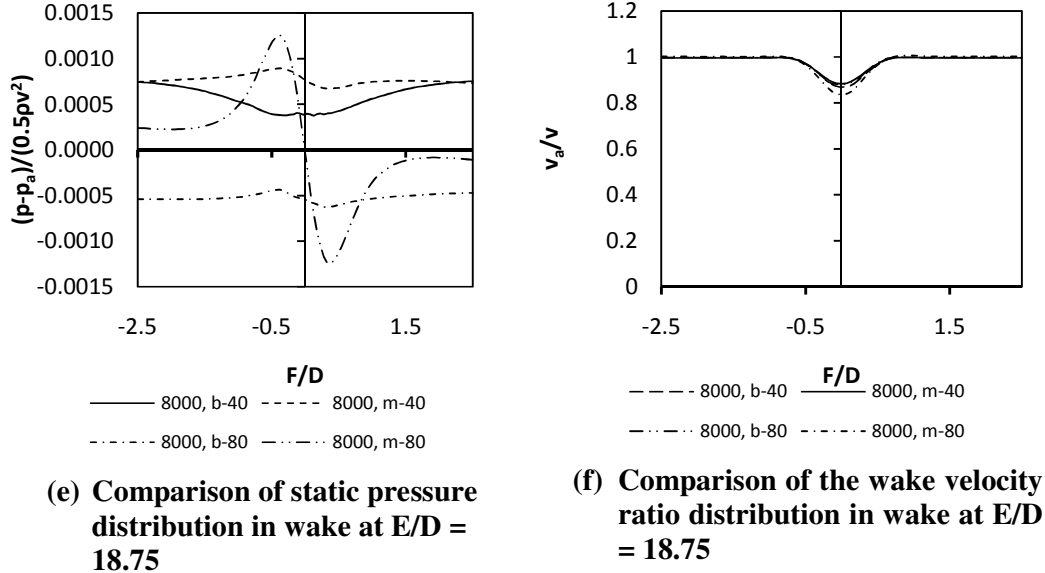
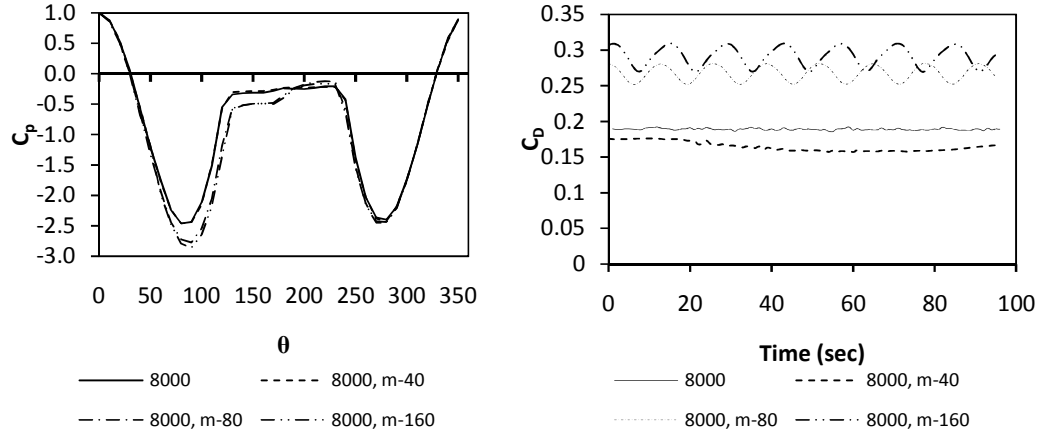


**Figure 3-7 Comparison of the different methods of grid refinement in the wake**

Figure 3-7 represents a comparison of the results obtained for different types of grid refinement in the wake, whilst keeping the boundary cell height constant in order to eliminate this influence. From Figure 3-7 (a) it is apparent that the type and size of refinement has an effect on the pressure distribution around the cylinder. Figure 3-7 (b) illustrates the difference in the drag coefficient as the time interval increases and indicates that boundary layer stability is affected by refinement in the wake. Other effects also observed is the change in drag coefficient and the frequency at which vortex shedding takes place, which changes with the method of refinement.

Figure 3-7 (c) illustrates that the effect of grid refinement is greater on static pressure distribution downstream of the cylinder than on the wake velocity distribution as noted in Figure 3-7 (d). It is observed from Figure 3-7 (e) that when using  $Y = m$  and refining the grid to  $Z \geq 80$ , the pressure distribution still has the form observed in Figure 3-7 (c), while those with  $Z \leq 80$  predict a constant pressure. However this difference is negligible since it is more than two orders of magnitude smaller at  $E/D = 18.75$  than at  $E/D = 0.65$ . When observing Figure 3-7 (f) it is apparent that the difference between free stream and wake velocity is significant at a distance of  $18.75D$  from the cylinder. The above comparison leads to the conclusion that the refining method which should be used, should have  $Y = m$  and  $Z \geq 80$ .



(a) Comparison of cylinder surface pressure coefficient

(b) Comparison of drag coefficients over time

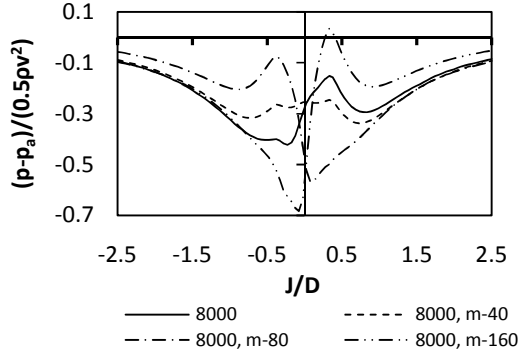
**Figure 3-8 Comparison of cylinder surface pressure coefficient for different grid refinements in the wake with  $Y = m$**

Figure 3-8 represents a comparison of the cylinder surface pressure coefficient and drag coefficient for different grid refinements in the wake using  $Y = m$ . From Figure 3-8 (a) and (b) it is apparent that increased accuracy for the static pressure profile around the cylinder, minimum static pressure on the surface of the cylinder, drag coefficient and  $St$  is:

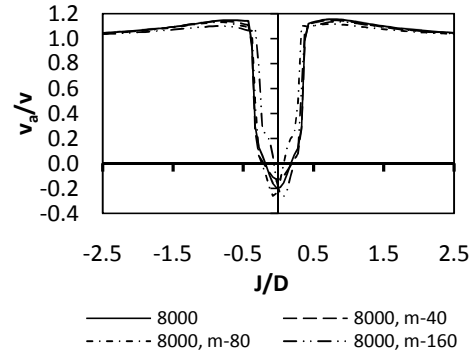
- negligible from no refinement to  $Z = 40$
- significant from  $Z = 40$  to  $Z = 80$
- negligible for  $Z = 80$  and  $Z = 160$

It is also noted that the angle at which boundary layer separation occurs is dependent on the refinement of the wake. Figure 3-8 (b) illustrates that the drag coefficient for no refinement and for  $Z = 40$  deviate minimally from the mean value, thus little vortex shedding is expected, while  $Z = 80$  and  $Z = 160$  both predict vortex shedding. The frequency of vortex shedding for  $Z = 80$  is higher when compared to  $Z = 160$ , while the magnitude of the peak to trough value is lower.

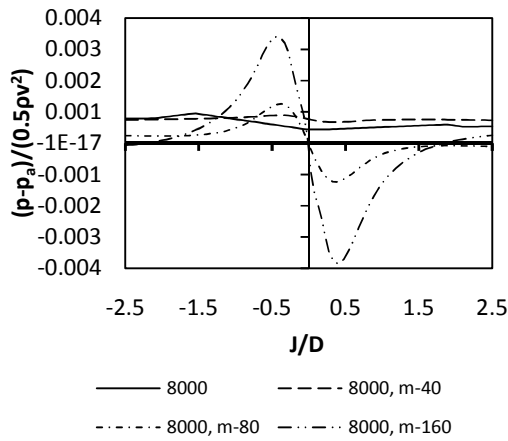
Figure 3-9 illustrates the pressure and velocity profiles behind the cylinder at specified locations. When studying Figure 3-9 (a) and (b), it is apparent that no wake refinement yields a better representation of the pressure profile behind the cylinder than when  $Z = 40$ . This can be due to the cells in the wake not being small enough to obtain an accurate mathematical prediction of the velocity gradients present in the air stream because of these eddies when  $Z = 40$ , whereas when there is no refinement the eddies can be encompassed in a single element. When comparing  $Z = 80$  to  $Z = 160$ , it is apparent that no significant difference are present between the velocity profiles, but a 17% difference in pressure profile peaks is observed. Grid independence is not achieved, but refining the mesh further increases the size to an extent that makes the available computing power inadequate.



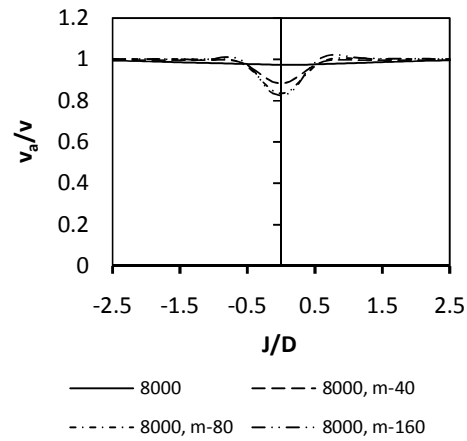
(a) Comparison of static pressure distribution in wake at  $E/D = 0.65$



(b) Comparison of axial velocity ratio distribution in wake at  $E/D = 0.65$



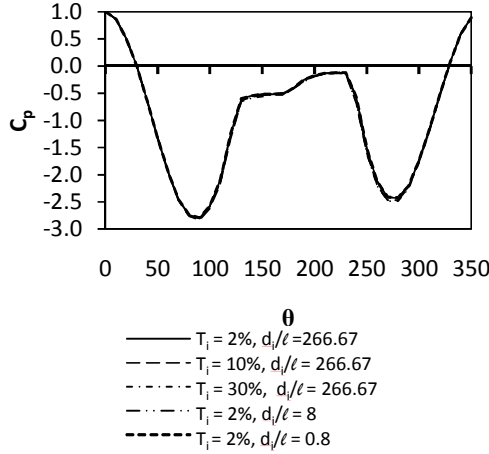
(c) Comparison of static pressure distribution in wake at  $E/D = 18.75$



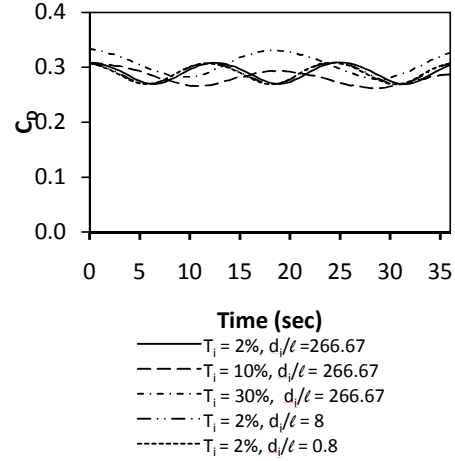
(d) Comparison of axial velocity ratio distribution in wake at  $E/D = 18.75$

**Figure 3-9 Comparison of wake refinement results with  $Y = m$**

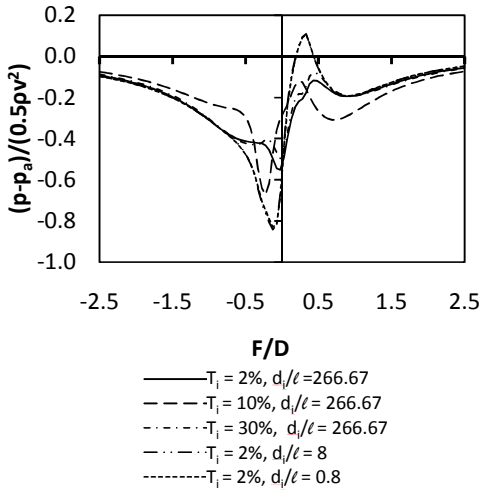
Figure 3-9 (c) and (d) represents a comparison of the pressure and velocity profiles at a distance of  $E/D = 18.75$  for different values of  $Z$ . At this distance, the predicted effect of the von Karman vortices increase as the value of  $Z$  increases. The fluctuations observed in the pressure profiles are assumed negligible since the average pressure in all four profiles is less than two orders of magnitude smaller than the profile at  $E/D = 0.65$ . The velocity profile has a substantial deviation of 20% from the free stream velocity in the wake. Increasing the distance of the mesh downstream of the cylinder to achieve a constant velocity profile is not feasible with the current computing power.



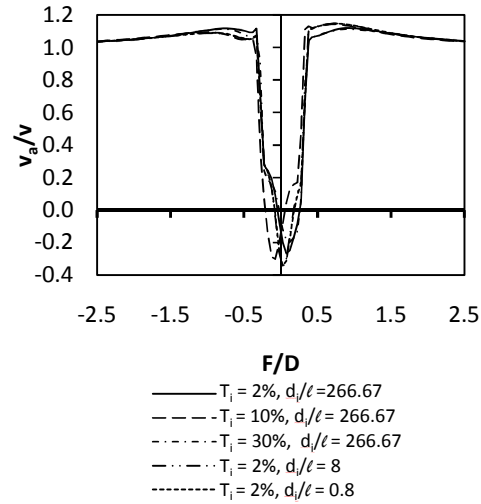
(a) Comparison of cylinder surface pressure coefficient



(b) Comparison of drag coefficients



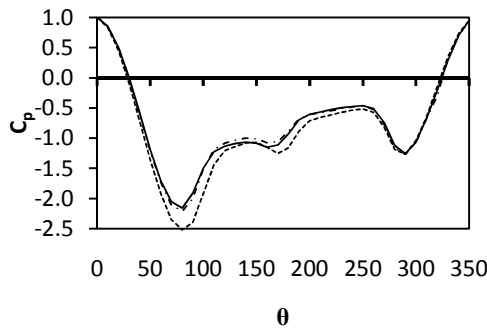
(c) Comparison of static pressure distribution in wake at  $E/D = 0.65$



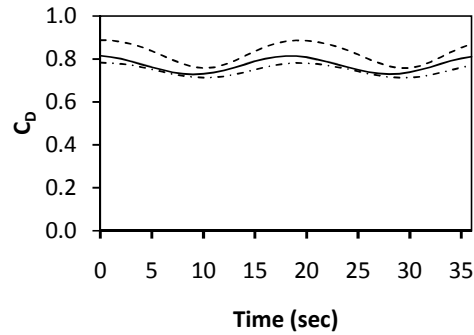
(d) Comparison of axial velocity ratio distribution in wake at  $E/D = 0.65$

**Figure 3-10 Comparison of cylinder parameters for different turbulence parameters**

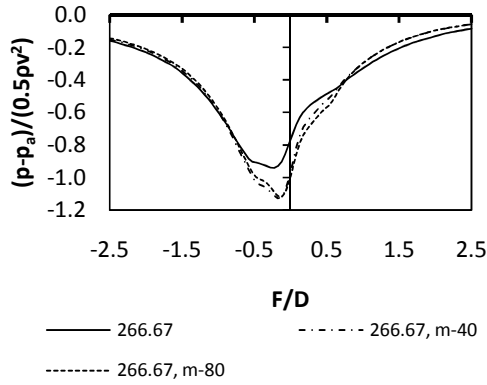
Figure 3-10 represents the results for different turbulence parameters. Figure 3-10 (a) illustrates that both the turbulence intensity and length scale have no effect on the pressure distribution around the cylinder. Figure 3-10 (b) indicates that the turbulence intensity does have an effect on the vortex shedding frequency and that as the turbulence intensity increases, the frequency with which vortices are shed decreases, as noted by Ribeiro (20). Figure 3-10 (c) and (d) indicates that both parameters influence the respective profiles and that the turbulence intensity has the lesser effect. In addition, it is apparent that the turbulence length scale only has an effect from a ratio of 266.67 to 8. Beyond the value of 8 the change in the pressure and velocity profiles are negligible. The lack of experimental data on the effect of these two parameters on the flow field behind the cylinder results in the inability to determine which of the combinations is the more accurate representation when modelling a NDCT.



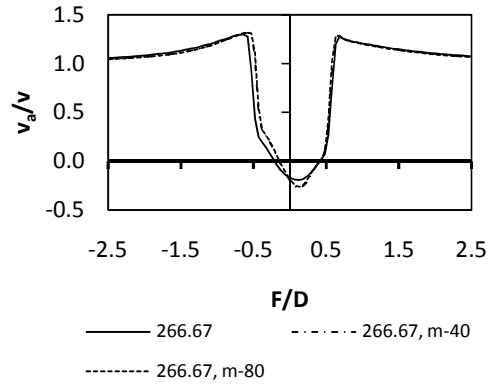
(a) Comparison of cylinder surface pressure coefficient



(b) Comparison of drag coefficients



(c) Comparison of static pressure distribution at  $E/D = 0.65$



(d) Comparison of axial velocity ratio distribution at  $E/D = 0.65$

**Figure 3-11 Comparison of results for cylinder surface roughness of  $k_s/D = 1.5 \times 10^{-3}$**

Figure 3-11 represents the effect surface roughness has on the distribution around a cylinder. In Fluent, the roughness is modelled by applying a modified version of the law of the wall, which requires that the wall-adjacent cell centroid be higher than the roughness height ( $k_s$ ). This requirement is met by using a diameter to wall-adjacent cell height ratio of 266.67 and a roughness height to diameter ratio of  $k_s/D = 1.5 \times 10^{-3}$ . The grid refinement process is again implemented in order to observe the effect roughness would have on the flow field and to determine if fewer cells can be used. From Figure 3-11 it is observed that the difference in the velocity and pressure profiles for  $Z=40$  and  $Z=80$  are negligible, whereas a significant effect is seen for the cylinder pressure distribution and the drag coefficient. Thus, the conclusion can be made that the finest possible mesh must be used downstream of the cylinder in the wake.

The following conclusions are drawn:

- The boundary layer must be created with hexahedral elements and be extended at least a radial distance away from the cylinder of  $D/3$ .

- The k- $\epsilon$  realizable model should be used due to consideration of processing time and accuracy.
- The refinement process downstream of the cylinder should be done using a grid with a minimum configuration of m-80.
- The turbulence parameters have an insignificant influence on the pressure profile around the surface of the cylinder, while the opposite is true for the frequency at which vortices are shed. This is due to the free stream turbulence penetrating the boundary layer and interacting with the free shear layer of the cylinder.
- Surface roughness has a profound influence on the frequency of vortex shedding, pressure profiles around the cylinder and in the velocity profiles in the wake. This is due to the stabilizing effect that surface roughness has on the flow around a circular cylinder.

### 3.3 Results

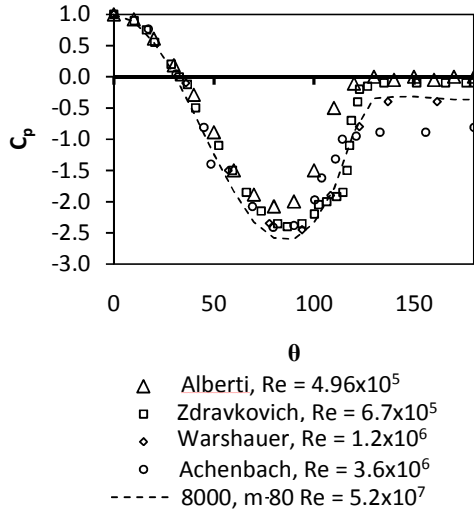
The validity of the Fluent model for flow around a smooth circular cylinder cannot be determined due to a lack of experimental data for flow in the trans-critical regime. Subsequently an attempt is made to compare the results with the available data even though it falls within different flow regimes. Unless stated otherwise, all the models simulated in this section are given the following input variables:

- $Re = 5.2 \times 10^7$ , which is based on the average free stream velocity upstream of the cylinder.
- The k- $\epsilon$  realizable model is used with the second-order upwind discretization technique.
- Reference pressure,  $p_{ref} = 100\,000$  Pa.
- A cylinder diameter of  $D = 80$  m.
- Turbulence intensity,  $T_i = 2\%$ .
- Turbulent Length scale,  $\ell = 0.3$  m.

#### 3.3.1 Comparison of 2-D analysis with literature

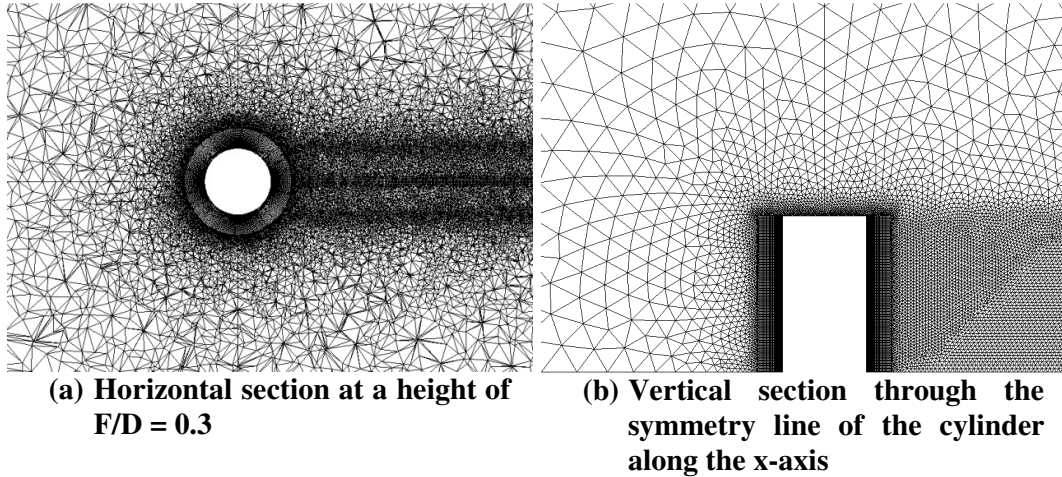
Figure 3-12 represents a comparison between averaged results for smooth circular cylinder pressure coefficient distributions from literature experiments and those obtained from Fluent. Figure 3-1 shows that the drag coefficient increases in the super-critical regime and this is a result of the weaker pressure recovery behind the cylinder with increasing Reynolds numbers, as shown in Figure 3-12. It is also noted that the drag coefficient increases steadily when moving into the trans-critical regime where after it starts to level off at a number around  $4 \times 10^6$ . It is unclear what happens to the drag coefficient beyond this Reynolds number and thus the validity of the Fluent result cannot be commented on. The assumption is made that the results are accurate based on the work of Alberti (17) and Catalano et al (14), where their Fluent models predictions compare well with their experimental data.





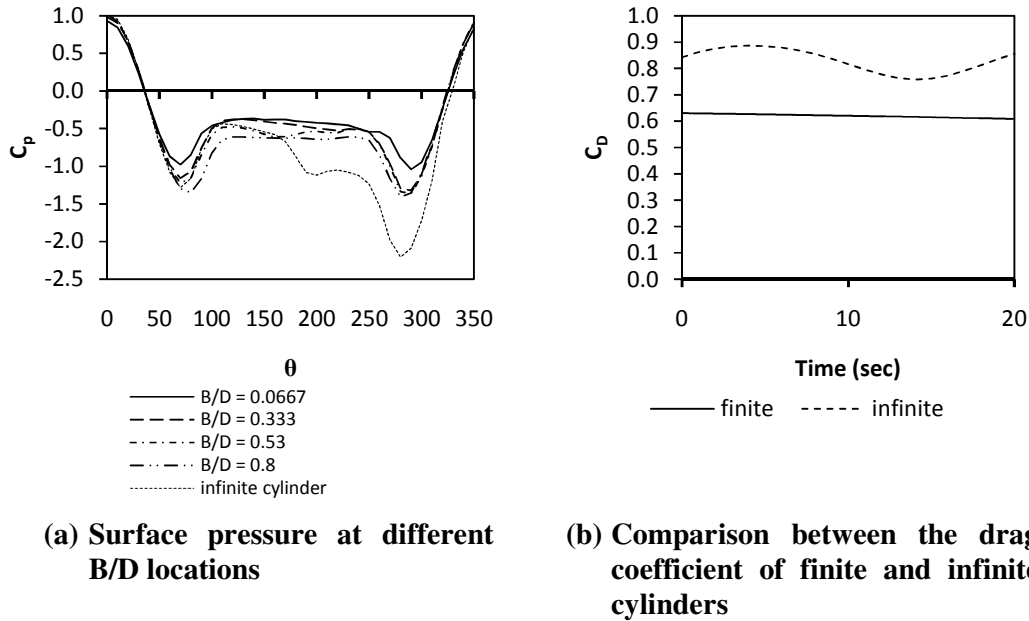
**Figure 3-12 Comparison of averaged pressure coefficient results from Fluent with literature for an infinite smooth circular cylinder**

### 3.3.2 3-D analysis



**Figure 3-13 Illustration of the three dimensional grid for the finite circular cylinder investigation**

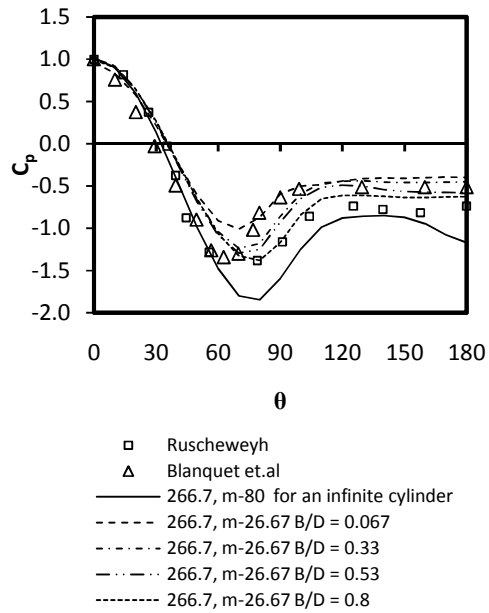
Figure 3-13 displays the grid of a three-dimensional mesh created to investigate the flow over a finite cylinder with a rough surface in order to compare the results with those found in literature. The roughness is assumed to be a uniformly distributed sand grain roughness and a roughness height of  $1.5 \times 10^{-3}$  is specified. A cylinder with a diameter to height ratio of 0.53 is used to match the dimensions of a typical full scale NDCT. Using the same approach as for the two dimensional case, a grid is constructed with the form (266.67, m-26.67). The faces used for refinement in the wake region have the same height as the tower and the boundary layer growth rate is 1.05 until it reaches a distance of  $D/3$  after which the growth rate is 1.2 due to limited computing capacity.



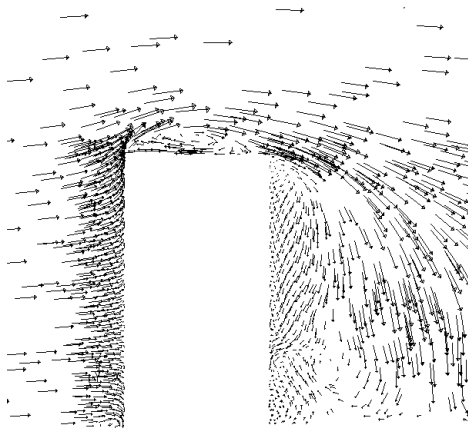
**Figure 3-14 Comparison between the surface pressure distribution and drag coefficients of finite and infinite cylinders**

Figure 3-14 represents a comparison of the surface pressure distribution of a rough finite circular cylinder, for different B/D values, with that of a rough infinite cylinder. From Figure 3-14 (a) it is apparent that the span wise distribution of the pressure coefficient differs for the infinite cylinder, as noted by Niemann and Hölcher (18), which is due to the pair of stationary symmetric vortices that form further downstream. This effect is illustrated in the paragraphs to follow. Figure 3-14 (b) compares the drag coefficient of an infinite and finite circular cylinder. The drag coefficient of the finite cylinder is lower as expected due to the tip effect. It is also apparent that the boundary layer is more stable due to a much lower Strouhal number and fluctuation magnitude of the drag.

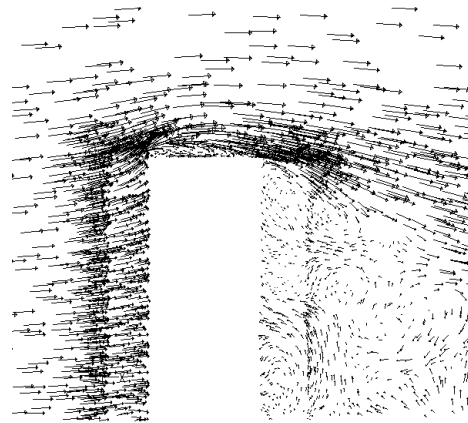
Figure 3-15 represents a comparison between the average circular cylinder pressure coefficient data from literature and Fluent with a rough surface. Since Ruscheweyh (25) and Blanquet et al (26) completed their measurement on full scale NDCT's, their work is deemed valid for this comparison. The Fluent results correlate well with the data from literature, however it is observed that the separation point predicted by Fluent is further downstream than that measured on the NDCT's. This might be due to the hyperbolic shape of the actual towers, a difference in the surface roughness, varying wind velocity during the experiments or it indicates that the Fluent model should be refined further.



**Figure 3-15 Comparison of rough circular cylinder pressure coefficient distribution from Fluent with experimental data from literature**



**(a) Vertical plane through the centre of the cylinder parallel to the free stream flow**



**(b) Vertical plane parallel to the freestream flow with  $J/D = 0.25$  from the centre**

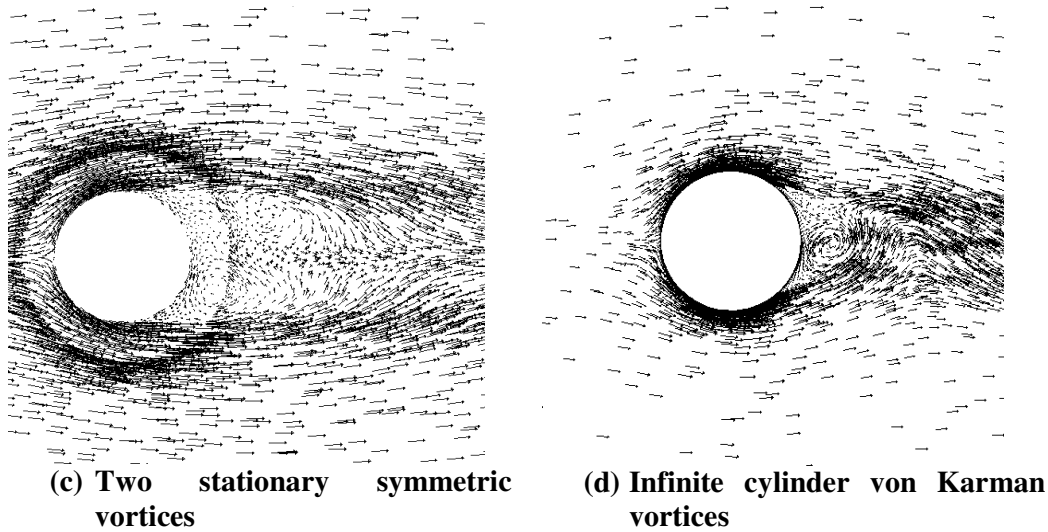


**Figure 3-16 Velocity vector plots at different planes for an infinite and finite cylinder**

Figure 3-16 illustrates the tip effect as described by Niemann and Hölcher (18). From Figure 3-16 (a) and (b) it is seen that the air flow over the top of the cylinder is sucked into the wake region due to the lower static pressure resulting in the two stationary vortices that form in this region as shown in Figure 3-16 (c). These are distinctly different from the oscillating Von Karman vortices that form during flow around an infinite cylinder as illustrated in Figure 3-16 (d).

### 3.4 Discussion

Through a sensitivity analysis, a Fluent model is developed to determine how accurately the pressure profile around a circular cylinder at Reynolds numbers in the trans-critical regime can be predicted. The model is solved using a double precision solver with the SIMPLE algorithm for the pressure-velocity coupling and second order discretization scheme for all the variables. The k- $\epsilon$  realizable turbulence model is identified as the most suitable due to decreased simulation time compared to other models. Grid independence could not be achieved due to limited computing resources available; however it is observed that the following are important when constructing a mesh:

- The boundary layer should be constructed using hexahedral elements and be extended at least a radial distance away from the cylinder of  $D/3$ .
- For improved accuracy in the wake of a cylinder the mesh elements should be constructed with  $Y = m$  and  $Z \geq 80$ .
- Increased turbulence intensity does not affect the pressure distribution around the cylinder, but does influence the stability of the boundary layer and decreases the Strouhal number.

Due to the lack of experimental data on smooth cylinders for a Reynolds number above  $10^6$  it is decided to model a rough surface ( $k_s/D = 1.5 \times 10^{-3}$ ) to determine how well the built-in modified law of the wall function in Fluent predicts the flow field. It is found that there is a substantial difference in the surface pressure field around the cylinder when compared to a smooth surface; however there is no significant change in Strouhal number with increasing surface roughness. It is observed that the average

surface pressure for the infinite rough cylinder predicts a lower pressure recovery than the experimental data obtained from literature for finite cylinders, which is attributed to the tip effect (18). To verify this statement, a three-dimensional model is constructed based on the principles obtained from the two-dimensional sensitivity analyses. The following is observed for the three dimensional case:

- There is a substantial difference in the surface pressure profiles around the cylinder compared to the two-dimensional case.
- There exists a span wise difference in the pressure profiles along the axis of the cylinder.
- The flow field around the cylinder is more stable.
- A lower drag coefficient is predicted due to an increased pressure recovery behind the cylinder.
- The increased pressure recovery of a finite cylinder compared to an infinite cylinder is due to the two stationary symmetrical vortices which form behind the cylinder.

The pressure profiles around the cylinder compare well with experimental data from literature. It is however observed that Fluent predicts a separation point further downstream than what is measured experimentally. This could be due to several factors which include but are not limited to:

- Difference in roughness height between the Fluent model and the experiment.
- Varying wind velocity during the experiments.
- Further grid refinement is needed.
- The modified law of the wall does not predict the shear stress next to the wall accurately.

## 4 Conclusion

This thesis investigate the capability of Fluent to model cooling tower inlet flow and flow around a cylinder, which are two important aspects when modelling the performance of natural draught cooling towers under cross-wind conditions.

### 4.1 Inlet loss and effective diameter study

The study of the inlet loss and effective diameter is initiated with a sensitivity analysis of the parameters that have an effect on the solution, which are: grid independence, grid elements, turbulence model, turbulence intensity, turbulent length scale and boundary layer parameter specification. From this investigation it is found that using the k- $\epsilon$  realizable model, tetrahedral elements with an inlet diameter to cell size ratio of 700 and a turbulence intensity of between 2% and 10 % results in the most accurate prediction of the inlet loss and effective diameter. The variation in the turbulence length scale and specifying no shear at the boundaries had insignificant influences on the solution and the latter reduces the necessity of creating a boundary layer that has  $30 \leq y^+ \leq 300$ , which reduces the complexity of designing the mesh.

The Fluent models are validated by experimental data obtained from a cooling tower sector model and it is established that the results compare well. The Fluent results did not compare well with literature available on this subject, since the literature used a cylindrical tower and an orthotropic packing, while this study employs a conical tower and an anisotropic packing. Orthotropic resistance is defined as a three-dimensional resistance with at least two orthogonal planes of symmetry where the resistance properties are independent of direction within each plane, while an anisotropic resistance is defined as a three-dimensional resistance without any planes of symmetry. Thus it is deemed necessary to study the effect of the different geometries on the inlet loss and effective diameter. It is found that for a conical tower the inlet loss is higher than for a cylindrical tower while the effective diameter is smaller. The increased inlet loss for conical towers is accredited to higher velocity gradients present in this geometry. With the knowledge that there is a difference in inlet loss and effective diameter between a cylindrical and conical tower, new empirical equations are developed with the aid of Fluent for conical towers with anisotropic packing.

Kröger (1) determined that the inlet loss can be reduced and the effective diameter increased by rounding of the lintel of a cooling tower whilst under construction. Unfortunately it is not possible to round the concrete lintel of a cooling tower which has already been constructed. Thus the inlet geometry must be changed by adding structures to it. Two methods were identified for this purpose, namely protruding platforms and rounded structures. Different configurations of these two structures are investigated and it was found that the inlet loss can be reduced by up to 42% when these structures are added to a tower. The best structure is the 0 m x 7.2 m platform, but it requires a larger amount of space than for the 3 m x 3 m platform and  $r_i/d_i = 0.025$ , which are equally good options. Observing the path line plot for the 3 m x 3 m platform, it is decided to investigate a 1 m x 1 m platform as well, which seems to be the most practical solution but does not give as good an improvement as the other geometries.

## 4.2 Flow around a circular cylinder

The study of the flow around a circular cylinder is initiated with a sensitivity analysis, which determines the influence of boundary layer creation, grid independence, turbulence model, surface roughness, turbulence intensity and turbulent length scale. From this investigation the following conclusions are drawn:

- The boundary layer must be created with hex elements and be extended at least a radial distance away from the cylinder wall of  $D/3$ .
- The  $k-\epsilon$  realizable should be used due to the consideration of processing time and accuracy.
- The refinement process downstream of the cylinder should be done using a grid with a minimum configuration of  $m-80$ .
- The turbulence parameters have an insignificant influence on the pressure profile around the surface of the cylinder, while the opposite is true for the frequency at which vortices are shed.
- Surface roughness has a profound influence on the frequency of vortex shedding, the velocity profiles in the wake and the pressure profiles around the cylinder and in the wake.

It is not possible to validate the Fluent model for flow around a smooth circular cylinder due to a lack of experimental data for the trans-critical regime. The results are compared to experimental data for the critical and super-critical regimes and it is observed that the increase in drag in the trans-critical regimen is due to the decrease in pressure recovery behind the cylinder. Fluent predicts an increasing pressure recovery behind the cylinder and thus a lower drag than the constant drag coefficient given by Figure 3-1 for the trans-critical regime above a  $Re$  of  $4 \times 10^6$ . The assumption is made that the results predicted by Fluent are accurate due to the accuracy of the Fluent model results by Alberti (17) and Catalano et al (14) compared to their experimental data.

The next step was to model a finite cylinder with a rough surface ( $k_s/D = 1.5 \times 10^{-3}$ ) in order to study three-dimensional effects, such as the tip effect mentioned by Niemann and Hölcher (18). The grid is designed applying the principles established for the two-dimensional infinite model. From the results of this model it is discovered that there is a span wise difference in the pressure profile. These results are then compared to experimental data measured on actual NDCT's. It is found that the separation point predicted by Fluent is further downstream compared to the experimental data. This might be due to several factors, which include the hyperbolic shape of the actual towers, a difference in the surface roughness, varying wind velocity during the experiments or indicates that the Fluent model must be further refined. The drag coefficient predicted for the finite case is lower than for the infinite case and can be attributed to the tip effect, which promotes pressure recovery downstream of the cylinder.

## 5 References

1. **Kröger, D.G.**, *Air-cooled Heat Exchangers and Cooling Towers: Thermal-flow Performance Evaluation and Design*, Penwell Corp., Tulsa, Oklahoma, 2004.
2. **De Villiers, E.**, *Losses in the inlet section of counterflow wet-cooling towers*, M.Sc.Eng Thesis, Department of Mechanical Engineering, University of Stellenbosch. Stellenbosch, 1998.
3. **Geldenhuis, J.D. and Kröger, D.G.**, *Aerodynamic Inlet Losses in Natural Draft Cooling Towers*, Proceedings of the 5th IAHR Cooling tower Workshop, Monterey, 1986.
4. **Terblanche, J.E. and Kröger, D.G.**, *Experimental evaluation of the aerodynamic inlet losses in cooling towers*,. South African Institute of Mechanical Engineers R&D Journal, Vol. 10, pp. 41-44, 1994.
5. **de Villiers, E.**, *Losses in the inlet section of counterflow wet-cooling towers*, PhD Thesis, Department of Mechanical engineering, University of Stellenbosch, Stellenbosch, 1998.
6. **Geldenhuis, J.D.**, *Ontwerpsfaktore by natuurlike konveksie droë koeltorings*, MSc Thesis, Departement van Meganiese Ingenieurswese, University of Stellenbosch, Stellenbosch, 1987.
7. **White, F.W.**, *Fluid Mechanics, Fifth edition*. New York : McGraw-Hill Education, 2005.
8. **Oosthuizen, P.C. and Kröger, D.G.**, *Performance characteristics of hybrid cooling towers*, MSc.Eng Thesis, Mechanical Engineering, University of Stellenbosch. Stellenbosch, 1995.
9. **Simmons, L.F.G.**, *Measurements of the aerodynamic forces on porous screens*, R & M, 2276, 1945.
10. **Weighardt, K.E.G.**, *On the resistance of screens*. The Aeronautical Quarterly, Vol. 4, pp. 186-192, February 1953.
11. **Derbunovich, G.Q., et. al.**, *Optimum wire screens for control of turbulence in wind tunnels*, Fluid Mechanics - Soviet Research, Vol. 10, Part 5, pp. 136-147, September-October 1981.
12. **Cornell, W.G.**, *Losses in flow normal to plane screens*, Transactions of ASME, Vol. 80, pp. 791-799, May 1985.
13. **Fluent Inc.** *Fluent 6.3 Documentation*. 2006-10-12.
14. **Catalano, P, Wang, M., Iaccarino, G. and Moin, P.**, *Numerical simulation of the flow around a circular cylinder at high Reynolds numbers*. , International Journal of Heat and Fluid Flow, Vol. 24, pp. 463-469, 23 March 2003.
15. **Zdravkovich, M.M.**, *Flow around circular cylinders*, Oxford University Press,. Vol. 1, 1997.
16. **Warschauer, K.A., and Leene, J.A.**, *Experiments on mean and fluctuating pressures of circular cylinders at cross flow at very high Reynolds numbers*, Proceedings of the International Conference on Wind Effects on Buildings and Structures, Tokyo, Japan, pp. 305-315.
17. **Alberti, L.**, *Flow around cylindrical towers: The stabilising role of vertical ribs*, M.Sc Thesis, Civil Engineering, University of Stellenbosch, University Press, Stellenbosch, South Africa, 2006.
18. **Niemann, H.J., and Hölscher, N.**, *A review of recent experiments on the flow past circular cylinders*, Journal of Wind Engineering and Industrial Aerodynamics, Vol. 37, pp. 197-209, March 1990.



19. **Schewe, G.**, *On the force fluctuations acting on a circular cylinder in cross flow from subcritical up to transcritical Reynolds numbers*, Journal of Fluid Mechanics, Vol. 133, pp. 265-285.
20. **Ribeiro, J.L.D.**, *Effect of surface roughness on the two dimensional flow past circular cylinders II: Fluctuating forces and pressures*, Journal of Wind Engineering and industrial Aerodynamics, Vol. 37, pp. 311-326, 1991.
21. **Ribeiro, J.L.D.**, *Effects of surface roughness on the two-dimensional flow past circular cylinders I: Mean forces and pressures*, Journal of Wind Engineering and Industrial Aerodynamics, Vol. 37, pp. 300-310, 1991.
22. **Ayoub, A., and Karamcheti, K.** *An experimental on the flow past a finite circular cylinder at high subcritical and supercritical Reynolds number*, Journal of Fluid Mechanics, Vol. 118, pp. 1-26, 1982
23. **Farivar, D.J.**, *Turbulent uniform flow around cylinders of finite length*. AIAA Journal, Vol. 19, pp. 275-281, 1981.
24. **Sakamoto, H., and Arie, M.** , *Vortex shedding from a rectangular prism and a circular cylinder placed vertically in a turbulent boundary layer*, J. Fluid Mech., Vol. 126, pp. 147-165, 1983.
25. **Ruscheweyh, H.** , *Full-scale measurements on a large NDCT*, Australia , Proceedings of the 6th international conference on wind engineering, 1983
26. **Blanquet, J.C., Goldwirth, F., and Manas, B.**, *Wind effects on the aerodynamic optimization of a NDCT*, Proceedings of the 5th IAHR cooling tower Workshop, Monterey, 1986.
27. **Pierce, D.J.**, *Evaluation and Performance Prediction of Cooling Tower Rain Zone*, MSc.Eng Thesis, University of Stellenbosch, Stellenbosch, South Africa, 2007.
28. **Dreyer, A.A.**, *Modelling of Cooling Tower Splash packs*, Ph.D. Thesis, Department of Mechanical Engineering, University of Stellenbosch, Stellenbosch, 1994.
29. **Ra'fat, A.**, *Development of Performance-Improving Structures for Power Station Cooling Towers*, Ph.D. Thesis, The School of Mechanical and Manufacturing Engineering, University of New South Wales, Sydney, Australia, 2004.
30. **Rossouw, A.**, *Optimization Of Natural Draught Cooling Tower Performance: Minimizing Tower Inlet Loss and Increasing Effective Diameter*, B.Eng final year project, Department of Mechanical Engineering, University Of Stellenbosch, Stellenbosch, South Africa, 2006.
31. **Viljoen, D.**, *Evaluation and Performance Prediction of Cooling Tower Spray Zones*, MSc.Eng Thesis, Department of Mechanical Engineering, Stellenbosch, University of Stellenbosch, South Africa, 2006.
32. **De Villiers, E.**, *The Analysis of Crosswind Effects On Solar Chimney Performance*, B.Eng final year project Mechanical Engineering, University of Stellenbosch, University Press, Stellenbosch, South Africa, 2004.
33. **Schlichting, H.**, *Boundary-Layer Theory*, translator: J Kestin, Sixth Edition, McGraw-Hill, Inc, 1968.
34. **Osborn, C.H.**, *Wind loading on chimneys*, B.E.Sc final year project Faculty of Engineering science, University of Western Ontario. London, Ontario, Canada, 1981.
35. **Lowe, H.J., and Christie, D.G.**, *Heat transfer and Pressure Drop Data on Cooling Tower Packings and Model Studies of the Resistance of Natural*

- Draught Towers to Airflow*. Proc. of the Int. Heat Transfer Conf, Part V Colorado, USA, 1961.
36. **Gunn, R., and Kinzer, G.D.**, *The Terminal Velocity of Fall For Water Droplets In Stagnant Air*, Journal of Meteorology, Vol. 6, pp. 243-248, 1949.
  37. **Ranz, W.E., and Marchall Jr., W.R.**, *Evaporation from Drops, Part I.*, Chemical Engineering Progress, Vol. 48, No 2, pp. 141-146. March 1952.
  38. **Turton, R., and Levenspiel, O.**, *Short Note on the Drag Correlation for Spheres*, Powder Technology, Vol. 47, pp. 83 – 86, 1986.
  39. **Du Preez, A.F., and Kröger, D.G.**, *The Influence of Buoyant Plume on the Performance of a Natural Draft Cooling Tower*, 9th IAHR Cooling Tower and Spraying Pond Symposium, Brussels, 1994.
  40. **Hosoz, M., Ertunc, H.M., and Bulgurcu, H.**, *Performance Prediction of a Cooling Tower Using Artificial Neural Network*, Energy Conversion and Management, Vol. 48, pp. 1349-1359, 2007.
  41. **Walker, W.H., et. al.** *Principles of Chemical Engineering*, 3rd edition., McGraw-Hill Inc., 1923.
  42. **Merkel, F.**, *Verdunstungshuhln*, Zeitschrift des Vereines Deutscher Ingenieure (VDI), Vol. 70, pp. 123-128, 1925.
  43. **Qureshi, Bilal A. and Zubair, Syed M.**, *A Complete Model of Wet Cooling Towers with Fouling in Fills.* , Applied Thermal Engineering, Vol. 26, pp. 1982-1989, 2006.
  44. **Kloppers, J.C. and Kröger, D.G.**, *A Critical Investigation Into the Heat and Mass Transer Analysis of Counterflow Wet-Cooling Tower.* , International Journal of Heat and mass Transfer, Vol. 48, pp. 765-777, 2005.
  45. **Kloppers, J.C. and Kröger, D.G.**, *The Lewis Factor and its Influence on the Performance Prediction of Wet-Cooling Towers.* ,International Journal of Thermal Sciences, Vol. 44, pp. 879-884, 2005.
  46. **Kloppers, J.C and Kröger, D.G.**, *Cooling Tower Performance: A Critical Evaluation of the Merkel Assumptions* , R & D Journal, Vol. 20, No 1, pp. 24-29, 2004.
  47. **4485, British Standard**, Water cooling towers, Part 2: methods for performrance testing, 1988.
  48. **Fisenko, S.P., Brin, A.A. and Petruchik, A.I.**, *Evaporative cooling of water in a mechanical draft cooling tower*, International Journal of Heat and Mass Transfer, Vol. 47, pp. 165-177, 2004.
  49. **Qureshi, B.A. and Zubair, S.M.**, *Second-law-based performance evaluation of cooling tower and evaporative heat exchangers*, International Journal of Thermal Sciences, Vol. 46, pp. 188-198, 2007.
  50. **Smrekar, J., Oman, J., and Sirok, B.**, *Improving the efficiency of natural draft cooling towers*, Energy Conversion and Management, Vol. 47, pp. 1086-1100, 2006.
  51. **Du Preez, F., and Kröger, D.G.**, *Experimental Evaluation of Aerodynamic Inlet Losses in Natural Draft cooling Towers*, Proceedings of the 6th IAHR Cooling Tower Workshop, Pisa, Italy, 1988.
  52. **Sakamoto, H. and Arie, M.**, *Vortex shedding from a rectangular prism and a circular cylinder placed vertical in a turbulent boundary layer*, Journal of Fluid Mechanics, Vol. 133, pp. 147-165, 1983.
  53. **Achenbach, E.**, *Distribution of local pressure and skin friction around a circular cylinder in cross-flow up to  $Re = 5 \times 10^6$* , Journal of Fluid Mechanics, Vol. 34, pp. 625-639.

## Appendix A: Thermo Physical Properties of Fluids

### *Properties of Air for a Temperature range of 220K to 380K*

Density:

$$\rho_a = p_a / (287.08 T), \text{ kg/m}^3 \quad (\text{A-1})$$

Specific heat:

$$c_{pa} = 1.045359 \cdot 10^3 - 3.161783 \cdot 10^{-1} T + 7.083814 \cdot 10^{-4} T^2 - 2.705209 \cdot 10^{-7} T^3, \text{ J/kgK} \quad (\text{A-2})$$

Dynamic viscosity:

$$\mu_a = 2.287973 \cdot 10^{-6} + 6.259793 \cdot 10^{-8} T - 3.131956 \cdot 10^{-11} T^2 + 8.15038 \cdot 10^{-15} T^3, \text{ kg/sm} \quad (\text{A-3})$$

Thermal conductivity:

$$k_a = -4.937787 \cdot 10^{-4} + 1.018087 \cdot 10^{-4} T - 4.627937 \cdot 10^{-8} T^2 + 1.250603 \cdot 10^{-11} T^3, \text{ W/mK} \quad (\text{A-4})$$

### *Properties of Saturated water vapour from 273.15K to 380K*

Vapour pressure:

$$p_v = 10^z, \text{ N/m}^2 \quad (\text{A-5})$$

where

$$z = 10.79586(1 - 273.16/T) + 5.02808 \log_{10}(273.16/T) + 1.50474 \cdot 10^{-4} [1 - 10^{-8.29692\{(273.16/T)-1\}}] + 4.2873 \cdot 10^{-4} [10^{4.76955(1-273.15/T)} - 1] + 2786118312 \quad (\text{A-6})$$

Specific heat:

$$c_{pv} = 1.3605 \cdot 10^3 + 2.31334 T - 2.46784 \cdot 10^{-10} T^5 + 5.91332 \cdot 10^{-13} T^6, \text{ kg/ms} \quad (\text{A-7})$$

Dynamic viscosity:

$$\mu_v = 2.562435 \cdot 10^{-6} + 1.816683 \cdot 10^{-8} T + 2.579066 \cdot 10^{-11} T^2 - 1.067299 \cdot 10^{-4} T^3, \text{ kg/ms} \quad (\text{A-8})$$

Thermal conductivity:

$$k_v = 1.3046 \cdot 10^{-2} - 3.756191 \cdot 10^{-5} T + 2.217964 \cdot 10^{-7} T^2 - 1.111562 \cdot 10^{-10} T^3, \text{ W/mK} \quad (\text{A-9})$$

Vapour density:

$$\rho_v = -4.062329056 + 0.10277044T - 9.76300388 \cdot 10^{-4} T^2 + 4.475240795 \cdot 10^{-6} T^3 - 1.004596894 \cdot 10^{-8} T^4 + 8.9154895 \cdot 10^{-12} T^5, \text{ kg/m}^3 \quad (\text{A-10})$$

**Properties of mixtures of air and water vapour**

Density:

$$\rho_{av} = (1 + w)[1 - w/(w + 0.62198)] p_{abs}/(287.08T), \text{ kg air - vapour /m}^3 \quad (\text{A-11})$$

Specific heat:

$$c_{pav} = (c_{pa} + wc_{pv})/(1 + w), \text{ J/K kg air - vapour} \quad (\text{A-12})$$

Or the specific heat of the air-vapour mixture per unit mass of dry air:

$$c_{pma} = (c_{pa} + wc_{pv}), \text{ J/K kg dry air} \quad (\text{A-13})$$

Dynamic viscosity:

$$\mu_{av} = (X_a \mu_a M_a^{0.5} + X_v \mu_v M_v^{0.5})/(X_a M_a^{0.5} + X_v M_v^{0.5}), \text{ kg/ms} \quad (\text{A-14})$$

where  $M_a = 28.97 \text{ kg/mole}$ ,  $M_v = 18.016 \text{ kg/mole}$ ,  $X_a = 1/(1+1.608w)$  and  $X_v = w/(w+0.622)$

Thermal conductivity:

$$k_{av} = (X_a k_a M_a^{0.33} + X_v k_v M_v^{0.33})/(X_a M_a^{0.33} + X_v M_v^{0.33}), \text{ W/mK} \quad (\text{A-15})$$

Humidity ratio:

$$w = \left( \frac{2501.6 - 2.3263(T_{wb} - 273.15)}{2501.6 + 1.8577(T - 273.15) - 4.184(T_{wb} - 273.15)} \right) \times \left( \frac{0.62509 p_{vwb}}{p_{abs} - 1.005 p_{vwb}} \right) - \left( \frac{(T - T_{wb})}{2501.6 + 1.8577(T - 273.15) - 4.184(T_{wb} - 273.15)} \right), \text{ kg} \\ \text{/kg of dry air} \quad (\text{A-16})$$

Enthalpy:

$$i_{av} = [c_{pa}(T - 273.15) + w\{i_{fgwo} + c_{pv}(T - 273.15)\}]/(1 + w), \text{ J} \\ \text{/kg air - vapour} \quad (\text{A-17})$$

Or the enthalpy of the air-vapour mixture per unit mass of dry air:

$$i_{ma} = c_{pa}(T - 273.15) + w\{i_{fgwo} + c_{pv}(T - 273.15)\}, \text{ J/kg dry - air} \quad (\text{A-18})$$

where the specific heat values are evaluated at  $(T+273.15)/2$  and the latent heat  $i_{fgwo}$ , is evaluated at 273.15K according to equation A-21,  $i_{fgwo} = 2.5016 \times 10^6 \text{ J/kg}$

***Properties of saturated water liquid from 273.15 K to 380 K***

Density:

$$\rho_w = (1.49343 \cdot 10^{-3} - 3.7164 \cdot 10^{-6}T + 7.09782 \cdot 10^{-9}T^2 - 1.90321 \cdot 10^{-12}T^3)^{-1}, \text{ kg/m}^3 \quad (\text{A-19})$$

Specific heat:

$$c_{pw} = 8.15599 \cdot 10^3 - 28.0627T + 5.11283 \cdot 10^{-2}T^2 - 2.17852 \cdot 10^{-5}T^3, \text{ J/K kg} \quad (\text{A-20})$$

Dynamic viscosity:

$$\mu_w = 2.414 \cdot 10^{-5} \cdot 10^{247.8/(T-140)}, \text{ kg/ms} \quad (\text{A-21})$$

Thermal Conductivity:

$$k_w = -6.14255 \cdot 10^{-1} + 6.9962 \cdot 10^{-3}T - 1.01075 \cdot 10^{-5}T^2 + 4.74737 \cdot 10^{-8}T^3, \text{ W/mK} \quad (\text{A-22})$$

Latent heat of vaporization:

$$i_{fgw} = 3.4831814 \cdot 10^6 - 5.8627703 \cdot 10^3T + 12.139568T^2 - 1.40290431 \cdot 10^{-2}T^3, \text{ J/kg} \quad (\text{A-23})$$

Critical pressure:

$$p_{wc} = 22.09 \cdot 10^6, \text{ N/m}^2 \quad (\text{A-24})$$

Surface tension:

$$\sigma_w = 5.148103 \cdot 10^{-2} + 3.998714 \cdot 10^{-4}T - 1.4721869 \cdot 10^{-6}T^2 + 1.21405335 \cdot 10^{-9}T^3, \text{ N/m} \quad (\text{A-25})$$

## Appendix B: Experimental work

### B.1 Wind tunnel

#### B.1.1 Description

A wind tunnel at the University of Stellenbosch is used for both the packaging and tower section experiments. The tunnel is an induced draught tunnel shown schematically in Figure B-1. A radial fan at position 7 draws the air through the tunnel. At position 1 the air is passed through a set of mixers and subsequently flows through a venturi at position 2, where a sampling tube is located. The flow is directed through a set of nozzles at position 4 that is set between two perforated plates at positions 3 and 6. There are five nozzles at 4 and each can be opened in turn or in combinations to improve the air flow measurements for different air flow rates. The mass flow is varied using a frequency inverter for the motor that drives the fan.

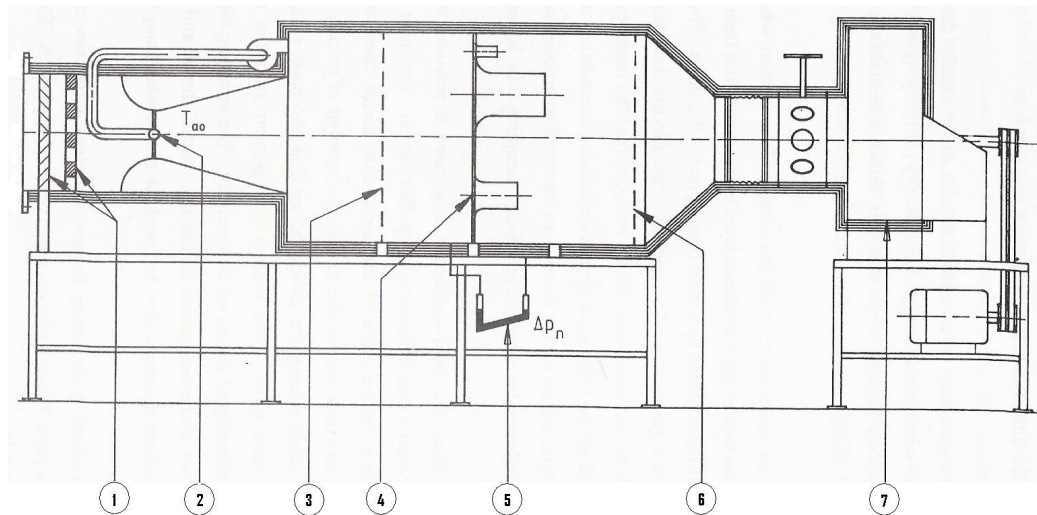


**Figure B-1 Schematic of wind tunnel used in experiments courtesy of Kröger (1)**

The tunnel was initially designed for the testing of finned tube bundle heat exchangers. The air discharged from the heat exchangers may or may not have a non-uniform distribution. Thus the function of the mixers is to mix the air in order to enable a mean temperature measurement of the exiting air. The result is very non-uniform flow. Thus the venturi is incorporated to minimize the non-uniformity of the air. The sampling tube at position 2 can withdraw air from numerous points in the throat of the venturi. The sample is then moved to a convenient location to measure the mean dry- and wet-bulb temperatures.

#### B.1.2 Measurement of mass flow rate

The wind tunnel is used to induce and measure the air flow through the test section installed at the air inlet of the tunnel. To determine the air mass flow, the pressure drop  $\Delta p_n$  and the pressure upstream of the nozzles, are measured with a pressure

transducer. The pressure transducer is calibrated using a Betz water manometer by connecting the negative connections to each other and creating a vacuum in this connection. The vacuum is lowered stepwise until atmospheric pressure is reached while the reading on the transducer and Betz is recorded at each step. A linear correlation is developed to convert the reading from the transducer to that given by the Betz. From the measured data the following set of equations can be used to determine the mass flow rate (1).

$$m = C_n \phi_g Y A_n (2\rho_n \Delta p_n)^{0.5} \quad (\text{B-1})$$

The nozzle coefficient of discharge,  $C_n$ , is a function of the nozzle Reynolds number. For

$30,000 < Re_n < 100,000$ :

$$C_n = 0.954803 + 6.37817 \cdot 10^{-7} Re_n - 4.65394 \cdot 10^{-12} Re_n^2 + 1.33514 \cdot 10^{-17} Re_n^3 \quad (\text{B-2a})$$

For  $100,000 < Re_n < 350,000$ :

$$C_n = 0.9758 + 1.08 \cdot 10^{-7} Re_n - 1.6 \cdot 10^{-13} Re_n^2 \quad (\text{B-2b})$$

And for  $Re_n > 350,000$ :

$$C_n = 0.994 \quad (\text{B-2c})$$

The gas expansion factor  $\phi_g$  may be approximated by the following relation:

$$\phi_g = 1 - 3\Delta p_n / (4p_{up} c_p / c_v) \quad (\text{B-3})$$

where  $c_p/c_v = 1.4$  for air and  $p_{up}$  is the upstream pressure.

For a compressible fluid, it can be shown that the approach velocity factor is approximately:

$$Y = 1 + 0.5(A_n/A_{tus})^2 + 2(A_n/A_{tus})^2 \Delta p_n / (p_{up} c_p / c_v) \quad (\text{B-4})$$

where  $A_{tus} = 1.44 \text{ m}^2$  and  $p_{up}$  is the pressure in front of the nozzle.

Equation B-4 neglects thermal expansion or contraction of the nozzle. If more than one of the nozzles are open, then the equations need to be applied for each nozzle. The two mass flows are then added together to determine the total mass flow of air through the tunnel. The fan limits the total system pressure loss to 1.5kPa, which limited the experimental total loss coefficient that could be investigated with the wind tunnel.

## B.2 Static pressure probe

To measure the pressure profile behind the packing of the cooling tower, a static pressure probe is manufactured and calibrated.

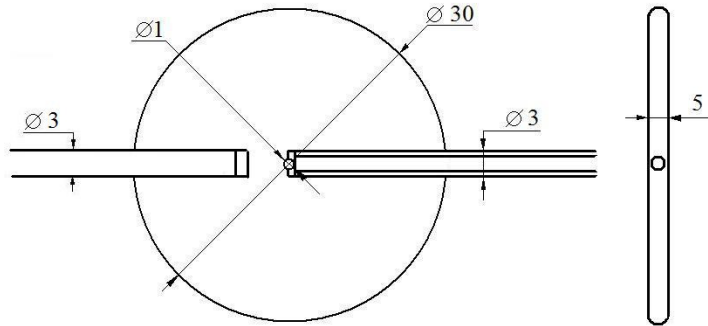


**Figure B-2 Dimensions of the static pressure probe**

Figure B-2 displays the dimensions of the static probe used inside the CTSM. A normal Pitot tube is sensitive to the direction of flow and thus the new probe needs to compensate for this. The resulting probe is machined from solid brass and given a disk shape. Two 3mm holes are drilled into the probe as indicated to house the solid rod on the one side and the hollow tube on the other. The solid rod is used for support and the hollow tube allows the transfer of the static pressure from the 1mm tapped hole in the centre to a Betz manometer.

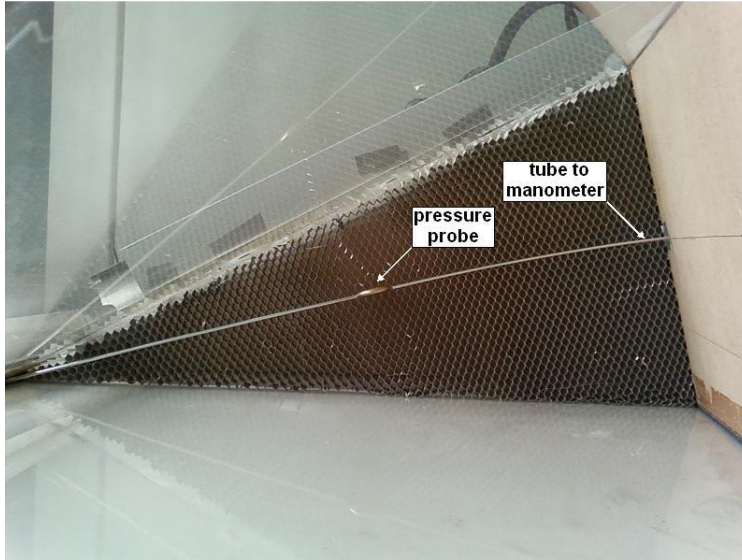


**Figure B-3 Pressure probe position in the CTSM**

Figure B-3 displays how the probe is inserted into the CTSM along a centre line behind the packing. The hollow tube is inserted through the wall of the tower and is connected to a Betz manometer. With this configuration it is possible to move the probe along the radius of the tower to measure the pressure distribution behind the packing.



**Table B-1 Data for pressure calibration of the probe**

Pitot tube pressure (Pa)	Disk probe pressure (Pa)
0	0
20.601	25.506
89.271	103.986
206.01	217.782
366.894	407.115
559.17	635.688

The probe is calibrated in a wind tunnel using a Pitot tube. Static pressure measurements are taken at different air speeds and the results are shown in Table B-1. The data is correlated to yield the following calibration curve:

$$p_{true} = 0.8861p_{probe} + 1.688 \quad (B-5)$$

**Table B-2 Data for probe sensitivity to angle of attack**

Angle	Test run 1 (Pa)	Test run 2 (Pa)
-30	36.297	37.278
-20	36.297	37.278
-10	38.259	38.259
-5	34.335	35.316
0	25.506	25.506
5	27.468	25.506
10	29.43	29.43
20	29.43	31.392
30	26.487	29.43

Table B-2 presents the data for the probe's sensitivity test to the direction of the flow field. This is achieved by varying the angle of attack in a range of -30° to 30° in increments of 5°. There is a clear difference in the pressure measured between the positive and negative angles of attack. Upon closer inspection it is observed that one of the holes in the probe is larger than the others, which explains the deviation. From this study it is concluded that the probe's angle of attack must be set as close as possible to zero during the measurement process and that if there is deflection, it must be in the direction of the smaller hole on the probe.

## Appendix C: Packing Experiment

### C.1 Sample calculation for the packing

The following parameters are measured during the experiment with reference to Figure 2-2 and Figure B-1:

Temperature of the environment:	$T_a = 295.15 \text{ K}$
Pressure of the environment:	$P_a = 101140 \text{ Pa}$
Pressure measured across nozzle:	$\Delta P_n = 506.56 \text{ Pa}$
Pressure upstream of the nozzle:	$P_{up} = 99600.15 \text{ Pa}$
Pressure measured across the test section:	$\Delta P_s = 1198.52 \text{ Pa}$
Number of nozzles used:	$n = 1$

The structural dimensions that stay constant are:

Diameter of nozzle 4:	$d_{n4} = 0.2009 \text{ m}$
Diameter of nozzle 5:	$d_{n5} = 0.2509 \text{ m}$
Diameter of the test section:	$d_{cyl} = 0.3 \text{ m}$
Area of section in front of nozzles:	$A_{tus} = 1.44 \text{ m}^2$
Gas constant of air:	$R = 287.07 \text{ J/(kg}\cdot\text{K)}$
Ratio of specific heats for air:	$k=1.4$

Firstly the properties of air need to be determined. Using equations (A-1) and (A-3) we find that:

$$\rho_a = 1.194 \text{ kg/m}^3$$
$$\mu_a = 1.824 \times 10^{-5} \frac{\text{kg}}{\text{m} \cdot \text{s}}$$

Now the determining of the mass flow rate is an iterative procedure and is started by assuming an initial mass flow rate:

$$m = 1.093 \text{ kg/s}$$

The nozzle Reynolds number is now calculated to determine which of equations (B-2a) to (B-2c) needs to be used.

$$Re_n = \frac{m \cdot d_{n4}}{\mu_a \cdot A_{n4}} = \frac{1.093 \cdot 0.2009}{1.824 \times 10^{-5} \cdot 0.006368} = 3.797 \times 10^5$$

This value of the nozzle Reynolds number leads to the use of equation (B-2c) which is:

$$C_n = 0.944$$

Now calculating the values of equation (B-3) and (B-4) we get:

$$Y = 1 + 0.5 \left( \frac{0.006368}{1.44} \right)^2 + 2 \left( \frac{0.006368}{1.44} \right)^2 \left( \frac{506.56}{99600.15 \cdot 1.4} \right) \approx 1$$

$$\varphi_g = 1 - \frac{3 \cdot 506.56}{4 \cdot 99600.15 \cdot 1.4} = 1.003$$

Substituting the above into equation (B-1) we find:

$$m = 0.944 \cdot 1.003 \cdot 1 \cdot 0.006368 \cdot \sqrt{2 \cdot 1.194 \cdot 506.6} = 1.093 \text{ kg/s}$$

With this mass flow rate the velocity through the cylinder can be calculated;

$$v_{cyl} = \frac{m}{(\rho_a \cdot A_{cyl})} = \frac{4 \cdot 1.093}{1.194 \cdot \pi \cdot 0.3^2} = 12.954 \text{ m/s}$$

Now the loss coefficient can be determined from the following:

$$K_s = \frac{2 \cdot \Delta P_s}{\rho_a \cdot v_{cyl}^2} = \frac{2 \cdot 1198.52}{1.194 \cdot 167.81} = 11.966$$

If more than one nozzle is used then the mass flow rate is calculated for both nozzles and the individual results are added together for the total mass flow rate.

## C.2 Experimental data of the fill experiment

Two nozzles were used to increase the mass flow rate at different stages in the experiment.

### First experimental run:

**Table C-1 Fill experimental data run 1: Honeycomb**

Atmospheric temperature: 297.65 K

Atmospheric pressure: 100440 Pa

n	$\Delta p_s$	$\Delta p_n$	$\Delta p_{up}$	$K_s$
1	0.27	48.32	30.77	0.03
1	4.28	112.94	68.91	0.19
1	9.29	193.21	134.35	0.24
1	14.30	302.08	208.38	0.24
1	21.31	436.46	296.05	0.25
1	29.33	592.69	393.38	0.28
1	39.34	775.16	509.56	0.29
1	47.35	983.02	641.79	0.27
1	58.37	1208.96	775.16	0.27

**Table C-2 Fill experimental data run 1: One layer of mesh**

Atmospheric temperature: 297.65 K

Atmospheric pressure: 100440 Pa

n	$\Delta p_s$	$\Delta p_n$	$\Delta p_{up}$	$K_s$
1	40.34	22.49	57.59	9.24
1	85.40	60.68	117.02	7.18
1	149.43	108.85	215.45	6.97
1	220.00	184.10	327.19	6.05
1	309.43	274.93	462.50	5.68
1	371.45	365.31	629.76	5.14
1	559.60	458.49	837.39	6.17
1	704.81	556.63	1062.37	7.10
1	860.07	704.94	1299.26	6.86

**Table C-3 Fill experimental data run 1: One layer of mesh and Honeycomb**

Atmospheric temperature: 296.65 K

Atmospheric pressure: 100360 Pa

n	$\Delta p_s$	$\Delta p_n$	$\Delta p_{up}$	$K_s$
1	40.34	24.56	57.59	8.47
1	89.40	61.71	124.16	7.41
1	155.43	114.98	215.45	6.88
1	232.43	183.09	326.18	6.44
1	326.43	268.89	471.51	6.15
1	434.48	366.31	626.75	6.01
1	555.59	478.52	817.32	5.89
1	689.79	608.72	1018.18	6.38
1	836.03	767.14	1241.08	6.14

**Table C-4 Fill experimental data run 1: One layer of mesh and Honeycomb**

Atmospheric temperature: 296.65 K

Atmospheric pressure: 100360 Pa

n	$\Delta p_s$	$\Delta p_n$	$\Delta p_{up}$	$K_s$
1	38.34	22.49	57.59	8.78
1	89.40	60.68	127.22	7.52
1	153.43	112.94	216.46	6.90
1	230.43	180.05	326.18	6.48
1	319.43	272.91	467.51	5.91
1	425.47	373.33	624.75	5.76
1	550.59	485.53	805.27	6.36
1	685.78	626.75	107.83	6.14
1	828.02	783.19	1228.03	5.95

**Table C-5 Fill experimental data run 1: Two layers of mesh**

Atmospheric temperature: 296.65 K

Atmospheric pressure: 100360 Pa

n	$\Delta p_s$	$\Delta p_n$	$\Delta p_{up}$	$K_s$
1	51.36	14.20	67.88	18.74
1	118.42	38.01	150.62	15.96
1	210.43	75.07	257.81	14.28
1	320.43	129.26	392.38	12.58
1	447.49	188.15	558.63	12.03
1	604.66	266.87	745.06	11.44
1	772.93	344.25	970.96	11.34
1	972.25	437.46	1219.00	11.23
1	1210.54	519.58	1508.78	13.07

**Second Experimental Run:**

**Table C-6 Fill experimental data run 2: One layer of mesh**

Atmospheric temperature: 295.15 K

Atmospheric pressure: 100930 Pa

n	$\Delta p_s$	$\Delta p_n$	$\Delta p_{up}$	$K_s$
1	38.34	21.45	55.54	9.20
1	84.39	62.74	119.06	6.86
1	146.43	117.02	212.42	6.35
1	221.43	187.14	325.18	5.99
1	313.43	276.94	460.50	5.72
1	373.45	374.34	625.75	5.04
1	555.59	463.50	828.36	6.06
1	712.82	552.63	1072.41	7.24
1	865.08	699.93	1309.30	6.95
2	981.27	131.29	1482.73	5.77
2	1205.53	164.84	1819.75	5.64

**Table C-7 Fill experimental data run 2: One layer of mesh with Honeycomb**

Atmospheric temperature: 295.15 K

Atmospheric pressure: 100930 Pa

n	$\Delta p_s$	$\Delta p_n$	$\Delta p_{up}$	$K_s$
1	40.34	24.56	55.54	8.45
1	88.40	61.71	124.16	7.31
1	151.43	116.00	215.45	6.63
1	229.43	185.11	327.19	6.27
1	325.43	271.91	468.51	6.04
1	430.48	374.34	624.75	5.81
1	552.59	490.54	805.27	6.32
1	685.78	624.75	1009.13	6.16
1	832.03	772.15	1232.05	6.06
2	1004.30	111.92	1494.75	6.93
2	1228.55	139.44	1831.81	6.80

**Table C-8 Fill experimental data run 2: One layer of mesh with honeycomb**  
 Atmospheric temperature: 295.15 K  
 Atmospheric pressure: 100930 Pa

n	$\Delta p_s$	$\Delta p_n$	$\Delta p_{up}$	$K_s$
1	40.34	24.56	56.57	8.39
1	87.40	61.71	124.16	7.23
1	150.43	116.00	215.45	6.58
1	227.43	183.09	329.19	6.28
1	320.43	268.89	465.50	6.02
1	427.47	371.33	622.75	5.81
1	546.58	488.54	807.28	5.66
1	681.77	630.76	1009.13	5.47
1	827.02	778.17	1231.04	5.39
2	1010.31	120.08	1502.77	6.50
2	1225.55	151.64	1830.80	6.23

**Table C-9 Fill experimental data run 2: Two layers of mesh with honeycomb**  
 Atmospheric temperature: 295.15 K  
 Atmospheric pressure: 101140 Pa

n	$\Delta p_s$	$\Delta p_n$	$\Delta p_{up}$	$K_s$
1	53.36	15.23	65.82	18.00
1	119.42	40.07	147.57	15.26
1	207.43	78.15	255.80	13.52
1	318.43	127.22	390.37	12.70
1	450.49	189.16	555.63	12.05
1	601.65	264.86	747.07	11.47
1	772.93	346.25	967.95	11.27
1	975.26	435.46	1221.01	11.32
1	1204.53	523.58	1507.78	11.64
2	1261.59	69.93	1575.93	13.99
2	1545.93	86.35	1934.46	13.86

### **Third Experimental Run:**

**Table C-10 Fill experimental data run 3: Two layers of mesh with honeycomb**  
 Atmospheric Temperature: 297.65 K  
 Atmospheric Pressure: 100440 Pa

n	$\Delta p_s$	$\Delta p_n$	$\Delta p_{up}$	$K_s$
1	54.36	16.27	68.91	17.23
1	119.42	42.13	148.59	14.47
1	202.43	78.15	256.81	13.16
1	309.43	131.29	390.37	11.93
1	438.48	195.23	552.63	11.33
1	587.63	266.87	744.06	11.10
1	763.91	347.26	970.96	11.08
1	970.25	426.44	1239.07	11.47
1	1198.52	506.56	1539.85	13.24
2	1245.57	74.04	1578.94	13.02
2	1531.91	94.54	1937.49	12.51

## Appendix D: Sector model test data

### D.1 Sample Calculation for CTSM

The data is collected along the radius of the sector model as shown in Figure D-1. At specified distances from the corner, measurements are taken with the aid of the probe. These are recorded for further analysis.

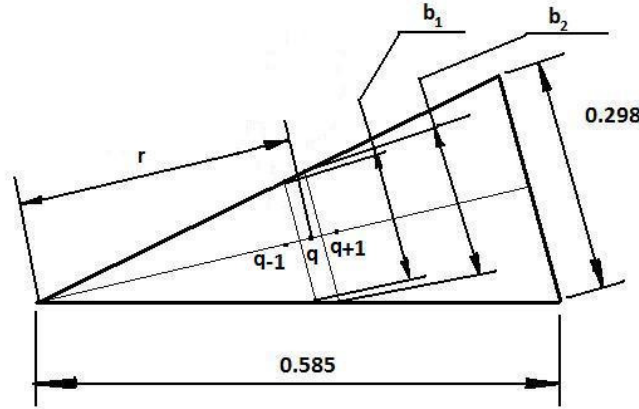


**Figure D-1 Illustration of Measurement Technique**

The area around the measurement point is determined as follows:

$$h_1 = \frac{r_q + r_{q-1}}{2} \quad (D-1)$$

$$h_2 = \frac{r_{q+1} + r_q}{2} \quad (D-2)$$

$$b_1 = 2 h_1 \tan \frac{\theta}{2} \quad (D-3)$$

$$b_2 = 2 h_2 \tan \frac{\theta}{2} \quad (D-4)$$

$$A_q = \left( \frac{b_2 + b_1}{2} \right) (h_2 - h_1) \quad (D-5)$$

The sample calculation is done using the data of Table D-1 and Table D-2. Implementing equation (B-1) to (B-4) the mass flow rate is determined as;

$$m = 0.77946 \text{ kg/s}$$

The inlet area of the tower model and the density are needed to determine the average inlet velocity. The area of a triangle is:

$$A_i = 0.5bh = 0.5 \times 0.305 \times 0.56831 = 0.086917 \text{ m}^2$$

The density of air according to equation (A-1) is:

$$\rho = \frac{p}{287.07T} = \frac{100600}{287.07 \times 292.35} = 1.1986 \frac{kg}{m^3}$$

Thus the inlet velocity can be calculated using equation (2-5):

$$v_i = \frac{m}{\rho A_i} = \frac{0.77956}{1.1986 \times 0.086917} = 7.4816 \frac{m}{s}$$

The inlet area of the plane where the measurement is done is as follows:

$$A_5 = 0.5bh = 0.5 \times 0.298 \times 0.5657 = 0.08429 m^2$$

The average velocity at this plane is then equal to:

$$v_5 = \frac{m}{\rho A_5} = \frac{0.77956}{1.1986 \times 0.08429} = 7.7148 \frac{m}{s}$$

The loss coefficient for two layers of mesh according to equation (2-21) is:

$$K_{he} = 22.5903 v_i^{-0.22795} = 22.5903 \times 7.4816^{-0.22795} = 14.2789$$

The average static pressure loss across the packing is determined by using equation (2-5). The density and velocity is assumed to be constant downstream of the packing and thus it simplifies the integrals to  $dA$ .

$$\Delta p = \frac{\sum \Delta p_q A_q}{A_5} = 843.01 Pa$$

The inlet loss coefficient can now be determined using equation (2-8). The assumptions are made that  $\alpha_{e,vc} = 1$  and that  $v_{vc} = v_5$ .

$$K_{ct} = \frac{p_a - (p + 0.5\rho v_5^2)}{0.5\rho v_i^2} = \frac{843.01 - 0.5 \times 1.2247 \times 7.7148^2}{0.5 \times 1.2247 \times 7.4816^2} - 14.2789 = 9.787$$

## D.2 CTSM Experimental Data

The incremental area stays the same for all experiments. Thus it is given once for completion. Equations (D-1) to (D-5) are utilized during the calculation of the incremental area. The data given in this section is based on using two layers of mesh.

**Table D-1 Incremental Area Data**

Position	$r_q$	$h_1$	$h_2$	$b_1$	$b_2$	$A_i$
1	0.0185	0.0093	0.0229	0.0050	0.0123	0.00012
2	0.0273	0.0229	0.0316	0.0123	0.0169	0.00013
3	0.0360	0.0316	0.0401	0.0169	0.0215	0.00016
4	0.0443	0.0401	0.0494	0.0215	0.0265	0.00022
5	0.0545	0.0494	0.0610	0.0265	0.0327	0.00034
6	0.0675	0.0610	0.0788	0.0327	0.0422	0.00066
7	0.0900	0.0788	0.1143	0.0422	0.0612	0.00184
8	0.1385	0.1143	0.1778	0.0612	0.0953	0.00497
9	0.2170	0.1778	0.2625	0.0953	0.1407	0.01000
10	0.3080	0.2625	0.3553	0.1407	0.1904	0.01535
11	0.4025	0.3553	0.4413	0.1904	0.2365	0.01835
12	0.4800	0.4413	0.5201	0.2365	0.2787	0.02032
13	0.5603	0.5201	0.5620	0.2787	0.2980	0.01207

### Sharp inlet Data

**Table D-2 Experimental data for Sharp inlet ( $d_i/H_i = 10.45$ )**

$p_a = 100600$  Pa  
 $T_a = 19.2^\circ\text{C}$   
 $\Delta p_n = 105.4$  Pa  
 $\Delta p_{up} = 1180$  Pa

Position	$\Delta p_s$ [Pa]
1	831.96
2	831.96
3	832.85
4	833.74
5	835.51
6	837.28
7	838.17
8	841.71
9	845.26
10	847.91
11	848.80
12	852.34
13	846.14

**Table D-3 Experimental data for Sharp inlet ( $d_i/H_i = 11.61$ )**

$p_a = 100600$  Pa  
 $T_a = 19.2^\circ\text{C}$   
 $\Delta p_n = 105$  Pa  
 $\Delta p_{up} = 1270$  Pa

Position	$\Delta p_s$ [Pa]
1	937.41
2	936.52
3	937.41
4	937.41
5	939.18
6	940.95
7	942.73
8	944.50
9	947.16
10	948.93
11	948.93
12	951.59
13	944.50

**Table D-4 Experimental data for sharp inlet ( $d_i/H_i = 13.06$ )**

$p_a = 100600$  Pa  
 $T_a = 19.2^\circ\text{C}$   
 $\Delta p_n = 105$  Pa  
 $\Delta p_{up} = 1689$  Pa

Position	$\Delta p_s$ [Pa]
1	1125.26
2	1125.26
3	1125.26
4	1125.26
5	1127.04
6	1127.92
7	1129.69
8	1130.58
9	1132.35
10	1131.47
11	1128.81
12	1135.01
13	1125.26



### Walkway Data

**Table D-5 Experimental data for walkway (XxY = 0x1.8m)**

$p_a = 100700 \text{ Pa}$

$T_a = 15.8^\circ\text{C}$

$\Delta p_n = 105.4 \text{ Pa}$

$\Delta p_{up} = 1220 \text{ Pa}$

Position	$\Delta p_s [\text{Pa}]$
1	938.30
2	939.18
3	940.07
4	940.07
5	940.95
6	943.61
7	945.39
8	947.16
9	951.59
10	955.13
11	956.90
12	960.45
13	957.79

**Table D-6 Experimental data for walkway (XxY = 0x3.6m)**

$p_a = 100740 \text{ Pa}$

$T_a = 15.8^\circ\text{C}$

$\Delta p_n = 105.4 \text{ Pa}$

$\Delta p_{up} = 1205 \text{ Pa}$

Position	$\Delta p_s [\text{Pa}]$
1	919.69
2	917.92
3	916.14
4	916.14
5	916.14
6	917.92
7	919.69
8	921.46
9	925.89
10	930.32
11	929.44
12	932.98
13	928.55

**Table D-7 Experimental data for walkway (XxY = 0x7.2m)**

$p_a = 100740 \text{ Pa}$

$T_a = 15.8^\circ\text{C}$

$\Delta p_n = 105.4 \text{ Pa}$

$\Delta p_{up} = 1190 \text{ Pa}$

Position	$\Delta p_s [\text{Pa}]$
1	904.62
2	904.62
3	904.62
4	906.40
5	907.28
6	909.06
7	910.83
8	919.69
9	917.03
10	920.57
11	922.35
12	925.89
13	925.89

**Rounded inlet data****Table D-8 Experimental data for rounded inlet ( $r_i/d_i=0.025$ )**

$$p_a = 100700 \text{ Pa}$$

$$T_a = 15.8^\circ\text{C}$$

$$\Delta p_n = 105.4 \text{ Pa}$$

$$\Delta p_{up} = 1220 \text{ Pa}$$

Position	$\Delta p_s$
1	793.86
2	794.75
3	797.41
4	798.29
5	798.29
6	799.18
7	802.72
8	808.04
9	815.13
10	820.45
11	822.22
12	827.53
13	816.90

## Appendix E: Cooling tower inlet loss modelling using CFD

### E.1 Inlet loss coefficient sample calculation

Determining the inlet loss coefficient of a cooling tower with the aid of CFD is accomplished in the following manner; the data downstream of the fill, which is needed to calculate the loss coefficient, is extracted at a level above the fill material and then imported into an Excel sheet for further processing.

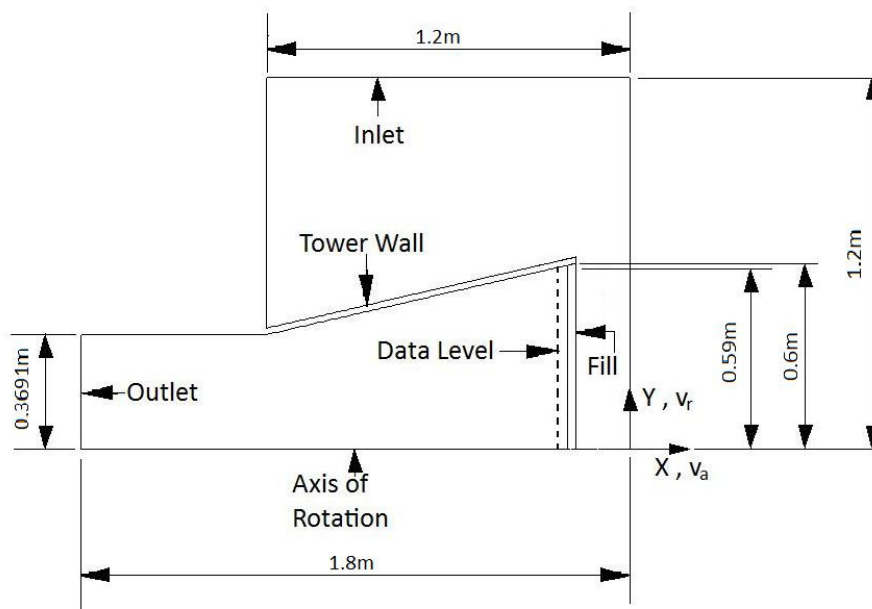


**Figure E-1 Domain of the axis-symmetric Fluent model developed to simulate the sector model experiment**

Figure E-1 yields an outline of the axis-symmetric model used with CFD to simulate the experimental model. The inputs to the model are the mass flow rate out of the tower, 11.5kg/s, and the loss coefficient for the fill which can either be equation (2-14) or equation (2-21). The inlet loss coefficient and effective diameter are calculated by extracting data at the level as indicated in Figure E-1. A sample calculation to obtain the results follows and are done with the aid of node 10 as a reference. The y-coordinate can be seen as a radius since this is an axis-symmetric model. The results are given in section E-2 for the sharp inlet and section E-3 for added structures.

**Table E-1 Data from CFD for further manipulation**

n	x	y	$v_r$	$v_a$	$ v $	$0.5\rho v^2$	$p-p_a$
1	-0.245	0.560	0.0725	-1.657	1.659	1.73	-939.31
2	-0.245	0.529	0.1427	-9.861	9.862	59.58	-939.02
3	-0.245	0.498	-0.0430	-9.598	9.598	56.42	-938.23
4	-0.245	0.466	-0.0450	-9.558	9.558	55.96	-938.87
5	-0.245	0.435	-0.0580	-9.688	9.688	57.49	-939.83
6	-0.245	0.404	-0.0815	-9.862	9.862	59.57	-940.91
7	-0.245	0.373	-0.0949	-10.032	10.033	61.65	-942.14
8	-0.245	0.342	-0.0935	-10.176	10.176	63.43	-943.51
9	-0.245	0.311	-0.0883	-10.295	10.295	64.92	-944.92
<b>10</b>	<b>-0.245</b>	<b>0.280</b>	<b>-0.0809</b>	<b>-10.393</b>	<b>10.393</b>	<b>66.16</b>	<b>-946.28</b>
11	-0.245	0.249	-0.0720	-10.471	10.471	67.16	-947.52
12	-0.245	0.218	-0.0615	-10.534	10.534	67.96	-948.62
13	-0.245	0.187	-0.0512	-10.582	10.582	68.58	-949.57
14	-0.245	0.155	-0.0463	-10.608	10.608	68.93	-950.37
15	-0.245	0.124	-0.0464	-10.600	10.600	68.82	-951.04
16	-0.245	0.093	-0.0380	-10.500	10.501	67.53	-951.55
17	-0.245	0.062	-0.0242	-10.463	10.463	67.06	-951.93
18	-0.245	0.031	-0.0104	-10.466	10.466	67.09	-952.17
19	-0.245	0.000	-0.0003	-10.473	10.473	67.18	-952.24

The inlet area and the area at the level where the data is measured can be calculated as:

$$A_3 = \pi r_3^2 = 1.31m^2$$

$$A_5 = \pi r_5^2 = 1.097m^2$$

Thus the average inlet velocity and average velocity at the level where the data is measured is:

$$v_3 = m/\rho A_3 = 8.301m/s$$

$$v_5 = m/\rho A_5 = 8.56m/s$$

Thus the incremental area can be calculated as:

$$A_{10} = \pi[((y_{11} + y_{10})/2)^2 - ((y_{10} + y_9)/2)^2] = 0.06683m^2$$

The incremental volume flow rate is calculated using the axial velocity since it is noted that the velocity magnitude does not differ significantly from the value of the axial velocity.

$$Q_{10} = v_{a,10}A_{10} = 0.68m^3/s$$

The density stays constant across the fill and has a value of 1.225. The mass flow rate is then calculated as:

$$m_{10} = \rho_{10}Q_{10} = 0.83kg/s$$

The point where the vena contracta stops is determined as the point where:

$$\sum_{i=k}^{19} m_i = m$$

k is the node where this equation is satisfied which is between 1 and 2 for this example. An interpolation constant is now calculated as:

$$C = \frac{m - \sum_{i=2}^{19} m_i}{\sum_{i=1}^{19} m_i - \sum_{i=2}^{19} m_i} = 0.492$$

The area of the vena contracta is then:

$$A_{vc} = \sum_{i=2}^{19} A_i + C \left( \sum_{i=1}^{19} A_i - \sum_{i=2}^{19} A_i \right) = 0.957 m^2$$

The average velocity of the vena contracta is:

$$v_{vc} = \left[ \sum_{i=2}^{19} Q_i + C \left( \sum_{i=1}^{19} Q_i - \sum_{i=2}^{19} Q_i \right) \right] / A_{vc} = 9.811 m/s$$

The kinetic energy coefficient can now be calculated using equation (3-9):

$$\alpha_{e,vc} = \sum_{i=1}^{19} v_i^3 A_i / (A_3 v_{vc}^3) = 1.047$$

Substituting  $v_3$  into equation (3-12) yields the fill loss coefficient:

$$K_{he} = 11.32$$

The average pressure drop is calculated using equation (3-6).

$$\overline{p - p_a} = \sum_{i=1}^{19} (p - p_a)_i Q_i / \sum_{i=1}^{19} Q_i = -943.14 Pa$$

The inlet loss coefficient according to equation (3-5) is:

$$K_{ct} = 9.565$$

## E.2 Data from Fluent for sharp inlet

**Table E-2 Sharp inlet Input parameters for Fluent**

$m_{tot}$ (kg/s)	15000.00
$d_i$ (m)	104.50
$A_i$ (m <sup>2</sup> )	8576.74
$r_s$ (m)	51.61
$A_s$ (m <sup>2</sup> )	8369.3
$p_{atm}$ (kPa)	100
$\rho_{ref}$ (kg/m <sup>3</sup> )	1.23
$v_{m,inlet}$ (m/s)	1.43
$v_{m5}$ (m/s)	1.46
Scale	87.3:1

**Table E-3 Sharp inlet output from Fluent for  $d_i/H_i = 6$**

$A_{tot,vc}$ (m <sup>2</sup> )	8318.44	8303.86	8288.50	8239.20	7708.33
$d_{ie}$ (m)	102.91	102.82	102.73	102.42	99.07
$d_{ie}/(d_i+2t_s)$	0.97	0.97	0.96	0.96	0.93
$v_{m,vc}$ (m/s)	1.47	1.47	1.48	1.49	1.59
$v_{m5}$ (m/s)	1.46	1.46	1.46	1.46	1.46
$\alpha_{e,vc}$	1.0067	1.0097	1.0201	1.0568	1.0358
$p_s$ (pa)	99965.04	99970.02	99974.87	99979.44	99983.62
$K_{he}$	24.00	20.00	16.00	12.00	8.00
Eq (2-8)	2.95	2.96	3.08	3.42	4.07
Eq (2-3)	2.93	2.93	3.03	3.32	3.84

**Table E-4 Sharp inlet output from Fluent for  $d_i/H_i = 6.97$**

$A_{tot,vc}$ (m <sup>2</sup> )	8318.69	8309.06	8291.29	8186.60	7436.90
$d_{ie}$ (m)	102.92	102.86	102.75	102.10	97.31
$d_{ie}/(d_i+2t_s)$	0.97	0.97	0.96	0.96	0.91
$v_{m,vc}$ (m/s)	1.47	1.47	1.48	1.50	1.65
$v_{m5}$ (m/s)	1.46	1.46	1.46	1.46	1.46
$\alpha_{e,vc}$	1.0098	1.0191	1.0450	1.0876	1.0325
$p_s$ (pa)	99964.18	99969.06	99973.76	99978.10	99982.05
$K_{he}$	24.00	20.00	16.00	12.00	8.00
Eq (2-8)	3.64	3.73	3.97	4.50	5.32
Eq (2-3)	3.62	3.69	3.90	4.35	5.00

**Table E-5 Sharp inlet output from Fluent for  $d_i/H_i = 8.71$** 

$A_{tot,vc} (m^2)$	8331.85	8330.85	8283.51	7691.38	6880.23
$d_{ie} (m)$	103.00	102.99	102.70	98.96	93.60
$d_{ie}/(d_i+2t_s)$	0.97	0.97	0.96	0.93	0.88
$v_{m,vc} (m/s)$	1.47	1.47	1.48	1.59	1.78
$v_{m5} (m/s)$	1.46	1.46	1.46	1.46	1.46
$\alpha_{e,vc}$	1.0335	1.0606	1.1077	1.0590	1.0197
$p_s (pa)$	99962.10	99966.72	99971.03	99974.87	99978.25
$K_{he}$	24.00	20.00	16.00	12.00	8.00
Eq (2-8)	5.31	5.60	6.15	7.08	8.37
Eq (2-3)	5.27	5.53	6.01	6.82	7.83

**Table E-6 Sharp inlet output from Fluent for  $d_i/H_i = 10.45$** 

$A_{tot,vc} (m^2)$	8343.31	8329.36	7877.27	7160.49	6341.94
$d_{ie} (m)$	103.07	102.98	100.15	95.48	89.86
$d_{ie}/(d_i+2t_s)$	0.97	0.97	0.94	0.90	0.84
$v_{m,vc} (m/s)$	1.47	1.47	1.55	1.71	1.93
$v_{m5} (m/s)$	1.46	1.46	1.46	1.46	1.46
$\alpha_{e,vc}$	1.0741	1.1226	1.0930	1.0370	1.0199
$p_s (pa)$	99959.16	99963.37	99967.06	99970.24	99972.83
$K_{he}$	24.00	20.00	16.00	12.00	8.00
Eq (2-8)	7.67	8.29	9.33	10.79	12.71
Eq (2-3)	7.58	8.15	9.09	10.35	11.90

**Table E-7 Sharp inlet output from Fluent for  $d_i/H_i = 11.61$** 

$A_{tot,vc} (m^2)$	8346.43	8251.62	7486.89	6806.09	5987.53
$d_{ie} (m)$	103.09	102.50	97.64	93.09	87.31
$d_{ie}/(d_i+2t_s)$	0.97	0.96	0.92	0.87	0.82
$v_{m,vc} (m/s)$	1.47	1.48	1.64	1.80	2.05
$v_{m5} (m/s)$	1.46	1.46	1.46	1.46	1.46
$\alpha_{e,vc}$	1.1138	1.1622	1.0630	1.0306	1.0222
$p_s (pa)$	99956.61	99960.38	99963.56	99966.21	99968.17
$K_{he}$	24.00	20.00	16.00	12.00	8.00
Eq (2-8)	9.71	10.69	12.14	14.02	16.44
Eq (2-3)	9.58	10.48	11.79	13.43	15.39

**Table E-8 Sharp inlet output from Fluent for  $d_i/H_i = 13.06$** 

$A_{tot,vc} (m^2)$	8287.64	7658.30	7017.96	6364.20	5592.55
$d_{ie} (m)$	102.72	98.75	94.53	90.02	84.38
$d_{ie}/(d_i+2t_s)$	0.96	0.93	0.89	0.85	0.79
$v_{m,vc} (m/s)$	1.48	1.60	1.74	1.92	2.19
$v_{m5} (m/s)$	1.46	1.46	1.46	1.46	1.46
$\alpha_{e,vc}$	1.1669	1.0895	1.0395	1.0244	1.0325
$p_s (pa)$	99952.45	99955.48	99957.99	99959.93	99961.13
$K_{he}$	24.00	20.00	16.00	12.00	8.00
Eq (2-8)	13.04	14.61	16.60	19.04	22.08
Eq (2-3)	12.84	14.29	16.10	18.23	20.71

**Table E-9 Sharp inlet output from Fluent for  $d_i/H_i = 14.93$** 

$A_{tot,vc} (m^2)$	7542.42	7021.63	6478.16	5872.65	5147.67
$d_{ie} (m)$	98.00	94.55	90.82	86.47	80.96
$d_{ie}/(d_i+2t_s)$	0.92	0.89	0.85	0.81	0.76
$v_{m,vc} (m/s)$	1.62	1.74	1.89	2.09	2.38
$v_{m5} (m/s)$	1.46	1.46	1.46	1.46	1.46
$\alpha_{e,vc}$	1.0758	1.0432	1.0296	1.0305	1.0415
$p_s (pa)$	99944.89	99947.06	99948.79	99949.78	99950.19
$K_{he}$	24.00	20.00	16.00	12.00	8.00
Eq (2-8)	19.09	21.35	23.97	27.17	30.85
Eq (2-3)	18.75	20.84	23.22	26.03	29.01



### E.3 Data from Fluent for added structures

**Table E-10 Added structures input parameters for Fluent**

$m_{tot}$ (kg/s)	11.500
$d_i$ (m)	1.200
$A_i$ (m <sup>2</sup> )	1.131
$r_5$ (m)	0.596
$A_5$ (m <sup>2</sup> )	1.116
$p_a$ (kPa)	100
$\rho_{ref}$ (kg/m <sup>3</sup> )	1.225
$v_i$ (m/s)	8.301
$K_{he}$	11.318

**Table E-11 Added structures at the inlet output from Fluent for  $d_i/H_i = 8.708$**

	Normal	<u>0x1</u>	<u>0x1t</u>	<u>0x2t</u>	<u>0x2</u>	<u>0x3t</u>	<u>0x3</u>	<u>0x4t</u>
$A_{tot,vc}$ (m <sup>2</sup> )	1.038	1.087	1.087	1.089	1.088	1.089	1.089	1.089
$d_{ie}$ (m)	1.149	1.176	1.177	1.178	1.177	1.178	1.177	1.178
$v_{m,vc}$ (m/s)	9.047	8.637	8.635	8.620	8.450	8.619	8.621	8.617
$\alpha_{e,vc}$	1.070	1.000	1.072	1.031	1.132	1.020	1.040	1.021
$p_s$ (Pa)	99210	99254	99272	99304	99278	99321	99296	99326
Eq. (2-8)	6.379	5.320	4.899	4.110	4.755	3.714	4.314	3.581
Eq. (2-3)	6.135	5.273	4.778	4.051	4.624	3.680	4.241	3.552

**Table E-12 Added structures at the inlet output from Fluent for  $d_i/H_i = 10.45$**

	Normal	<u>0x1</u>	<u>0x1t</u>	<u>0x2t</u>	<u>0x2</u>	<u>0x3t</u>	<u>0x3</u>	<u>0x4t</u>
$A_{tot,vc}$ (m <sup>2</sup> )	0.960	1.022	1.036	1.087	1.055	1.091	1.085	1.089
$d_{ie}$ (m)	1.106	1.141	1.149	1.177	1.159	1.178	1.176	1.178
$v_{m,vc}$ (m/s)	9.774	9.186	9.060	8.635	8.901	8.608	8.650	8.620
$\alpha_{e,vc}$	1.038	1.083	1.089	1.104	1.112	1.048	1.127	1.025
$p_s$ (Pa)	99057	99117	99134	99194	99150	99235	99178	99253
Eq. (2-8)	10.013	8.572	8.177	6.737	7.791	5.770	7.136	5.314
Eq. (2-3)	9.593	8.268	7.905	6.579	7.539	5.691	6.946	5.270

**Table E-13 Added structures at the inlet output from Fluent for  $d_i/H_i = 11$** 

	Normal	<u>0x1</u>	<u>0x1t</u>	<u>0x2t</u>	<u>0x2</u>	<u>0x3t</u>	<u>0x3</u>	<u>0x4t</u>
$A_{tot,vc} (m^2)$	0.937	0.988	1.010	1.083	1.016	1.088	1.058	1.089
$d_{ie} (m)$	1.092	1.122	1.134	1.174	1.138	1.177	1.161	1.178
$v_{m,vc} (m/s)$	10.017	9.499	9.299	8.669	9.238	8.627	8.873	8.621
$\alpha_{e,vc}$	1.031	1.063	1.073	1.136	1.078	1.070	1.114	1.032
$p_s (Pa)$	98996	99059	99085	99146	99091	99195	99126	99224
Eq. (2-8)	11.574	9.966	9.348	7.897	9.187	6.722	8.350	6.022
Eq. (2-3)	11.073	9.595	9.024	7.689	8.875	6.610	8.108	5.967

**Table E-14 Added structures at the inlet output from Fluent for  $d_i/H_i = 11.611$** 

	Normal	<u>0x1</u>	<u>0x1t</u>	<u>0x2t</u>	<u>0x2</u>	<u>0x3t</u>	<u>0x3</u>	<u>0x4t</u>
$A_{tot,vc} (m^2)$	0.914	0.958	0.977	1.040	0.978	1.087	1.017	1.089
$d_{ie} (m)$	1.079	1.104	1.115	1.151	1.116	1.177	1.138	1.177
$v_{m,vc} (m/s)$	10.268	9.799	9.612	9.024	9.588	8.634	9.232	8.573
$\alpha_{e,vc}$	1.026	1.048	1.055	1.098	1.053	1.105	1.079	1.062
$p_s (Pa)$	98922	98989	99016	99084	99023	99143	99062	99186
Eq. (2-8)	13.294	11.613	10.975	9.367	10.807	7.959	9.879	6.922
Eq. (2-3)	12.724	11.171	10.579	9.096	10.425	7.801	9.566	6.841

**Table E-15 Added structures at the inlet output from Fluent for  $d_i/H_i = 12.294$** 

	Normal	<u>0x1</u>	<u>0x1t</u>	<u>0x2t</u>	<u>0x2</u>	<u>0x3t</u>	<u>0x3</u>	<u>0x4t</u>
$A_{tot,vc} (m^2)$	0.889	0.930	0.946	1.001	0.950	1.073	0.980	1.089
$d_{ie} (m)$	1.064	1.088	1.097	1.129	1.100	1.169	1.117	1.177
$v_{m,vc} (m/s)$	10.554	10.096	9.923	9.381	9.879	8.750	9.577	8.622
$\alpha_{e,vc}$	1.024	1.206	1.046	1.072	1.047	1.127	1.060	1.065
$p_s (Pa)$	98829	98903	98931	99006	98938	99074	98981	99136
Eq. (2-8)	15.397	13.655	12.999	11.222	12.830	9.595	11.809	8.099
Eq. (2-3)	14.742	12.887	12.522	10.868	12.365	9.374	11.420	7.996

**Table E-16 Added structures at the inlet output from Fluent for  $d_i/H_i = 13.063$**

	<b>Normal</b>	<b>0x1</b>	<b>0x1t</b>	<b>0x2t</b>	<b>0x2</b>	<b>0x3t</b>	<b>0x3</b>	<b>0x4t</b>
<b><math>A_{tot,vc}</math> (m<sup>2</sup>)</b>	0.882	0.901	0.914	0.965	0.937	1.026	0.946	1.089
<b><math>d_{ie}</math> (m)</b>	1.060	1.071	1.079	1.108	1.092	1.143	1.098	1.177
<b><math>v_{m,vc}</math> (m/s)</b>	10.754	10.422	10.266	9.730	10.088	9.154	9.919	8.624
<b><math>\alpha_{e,vc}</math></b>	1.033	1.187	1.037	1.058	1.058	1.089	1.050	1.101
<b><math>p_s</math> (Pa)</b>	98714	98796	98825	98907	98833	98987	98879	99069
<b>Eq. (2-8)</b>	18.149	16.195	15.521	13.560	15.327	11.670	14.224	9.709
<b>Eq. (2-3)</b>	17.428	15.338	14.949	13.123	14.779	11.372	13.741	9.561

**Table E-17 Added structures away from the inlet output from Fluent for  $d_i/H_i = 8.708$**

	<b>3.5x3</b>	<b>3x1</b>	<b>3x2</b>	<b>3x3</b>	<b>4x3</b>	<b>ri/di</b>		
						<b>0.020</b>	<b>0.010</b>	<b>0.025</b>
<b><math>A_{tot,vc}</math> (m<sup>2</sup>)</b>	1.089	1.063	1.088	1.089	1.088	1.090	1.089	1.090
<b><math>d_{ie}</math> (m)</b>	1.177	1.163	1.177	1.178	1.177	1.178	1.177	1.178
<b><math>v_{m,vc}</math> (m/s)</b>	8.622	8.831	8.629	8.618	8.626	8.615	8.624	8.614
<b><math>\alpha_{e,vc}</math></b>	1.029	1.070	1.042	1.030	1.033	1.031	1.032	1.031
<b><math>p_s</math> (Pa)</b>	99294	99237	99279	99296	99287	99299	99297	99298
<b>Eq. (2-8)</b>	4.353	5.724	4.714	4.290	4.520	4.227	4.284	4.247
<b>Eq. (2-3)</b>	4.307	5.543	4.637	4.248	4.460	4.186	4.224	4.206

**Table E-18 Added structures away from the inlet output from Fluent for  $d_i/H_i = 10.45$**

	<b>3.5x3</b>	<b>3x1</b>	<b>3x2</b>	<b>3x3</b>	<b>4x3</b>	<b>ri/di</b>		
						<b>0.020</b>	<b>0.010</b>	<b>0.025</b>
<b><math>A_{tot,vc}</math> (m<sup>2</sup>)</b>	1.088	0.993	1.063	1.089	1.084	1.089	1.085	1.090
<b><math>d_{ie}</math> (m)</b>	1.177	1.125	1.163	1.177	1.175	1.178	1.175	1.178
<b><math>v_{m,vc}</math> (m/s)</b>	8.629	9.450	8.832	8.622	8.664	8.617	8.655	8.269
<b><math>\alpha_{e,vc}</math></b>	1.055	1.042	1.067	1.040	1.084	1.038	1.097	1.175
<b><math>p_s</math> (Pa)</b>	99213	99104	99176	99228	99190	99234	99186	99189
<b>Eq. (2-8)</b>	6.285	8.882	7.176	5.917	6.850	5.757	6.932	6.832
<b>Eq. (2-3)</b>	6.193	8.552	7.001	5.855	6.703	5.704	6.773	6.732

**Table E-19 Added structures away from the inlet output from Fluent for  $d_i/H_i = 11$**

	<u>3.5x3</u>	<u>3x1</u>	<u>3x2</u>	<u>3x3</u>	<u>4x3</u>	<u>ri/di</u>		
						<b>0.020</b>	<b>0.010</b>	<b>0.025</b>
$A_{tot,vc} (m^2)$	1.087	0.972	1.042	1.089	1.062	1.089	1.060	1.090
$d_{ie} (m)$	1.177	1.113	1.152	1.177	1.163	1.178	1.162	1.178
$v_{m,vc} (m/s)$	8.635	9.657	9.006	8.623	8.841	8.617	8.857	8.459
$\alpha_{e,vc}$	1.074	1.036	1.056	1.046	1.070	1.042	1.078	1.102
$p_s (Pa)$	99179	99052	99135	99202	99151	99165	99160	99211
Eq. (2-8)	7.104	10.123	8.143	6.541	7.766	7.399	7.559	6.317
Eq. (2-3)	6.983	9.737	7.925	6.469	7.586	7.341	7.365	6.239

**Table E-20 Added structures away from the inlet output from Fluent for  $d_i/H_i = 11.611$**

	<u>3.5x3</u>	<u>3x1</u>	<u>3x2</u>	<u>3x3</u>	<u>4x3</u>	<u>ri/di</u>		
						<b>0.020</b>	<b>0.010</b>	<b>0.025</b>
$A_{tot,vc} (m^2)$	1.084	0.949	1.021	1.088	1.039	1.089	1.034	1.090
$d_{ie} (m)$	1.175	1.099	1.140	1.177	1.150	1.178	1.148	1.178
$v_{m,vc} (m/s)$	8.662	9.889	9.192	8.625	9.035	8.618	9.076	8.616
$\alpha_{e,vc}$	1.096	1.032	1.050	1.057	1.059	1.047	1.065	1.047
$p_s (Pa)$	99136	98988	99085	99169	99103	99139	99112	99183
Eq. (2-8)	8.116	11.650	9.329	7.330	8.918	8.019	8.705	6.976
Eq. (2-3)	7.958	11.202	9.066	7.241	8.688	7.953	8.457	6.912

**Table E-21 Added structures away from the inlet output from Fluent for  $d_i/H_i = 12.294$**

	<u>3.5x3</u>	<u>3x1</u>	<u>3x2</u>	<u>3x3</u>	<u>4x3</u>	<u>ri/di</u>		
						<b>0.020</b>	<b>0.010</b>	<b>0.025</b>
$A_{tot,vc} (m^2)$	1.059	0.925	0.998	1.088	1.016	1.089	1.009	1.090
$d_{ie} (m)$	1.161	1.085	1.127	1.177	1.137	1.178	1.133	1.178
$v_{m,vc} (m/s)$	8.863	10.149	9.403	17.301	9.242	8.618	9.304	8.616
$\alpha_{e,vc}$	1.083	1.029	1.045	0.133	1.053	1.053	1.057	1.054
$p_s (Pa)$	99083	98908	99023	99125	99043	99149	99051	99150
Eq. (2-8)	9.388	13.554	10.812	8.378	10.345	7.795	10.141	7.770
Eq. (2-3)	9.188	13.030	10.489	8.843	10.058	7.720	9.832	7.697

**Table E-22 Added structures away from the inlet output from Fluent for  $d_i/H_i = 13.062$**

	<u><b>3.5x3</b></u>	<u><b>3x1</b></u>	<u><b>3x2</b></u>	<u><b>3x3</b></u>	<u><b>4x3</b></u>	<u><b>ri/di</b></u>		
						<b>0.020</b>	<b>0.010</b>	<b>0.025</b>
<b><math>A_{tot,vc}</math> (m<sup>2</sup>)</b>	1.031	0.898	0.974	1.087	0.991	1.074	0.984	1.090
<b><math>d_{ie}</math> (m)</b>	1.146	1.069	1.114	1.176	1.123	1.170	1.119	1.178
<b><math>v_{m,vc}</math> (m/s)</b>	9.106	10.551	9.635	8.639	9.475	8.672	9.543	8.617
<b><math>\alpha_{e,vc}</math></b>	1.071	0.995	1.044	1.105	1.050	1.058	1.052	1.062
<b><math>p_s</math> (Pa)</b>	99014	98807	98945	99067	98967	99074	98974	99109
<b>Eq. (2-8)</b>	11.032	15.950	12.673	9.748	12.141	9.570	11.976	8.743
<b>Eq. (2-3)</b>	10.768	15.354	12.280	9.589	11.791	9.474	11.605	8.659